UNIVERSITY OF CALIFORNIA,
IRVINE

Effect of Particles on the Microstructure and Rheology of Solid-Stabilized Emulsions

DISSERTATION

submitted in partial satisfaction of the requirements
for the degree of

DOCTOR OF PHILOSOPHY

in Chemical and Biochemical Engineering

by

Maxsim Grigorovich Kaganyuk

Dissertation Committee:
Professor Ali Mohraz, Chair
Professor Elliot Botvinick
Professor Michael Dennin

2019

TABLE OF CONTENTS

LIST OF FIGURES

LIST OF EQUATIONS

ACKNOWLEDGMENTS

I appreciate the opportunity I have had to work in the Colloid Science Lab these past six years. I would like to sincerely thank my research advisor, Ali Mohraz, for all his mentorship, guidance and patience along this journey. The high standards you have work to instill into all aspects of my work is something I will try to carry with me as I move beyond my academic career.

A big thank you to Dr. Elliot Botvinick and Dr. Michael Dennin for serving on my defense committee and providing insightful feedback on my qualifying exam.

To all my current and former labmates, I appreciate the positive and welcoming environment you helped create within the Colloid Science Lab. It has been an honor to work alongside you and I hope all the best in your research endeavors. A special thank you to Jessica Witt, who helped get me started on my research when I first joined the lab.

Thank you to all the administrative staff for all you do to keep the department running. Your work is appreciated! Special thanks to Yi-San and Steve for all their help.

Lastly, to my family, I am grateful for all the support you have provided me throughout my academic career. Though we have been separated by distance during my time at UCI, you have and always will be with me. Thank you so much and hope to see you all soon!

CURRICULUM VITAE

Maxsim Grigorovich Kaganyuk

EDUCATION

2019 **Doctor of Philosophy – Chemical and Biochemical Engineering**
University of California, Irvine, *Irvine, California*

2017 **Master of Science – Chemical and Biochemical Engineering**
University of California, Irvine, *Irvine, California*

2013 **Bachelor of Science – Chemical Engineering**
University of Washington, Seattle, Washington

PUBLICATIONS

1. Impact of Particle Size on Droplet Coalescence in Solid-Stabilized High Internal Phase Emulsions, **M. Kaganyuk** and A. Mohraz. *Langmuir* (2019).
2. Role of particles in the rheology of solid-stabilized high internal phase emulsions, **M. Kaganyuk** and A. Mohraz. *J. Colloid Interface Sci.* (2019)
3. Non-monotonic dependence of Pickering emulsion gel rheology on particle volume fraction, Soft Matter, **M. Kaganyuk** and A. Mohraz. Soft Matter (2017)

CONFERENCE PRESENTATIONS

1. Direct observations into the deformation of solid-stabilized droplets under shear flow, M. Kaganyuk and A. Mohraz. 91st Society of Rheology Annual Meeting, October 2019, Raleigh, NC.
2. Impact of particles on droplet coalescence in solid-stabilized high internal phase emulsions, M. Kaganyuk and A. Mohraz, 93rd Colloid and Surface Science Symposium, June 2019 Atlanta, GA.
3. Role of interfacially adsorbed particles in the rheology of solid-stabilized emulsions, M. Kaganyuk and A. Mohraz. 90th Society of Rheology Annual Meeting, October 2018, Houston, TX.
4. Interfacial Routes to Gelation in Solid-Stabilized Emulsions, M. Kaganyuk and A. Mohraz, AIChE Annual Meeting, October 2017, Minneapolis, MN.
5. Role of Solid-Stabilized Interfaces on the Rheology of Pickering Emulsions, **M. Kaganyuk** and A. Mohraz, 33rd Annual Meeting American Society for Gravitational and Space Research, October 2017, Renton, WA.
6. Impact of Inter-Droplet Interactions on Pickering Emulsion Rheology, **M. Kaganyuk** and A. Mohraz, 3rd International Conference on Droplets, July 2017, Los Angeles, CA.
7. Investigating the Role of Particles in the Rheology of Solid-Stabilized Emulsions, **M. Kaganyuk** and A. Mohraz, 91st Colloid and Surface Science Symposium, July 2017 New York, NY. (**Keynote Talk**)

8. Non-Monotonic Dependence of Pickering Emulsion Gel Rheology on Particle Loading, M. Kaganyuk and A. Mohraz, 91st Colloid and Surface Science Symposium, July 2017 New York, NY.
9. Microstructural Origins of Gel-like Rheology in Solid-Stabilized Emulsions, **M. Kaganyuk** and A. Mohraz, AIChE Annual Meeting, November 2016, San Francisco, CA.
10. Investigating the Microstructural Origins of Solid-Stabilized Emulsion Rheology, M. Kaganyuk and A. Mohraz, 32nd Annual Meeting American Society for Gravitational and Space Research, October 2016, Cleveland, OH.
11. Interfacial Routes to Colloidal Gelation, A. Mohraz and M. Kaganyuk, AIChE Annual Meeting, November 2015, Salt Lake City, UT.
12. Investigating the stability of bijels against external stresses, **M. Kaganyuk** and A. Mohraz, 31st Annual Meeting American Society for Gravitational and Space Research, November 2015, Alexandria, VA.
13. Investigating the Role of Particles in the Rheology of Solid-Stabilized Emulsions, **M. Kaganyuk** and A. Mohraz, 89th Colloid and Surface Science Symposium, June 2015 Pittsburgh, PA.

ABSTRACT OF THE DISSERTATION

Effect of Particles on the Microstructure and Rheology of Solid-Stabilized Emulsions

By

Maxsim Grigorovich Kaganyuk

Doctor of Philosophy in Chemical and Biochemical Engineering

University of California, Irvine, 2019

Professor Ali Mohraz, Chair

Emulsions are mixtures of immiscible fluids, which typically exhibit thermodynamically unstable droplets dispersed within a continuous body of fluid. Though surfactants have traditionally been used to achieve kinetically stable emulsions, colloids are increasingly being utilized. Today, solid-stabilized emulsions, or Pickering emulsions, are ubiquitous within the consumer market, often found in food formulations and many personal care products. However, to expand their utilization in many emerging technological applications, such as drug delivery, oil recovery and composite materials, a greater fundamental understanding of the role particles play in mediating the microstructure and mechanical behavior of Pickering emulsions is needed. To this end, I have studied a variety of solid-stabilized emulsions spanning a wide range of droplet concentrations. First, the microstructure of high internal phase emulsions is examined utilizing confocal microscopy. These concentrated systems are composed of highly faceted droplets separated by thin films of the continuous fluid. By varying the size of the stabilizing particles, it is revealed that larger particles provide greater stability against droplet coalescence, as they more readily adopt a bridged particle (particle which resides on two droplet interfaces)

monolayer configuration within the thin films, in lieu of particle bilayers. Second, confocal microscopy is supplemented with rheological measurements to explore the connection between the microstructure and rheology of solid-stabilized emulsions, and the influence particles have on these properties. In concentrated emulsions, particle excluded volume is shown to strongly impact the microstructural transition from spherical to highly faceted packed droplets, which is coupled to variations in sample rigidity. Pickering emulsion gels are dilute emulsions that feature a tenuous network of faceted droplets, held together by bridged monolayers of particles. In these systems particle loading is found to govern the degree of particle bridging within the droplet network, yielding a non-monotonic dependence of the zero-shear elastic modulus. Lastly, I have begun counter-rotation shear experiments, monitored with confocal microscopy to allow direct observation of the impact particles have on droplet deformation and rupture under shear. My fundamental results provide greater insight into the effect particles have on the microstructure and rheology of Pickering emulsions at various compositions and different processing conditions.

CHAPTER 1: INTRODUCTION

1.1 Solid-Stabilized Emulsions

Emulsions are mixtures of two immiscible fluids, which typically feature thermodynamically unstable droplets of one fluid dispersed within a continuous body of the other. Due to the ubiquitous nature of emulsions, they have received and continue to garner a lot of research attention across the scientific community. The utilization of these multiphase mixtures vary from commonly used consumer goods, such as cosmetics, personal hygiene products and food items, to applications within the pharmaceutical, petroleum and agricultural industries[1]–[7]. Many emerging technologies are using emulsions to develop composite materials for tissue engineering, energy storage, drug delivery, and electrochemical sensing applications[8]–[14]. As mentioned earlier, emulsions are in general thermodynamically unstable. Since the immiscible fluids energetically favor minimizing their contact with each other, energy input (often in the form of shear/mixing) is required to generate an emulsion[3], [15], [16]. Once formed an emulsion is susceptible to catastrophic instability as the dispersed droplets will strive to coalesce into larger, but fewer droplets, reducing the interface present until complete separation of the two fluids is reached. This is schematically illustrated in Figure 1.1, for a water-in-oil emulsion.

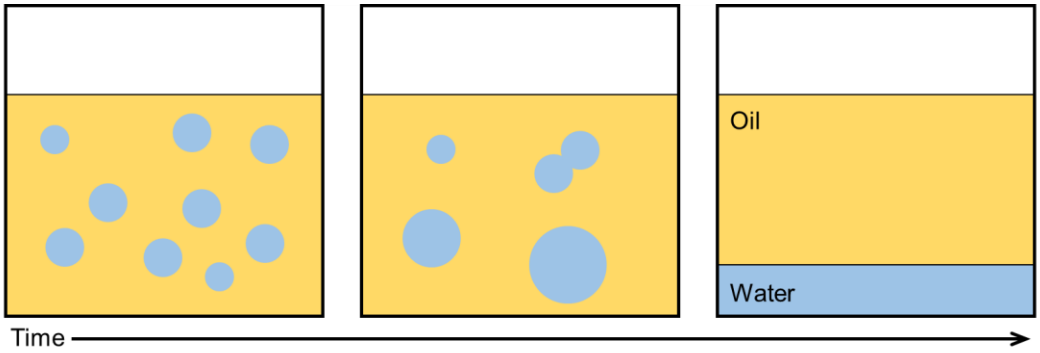

Figure 1.1. Illustration of droplet coalescence in a thermodynamically unstable emulsion.

To achieve a kinetically stable emulsion, emulsifying agents are utilized. These have traditionally been surfactant molecules, which readily adsorb to the interface between the two fluids due to their amphiphilic nature[2], [6], [17]. However, since W. Ramsden[18] and S. U. Pickering[19] first observed the ability of particles to stabilize fluid interfaces, in the early 20th century, they have increasingly been used in emulsion formulations. Such solid-stabilized emulsions are commonly referred to as Pickering emulsions. Unlike surfactants, particles can possess a homogeneous surface chemistry and still have a strong affinity to absorb to a fluid/fluid interface[17]. This is due to them being able to reduce the energetically unfavorable interface between the fluids upon interfacial adsorption. The energy required to detach a particle from an interface is often several magnitudes greater than its thermal energy, such that particles are typically considered irreversibly attached. The desorption energy, E, for a single particle on a flat interface can be estimated by Equation 1.1, where r, σ, and θ are particle radius, interfacial tension between the fluids and particle contact angle, respectively[1].

$$E = \pi r^2 \sigma (1 - |\cos(\theta)|)^2 \tag{1.1}$$

The contact angle in Equation 1.1 describes the particle's position on the interface and is measured, by convention, against the more polar fluid phase as illustrated in Figure 1.2 for a water/oil interface.

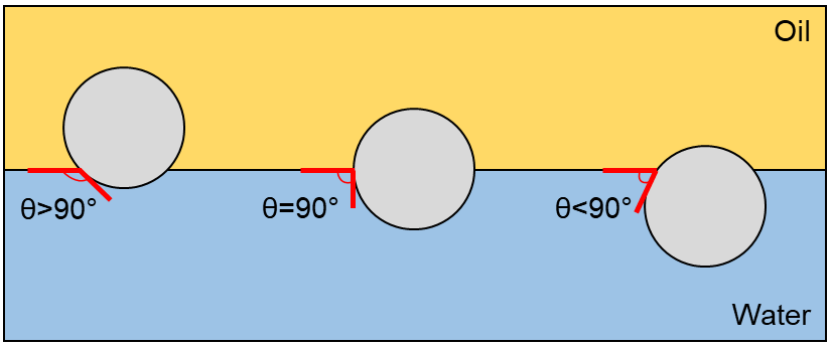

Figure 1.2. Illustration of the three-phase contact angle.

Here the contact angle depends on the interfacial tensions (σ) between the particle (p), water (w), and oil (o) interfaces according to Young's equation[20].

$$\cos(\theta) = \frac{\sigma_{po} - \sigma_{pw}}{\sigma_{ow}} \tag{1.2}$$

Early studies have investigated the impact of θ on emulsion stabilization, concluding that hydrophobic particles (θ>90°) tend to stabilize water-in-oil droplets and hydrophilic particles (θ<90°) tend to stabilize oil-in-water emulsions[15], [21]. Pickering emulsions are still being researched to get a more fundamental understanding of the particle stabilization mechanism[22], [17], [23]. Often, the nearly irreversible attachment of particles to interfaces is taken paramount to stabilizing Pickering emulsions against coalescence, however other studies suggest the stability of the thin film formed between merging droplets must be considered[23]–[27]. In Chapter 2, the stabilization mechanism of particles is considered when examining the microstructure of solid-stabilized high internal phase emulsions (HIPEs) that feature highly faceted droplets separated by thin films of fluid. Varying the size of the stabilizing particles is shown to impact the degree of coalesced droplets that arise when concentrating to a HIPE state. The ability of particles to confer to a configuration that provides greater stability against film rupture is important in these concentrated systems. In Chapter 5, experiments to directly observe isolated particle coated droplets under shear flow are reviewed. These preliminary observations consider the impact particles have on droplet deformation and rupture, but future experiments could shed light on Pickering emulsion stability against coalescence undergoing flow.

1.2 Emulsion Rheology

Emulsions, despite being composed almost entirely of liquids, can exhibit a wide range of rheological behavior[28]–[33]. This has led to them being actively studied from an academic perspective, as well as be utilized in a wide array of applications, as highlighted in the previous section. A big factor in the mechanical behavior of an emulsion is its microstructure. Depending on the fluid composition, particle chemistry, and formulation route, a variety of complex microstructures can be achieved in Pickering emulsions[34]–[38]. Simple Pickering emulsions, in which fluid droplets are dispersed within another simple fluid and primarily interact through excluded volume interactions, are largely the focus of this work. The span of microstructures achieved in such systems are shown in Figure 1.3.

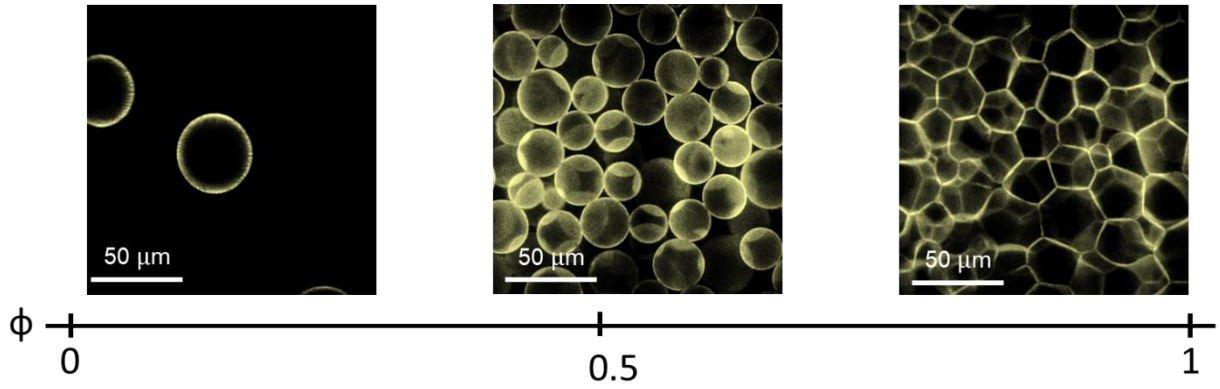

Figure 1.3. Simple Pickering emulsion over a wide range of droplet concentrations.

Here, ϕ, represents the concentrations of droplets as the volume fraction of the droplet fluid phase. Below the random close packing limit of spheres, $\phi \approx 64\%$, the emulsion microstructure largely consists of spherical droplets. Previous studies have shown that in this regime, emulsions will typically exhibit viscous behavior, unless strong attractive interdroplet interactions are present[2], [28]–[32]. Above this regime, droplets will deform as they continue to pack at higher concentrations. Elastic behavior for such emulsions has been reported and is rationalized at energy stored in the deformed interfaces of the highly packed droplets[28], [39]–

[42], [30]. In Chapter 3, the microstructure and rheology of solid-stabilized emulsions, above ϕ=50%, are examined to determine the impact of particles. In this study, particles with different surface chemistry were used to change the interdroplet interactions, which may influence emulsion behavior at the low end of this regime[31]. In Chapter 4, the rheology of Pickering emulsion gels is investigated. The characteristic microstructure of these dilute emulsions, ϕ<50%, differs significantly from simple Pickering emulsions (Figure 1.3) as seen in Figure 1.4.

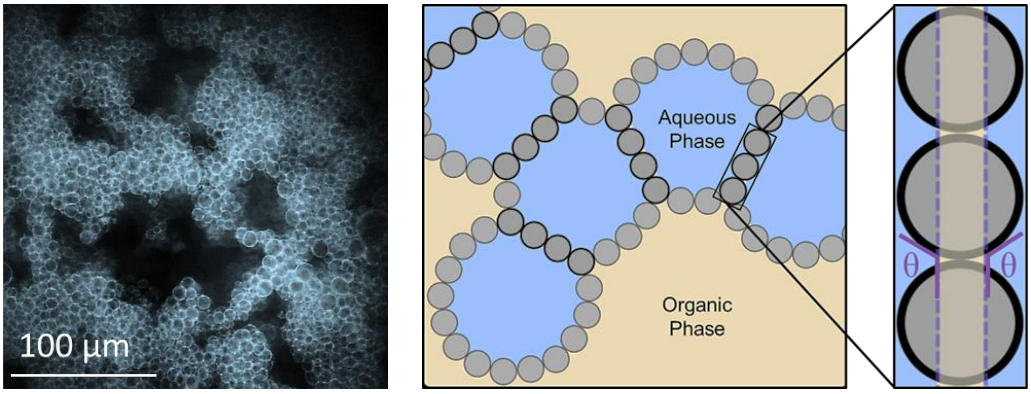

Figure 1.4. Pickering emulsion gel and an illustration of particle bridging between droplets

The particle surface chemistry in these systems allows particles to satisfy their three-phase contact angle simultaneously at two droplet interfaces as illustrated in Figure 1.4. In Pickering emulsion gels, these bridging particles stitch together droplets to form a tenuous network through the sample volume, which is attributed for the elastic behavior seen at low droplet concentrations[35]. This microstructure is similar to that of a colloidal gel[43]–[45], suggesting the rheology behavior of Pickering emulsion gels at increased particle loading may follow the well establish trend observed in colloidal gels. However, our work in Chapter 4 shows that particles significantly impact the droplet microstructure in Pickering emulsion gels to generate a non-monotonic dependence of their zero-shear elastic modulus with particle loading.

1.3 Overview of Experimental Techniques

1.2.1 Confocal Microscopy

Since its introduction in the 1950s, confocal microscopy has been heavily utilized in studying emulsions[46]. It is a simple technique which allows direct visualization of the microstructures present in solid-stabilized emulsions, as well as resolve individual particles, ~1 μm, in many of the fluid systems studied in this work. Its improvement over traditional fluorescence microscopy, stems from the use of a secondary pinhole aperture to help filter out-of-focus signals not coming from a point of interest. This is key to improving the imaging capability of 3D samples. A basic overview of the technique is illustrated in Figure 1.5.

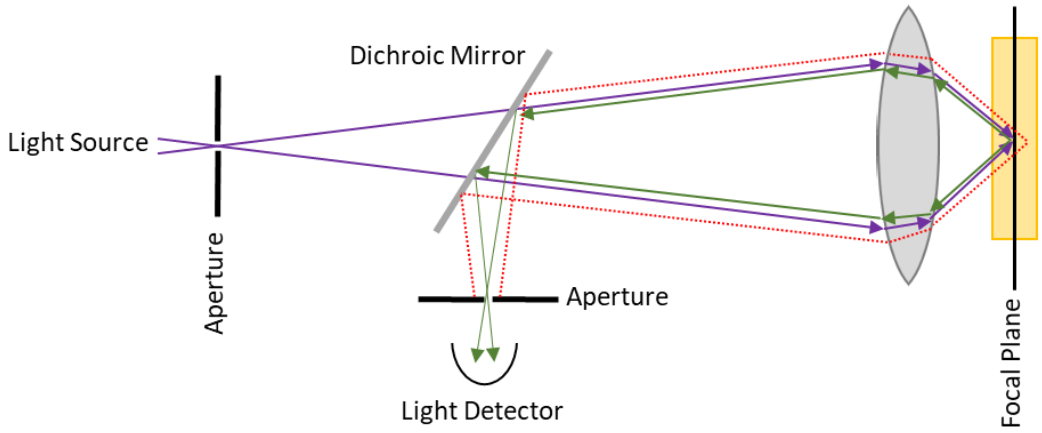

Figure 1.5. Overview of confocal microscopy.

The laser shines light (purple line) through a pinhole aperture to a specific point of interest in the fluorescent sample. The signals emitted by the sample are reflected back to a detector, but must first pass through a secondary pinhole aperture. Note, it is at this pinhole that out-of-focus light (red line) from outside the point of interest are blocked, while in focus light from the point of interest (green line) is passed to the detector. Repeating this process at many points on a set focal plane allows the generation of a 2D image of that sample. The focal plane can be varied to image the sample at difference depths to generate a 3D reconstruction from 2D

sample images. Throughout this dissertation, confocal imaging is conducted with a confocal scanner (Vt-eye, Visitech International) coupled to either an inverted microscope (Axio Observer A1, Carl Zeiss Microimaging, Inc.) or the optical stage of a stress-controlled rheometer (DHR-3, TA Instruments). A monochromatic laser (= 491 nm, Calypso, Cobolt AB) is used for the light source, with an acuosto-optic tunable filter for modulating the intensity of the laser.

Briefly, confocal images of experimental samples readily allow qualitative observations on the microstructural details of solid-stabilize emulsions. However, they can also be used for quantitative analysis of these details, whose differences between emulsion samples may be hard to discern solely by visual inspection. ImageJ software is utilized throughout this dissertation to perform simple characterizations of the droplet size, shape and interfacial morphology in experimental emulsion samples. The specific characterization method and analysis performed in each of the studies are outlined in Sections 2.2.3, 3.2.2, 4.2.3.

1.2.2 Oscillatory Rheology

Rheology examines the mechanical behavior of materials, spanning from purely viscous liquids to perfectly elastic solids and everything in between. The two extremes differ significantly in their deformation behavior. A perfectly elastic solid will experience a finite strain γ under an applied stress, τ, which is governed by the material's elastic modulus, E, as follows: $\tau = E\gamma$. The elastic solid completely recovers once the applied stress is removed. Whereas, a purely viscous liquid deforms at a constant shear rate, $\dot{\gamma}$, under an applied stress, which is set by the liquid's viscosity, η, as follows: $\tau = \eta\dot{\gamma}$. Deformations halts once stress is removed, without no recovery. These differences are utilized in oscillatory rheology experiments to probe viscoelastic materials, which exhibit both viscous (liquid-like) and elastic (solid-like) behavior. In Figure 1.6, the parallel plate geometry used in this work is illustrated.

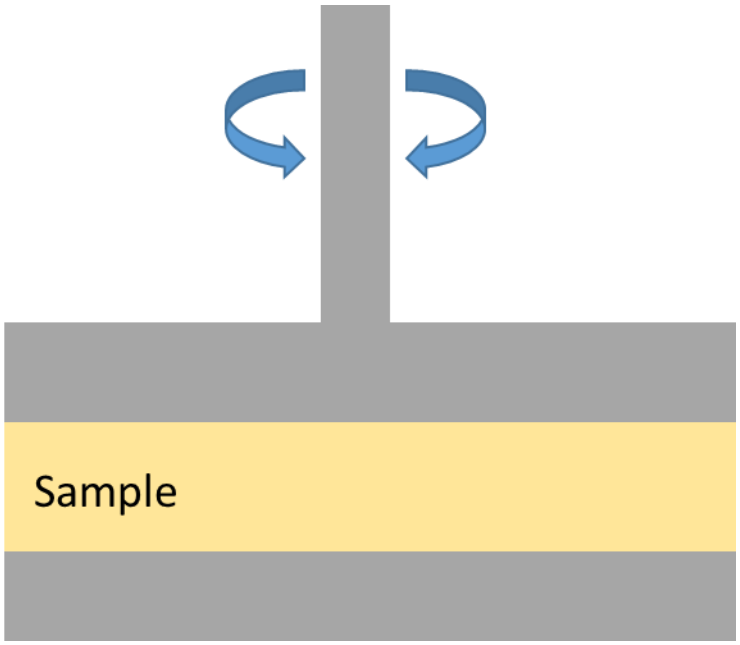

Figure 1.6. Illustration of the parallel plate geometry used for oscillatory rheology measurements.

The movement of the upper plate in Figure 1.6 subjects the sample to oscillatory shear deformation as strain and stress oscillate with time, t. The instantaneous strain and shear rate are shown in Equations 1.3 and 1.4 respectively.

$$\gamma = \gamma_0 \sin(\omega t) \tag{1.3}$$

$$\dot{\gamma} = \omega\gamma_0 \cos(\omega t) \tag{1.4}$$

Here γ_0 is the maximum strain amplitude and ω is the oscillation frequency. Since the strain and shear rate are out of phase with each other, the degree of solid-like to liquid-like behavior can be determined from the lag between strain, $\gamma(t)$, and stress, $\tau(t)$. For an elastic material $\tau(t)$ would vary in phase with $\gamma(t)$, whereas for viscous sample, $\tau(t)$ would vary completely out of phase with $\gamma(t)$. Within the linear viscoelastic regime, $\tau(t)$, can be described by Equation 1.5.

$$\sigma = \gamma_0[G'(\omega)\sin(\omega t) + G''(\omega)\cos(\omega t)] \tag{1.5}$$

Here, the storage modulus, G', is a measure of the sample's ability to store energy (solid-like behavior) and the loss modulus , G'', characterizes the sample's tendency to dissipate energy (liquid-like behavior). Samples with $G'> G''$ are considered more solid-like, whereas more liquid-like sample show $G''> G'$. In this work, the storage and loss moduli are measured by conducting standard small amplitude oscillatory strain sweeps. Characteristic results of such a test, done on a sample which exhibits gel-like rheology, is shown in Figure 1.7.

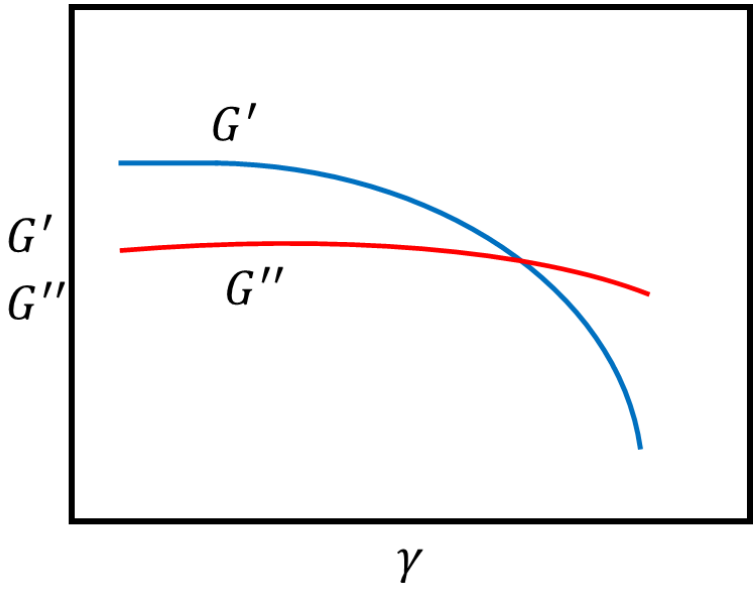

Figure 1.7. Characteristic oscillatory strain sweep on a gel-like sample.

At low strains the sample is dominated by solid-like behavior as $G'> G''$. At higher strains, it begins to yield and exhibit liquid-like behavior with $G''> G'$. The point at which the storage modulus crosses over with the loss modulus is often defined as the sample's yield stress. This quantify is not examined within our work, instead the zero-shear elastic modulus, G_0', is considered. G_0' is extracted from the oscillatory strain sweep as the average G' at the low strains where G' plateaus.

1.2.3 Steady Shear with Counter Rotation

In Chapter 5, we review some of the preliminary results acquired utilizing a counter-rotation stage to directly observe the behavior of particle-coated droplets under steady shear flow. The experimental set-up is illustrated below in Figure 1.8.

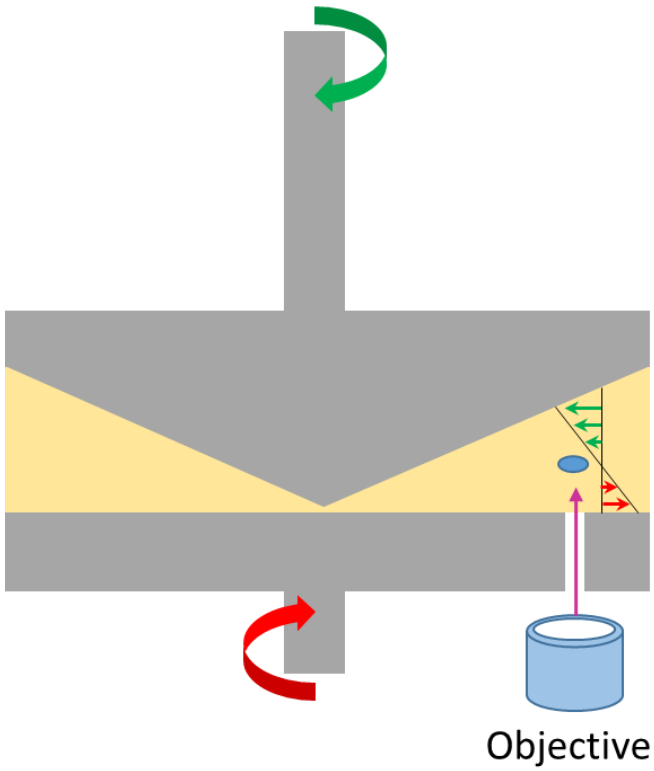

Figure 1.8. Counter-rotation experimental set-up. A droplet is isolated for confocal imaging.

Using a cone-and-plate geometry, the cone is spun in one direction, while the bottom stage is spun in the other direction. This establishes a zero-velocity plane at a certain depth in the sample, which can be modulated by adjusting the speed at which the bottom stage is spun counter to the cone. Control of the zero-velocity plane allows a droplet to be held in place, while it is imaged by an objective mounted underneath the stage. Note the sample sits on a glass plate, mounted to the counter-rotation stage. So far simple experiments at set shear rates have been conducted to examine deformation and rupture of droplets under shear flow. The relaxation behavior of droplets once shear is immediately halted, has also been visualized.

1.3 Structure of the Dissertation

In this dissertation, I examine the microstructure and rheology of solid-stabilized emulsions spanning across a wide composition range, from isolated droplets in dilute emulsions to high internal phase emulsions that feature highly faceted droplets. The goal is to generate a greater fundamental understanding of how these properties are effected by the particles present. The dissertation is structured as follows. Chapter 2 investigates the microstructure of high internal phase emulsions, stabilized with different size particles. Here it is shown that larger particles provide greater stability against droplet coalescence, as they are more readily able to rearrange into a bridged particle (particle which is able to simultaneously reside on two droplet interfaces) monolayer within the thin films neighbor droplets, in lieu of a particle bilayer configuration. In Chapter 3, concentrated emulsions (volume fraction of droplets is >50%) are investigated to reveal the significance particle excluded volume has on their microstructural and rheological transitions. The particle bridging phenomenon introduced in Chapter 2 is revisited in Chapter 4 during the study of Pickering emulsion gels. These dilute systems feature a tenuous network of faceted droplets, held together by bridged monolayers of particles. Particle loading is found to mediate the degree of particle bridging within the droplet network which is shown to result in a non-monotonic dependence of the zero-shear elastic modulus. Lastly in Chapter 5, our findings are summarized and some preliminary results from future work on directly observing particle-stabilized droplets under shear flow are briefly noted.

CHAPTER 2: IMPACT OF PARTICLE SIZE ON DROPLET COALESCENCE IN SOLID-STABILIZED HIGH INTERNAL PHASE EMULSIONS

2.1 Background

Emulsions typically consist of two immiscible fluids, with one fluid dispersed as droplets within the other. At high volume fractions of the dispersed fluid phase, $\phi > 0.74$, such systems are commonly referred to as high internal phase emulsions (HIPEs)[11]. Since HIPEs surpass the hexagonal close packing limit of spheres, they usually feature a microstructure composed of compressed droplets, ranging from slightly deformed spheres to highly faceted polyhedra separated by thin films of the continuous fluid phase[11], [47], [48]. This microstructure has been prominently utilized in templating polymerized HIPEs (polyHIPEs), a class of highly porous cellular materials with applications in tissue engineering, chemical sensing, drug delivery, and synthesis supports, to name a few[11], [12], [47]–[51]. Conventionally, surfactants have been used in creating HIPEs; however there is growing interest in the use of colloids as stabilizing agents to create surfactant-free HIPEs with potential applications in energy systems, cosmetics, food formulations, and pharmaceuticals, in addition to those mentioned earlier[13], [52]–[55]. With interest in these systems having cultivated relatively recently, the question of how particles impact the stability of the highly faceted droplets that arise in HIPEs has not been thoroughly explored[11], [17], [56]–[60]. This is a basic scientific question of significant practical interest, since droplet stability is the primary factor controlling the microstructure and utility of HIPEs. Therefore, this knowledge can pave the way for better-informed formulation and more effective utilization of solid-stabilized HIPEs in the aforementioned applications. In addition, investigation on this front can broaden our fundamental understanding of particle-mediated stabilization of fluid interfaces.

The notion of using solid particles to stabilize emulsions was initially introduced by Ramsden and Pickering, over a century ago[18], [19]. A large number of studies have since investigated different factors that contribute to the stability of solid-stabilized emulsions, often at lower concentrations than HIPEs. For example, early work investigated how particle surface chemistry governs the type of emulsion (oil-in-water or water-in-oil) formed[15], [21], [61]. Other studies have reported the importance of irreversible particle attachment to the droplet interface for emulsion stability[17], [22], [62], [23]. Some recent models have proposed that the stability of particle-coated droplets against coalescence is governed by the maximum capillary pressure that the thin film separating the droplets can withstand[23]–[27], [63]. This critical pressure is proportional to the fluid interfacial tension and inversely proportional to particle size. Therefore, if the same criteria were to hold across the entire compositional space, these findings would predict that decreasing particle size should enhance the stability of solid-stabilized HIPEs against coalescence. However, a number of other factors can also be at play when considering film stability in Pickering-Ramsden emulsions. For example, particles are able to participate in droplet bridging in a size-dependent manner, which can affect film stability; though this has only been demonstrated at lower dispersed phase volume fractions[35], [64]–[66]. Further, the particle excluded volume can strongly impact the microstructure and mechanics of Pickering-Ramsden emulsions, especially at the large volume fractions relevant to HIPEs[86]. Finally, emulsion stabilization has been linked to interfacial particle arrangement and mobility, which may be influenced by size-dependent interparticle interactions[26], [27], [63], [67]. Therefore, without a direct assessment, a clear understanding of how particle size may impact the stability of solid-stabilized HIPEs remains lacking. To this end, here we report a set of systematic experiments that aim to address this knowledge gap. Using confocal microscopy, the microstructures of solid-

stabilized emulsions created at increasing effective volume fractions of the dispersed phase, and with particles of various sizes, are examined. Setting stability criteria based on the distribution of droplet aspect ratios and the fraction of ruptured interfaces, we find that the use of larger particles enhances the stability of droplets against coalescence as the dispersed phase volume fraction is pushed into the HIPE state. At first glance, this finding appears to directly contradict the general notion that smaller particles result in more stable emulsions, which has been established both experimentally and theoretically[22], [23], [62], [68]. However, using direct imaging and microstructural quantification, we show that, during droplet faceting, larger particles are more readily able to arrange in a bridging monolayer configuration than smaller particles. We adopt a previously established theoretical model for capillary stabilization of liquid films with solid particles, and demonstrate that monolayer formation can significantly alter the capillary pressure profile, imparting mechanical stability to the liquid film even at very high volume fractions of the dispersed phase. Our study establishes the utter importance of droplet bridging in solid-stabilized HIPEs, and provides new insights into how particle size can be used to impact this important phenomenon and ultimately the stability of solid-stabilized emulsions. Further, our findings introduce new avenues for future research in this area, related to how monolayer formation may be governed by the interfacial rheology of solid-stabilized interfaces.

2.2 Experimental Methods

2.2.1 Emulsion Composition

The emulsions investigated in this study comprised of a 62 wt% sodium iodide (99% Fisher Scientific) solution in deionized water (Millipore), from hereon referred to as the aqueous phase, dispersed within a continuous phase of dodecane (99% Sigma Aldrich). Hexane (98.5% Fisher Scientific) was utilized as a provisional solvent in the initial formation of experimental

samples, the details of which are explained in the Emulsion Preparation section. The colloids used were polymethylmethacrylate (PMMA) particles with a grafted layer of polyhydroxystearic acid (PHSA), synthesized in our laboratory. Four batches of monodispersed particles (coefficient of variation CV < 5%) with average diameters of 0.66 μm, 1.40 μm, 1.73 μm and 2.20 μm, were made following previously reported synthesis procedures[69], [70]. Each particle batch was labeled with Nile red fluorescent dye (technical grade Sigma Aldrich) to allow visualization of the emulsions via fluorescence confocal imaging. Scanning Electron Microscopy (Quanta 3D FEG, Thermo Scientific) was conducted to characterize particle size and monodispersity (see Figure S2.1 in Section 2.5.1). In calculating experimental sample compositions, the density of the PHSA-grafted PMMA particles was taken to be 1.17 mg/μL[69]. An optical tensiometer (Attension Theta, Biolin Scientific) was used to measure the three-phase contact angle for each batch of particles via the immersed droplet technique[71] (see Figure S2.2 in Section 2.5.1). All four particle batches were found to exhibit a contact angle of $\theta \approx 153°$ between the aqueous phase and dodecane, and experimentally observed to stabilize water-in-oil emulsions by using rhodamine B (95% Sigma Aldrich) to selectively dye the aqueous phase, distinguishing it from dodecane in confocal microscopy (see Figure S2.3 in Section 2.5.1). The optical tensiometer was also used to measure the interfacial tension between the aqueous phase and dodecane to be $\sigma = 53$ mN/m at room temperature.

2.2.2 Emulsion Preparation

Experimental samples were formulated to have different compositions; however, each arrived to their final state from an initial dilute emulsion in which the volumetric ratio of aqueous to oil phase was 30:70. This was done by following a method developed in our previous investigation[37]. Briefly, an initial two-component continuous phase with a volatile and a non-

volatile compound (hexane and dodecane) was utilized, tuning their initial ratio to reach the desired continuous phase volume after the volatile component is fully evaporated. It was shown that aging an initial dilute emulsion for 5 hr achieves selective and complete removal of hexane from the continuous phase, with no noticeable loss in dodecane. Hence, samples in this study were made in a 1.5 mL centrifuge tube to which 0.36 mL aqueous phase, 0.84 mL oil phase including hexane, and a recorded mass of solids were added. The contents of the 1.5 mL centrifuge tube were emulsified with an ultrasonic probe (Sonifier 250, Branson Ultrasonics), running continuously at 2 W power for ~45 sec, followed by vortex mixing (Vortex Genie 2, Science Industries) at the highest speed setting for 5 min. The emulsified samples were then decanted into a 50-mm tall polycarbonate tube with an inner diameter of 25 mm, which was placed upright on a 40 × 50 mm optical glass coverslip. The 1.5 mL centrifuge tube was rinsed with 0.5 mL hexane to ensure that samples were completely transferred to the sample holder, where they were given 5 hr to age at room temperature. During aging, hexane evaporation caused the dispersed phase volume fraction to gradually increase throughout the sample, changing the mixture from a semi-concentrated Pickering emulsion to a solid-stabilized HIPE (see Figure 2.1 for snapshots of a representative sample during this aging process). Ostwald ripening is not observed during aging. After aging, the polycarbonate tube was carefully raised away to yield a cylindrical sample which would be immediately imaged with confocal microscopy (see Figure S2.4 in Section 2.5.1 for a digital image of a characteristic aged sample). With this protocol, the initial amount of hexane is used as a control knob to achieve solid-stabilized emulsions with different final compositions. For each batch of particles, the volumetric ratio of solids to aqueous phase was held at a certain ratio to create dilute emulsions (before aging) with a constant average droplet diameter of ~25 μm[72]. In this way, the role of particle

size could be isolated from possible droplet size effects, and investigated directly. Some samples were recreated as outlined above, but aged on the confocal microscope stage to record their microstructural evolution during aging (Figure 2.1).

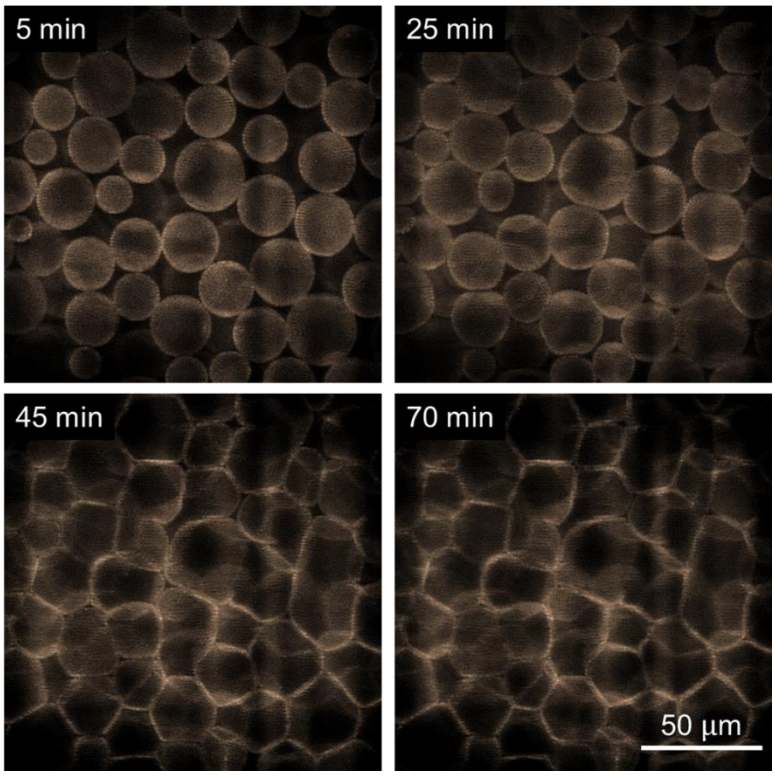

Figure 2.1. Confocal images illustrating the change in droplet microstructure during aging of an emulsion sample. Negligible change in structure was observed beyond 70 min.

2.2.3 Emulsion Characterization

Preparing emulsions on optical glass coverslips allowed each sample to be imaged on a custom microscopy stage coupled to a confocal scanner (Vt-eye, Visitech International). A 20X NA = 0.4 objective (Carl Zeiss AG) and a 100X NA = 1.4 oil-immersion objective (Carl Zeiss AG) were used to examine the overall microstructure and the arrangement of particles at the droplet interfaces, respectively. Confocal imaging was typically done ~15 µm into the sample, from the bottom coverslip, to avoid significant wall effects while retaining sufficient resolution to observe individual droplets (20X objective) or individual particles (100X objective). Images

generated from confocal microscopy were imported to ImageJ software to characterize the microstructure of each sample, specifically the number-average droplet aspect ratio, α. The aspect ratio, α_i, of at least 50 droplets was calculated as the ratio between their greatest length, l_i, and width, w_i, which are manually measured with the "straight line" tool in ImageJ. Note that w_i is evaluated perpendicular to l_i at its midpoint. ImageJ was also used to analyze the different morphologies of particle-stabilized films observed in highly faceted emulsions. Multiple images, taken with the 100X objective, were used to measure the length of the interfaces present. The total sum of interfacial lengths recorded for each characterized sample was ~1000 μm, grouped into four sets of approximately 250 μm each, used for statistical analysis of ruptured interfaces The analysis done to determine the different solid-stabilized films present in highly faceted samples is discussed further within Section 2.3.2 and Section 2.5.2.

2.2.4 Capillary Pressure Analysis

Our derivations for the capillary pressure of particle-stabilized emulsion films follow a simplified model of a spherical meniscus advancing through the converging/diverging pore created between spherical particles sequestered at the fluid interface[24], [25], [73]. The simple geometry of this model is utilized to generate nondimensionalized plots of capillary pressure versus an approximated emulsion film volume per stabilizing solids volume. All capillary pressure and film volume calculations were performed with MATLAB software (R2015a MathWorks). The equations used in calculating capillary pressure and film volume are derived in Section 2.5.3 and Section 2.5.4, respectively.

2.3 Results and Discussion

2.3.1 Droplet Aspect Ratio

In this study, four series of solid-stabilized emulsions are created at varying compositions. Polymethylmethacrylate (PMMA) microspheres with a polyhydroxystearic acid (PHSA) graft layer are used as the stabilizing solids in all four series, however between each sample set the diameter of the particles, δ_P, is changed (0.66 μm, 1.40 μm, 1.73 μm, 2.20 μm). In Figure 2.2, we show confocal images of representative emulsions stabilized with 0.66 μm particles. Their concentration is denoted by an effective dispersed volume fraction, ϕ_{eff}, taken as the sum of the dispersed fluid and particle volume fractions. As such, ϕ_{eff} accounts for the excluded volume of the stabilizing solids, which have been shown to influence Pickering emulsion microstructure and rheology[37].

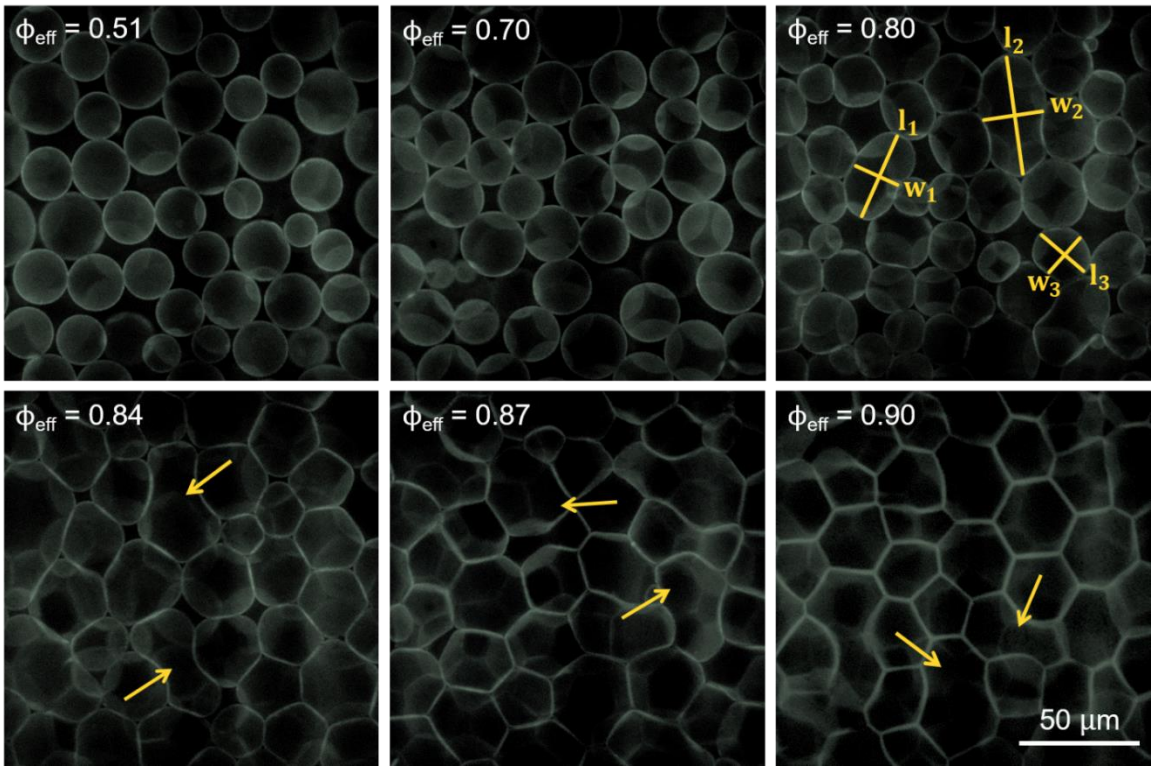

Figure 2.2. Confocal images of experimental emulsion samples stabilized at different effective dispersed volume fractions, ϕ_{eff}, by 0.66 μm particles. The lines, l_i and w_i, drawn in the sample at $\phi_{eff} = 0.80$ are characteristic of droplet aspect ratio measurements, which are discussed in Section 2.2.3. Arrows are inserted to highlight coalesced droplets.

From the images shown in Figure 2.2, we observe a qualitative change in the final microstructure of our samples as ϕ_{eff} increases: spherical droplets become concentrated, then begin to deform and eventually turn into highly faceted cells. The same transition in droplet shape is seen within all four emulsion sets, which we quantify by characterizing droplet aspect ratios. The aspect ratio, α_i, describes the deformation of an individual droplet and is taken as the ratio between its greatest length, l_i, and width, w_i, measured as shown for three representative droplets in Figure 2.2. The degree of droplet deformation in a sample is quantified by a number-average droplet aspect ratio, α. In Figure 2.3, α is plotted against ϕ_{eff} for the four emulsion series, stabilized by the denoted particles. For consistency, the colors and symbol shapes used to differentiate the four particle batches in Figure 2.3 will be used throughout this paper, including the false-colored confocal images. All four emulsion series show the same overall behavior in α as ϕ_{eff} increases: little change before $\phi_{eff} \approx 0.70$, and a pronounced rise past this point to a particle-size-dependent value at the highest ϕ_{eff} examined. We will next assess the details of this behavior. When our samples are imaged at their initial dilute state immediately after preparation ($\phi_{eff} < 0.40$), solid-stabilized droplets with almost fully coated surfaces are observed (refer to Section 2.5.1 for a volumetric confocal scan of an initial droplet showing near complete surface coverage, in Video V2.1). As the emulsion concentration gradually grows by evaporation of the provisional solvent (hexane), droplets will eventually begin to deform, increasing their surface area and yielding bare interfaces susceptible to coalescence. This is examined closer, considering four representative samples stabilized by 0.66 μm particles marked as A-D, for which α_i distributions are shown in Figure 2.3. Confocal images of these four specimens are part of the six panels shown in Figure 2.2, and will be used to aid in the discussion.

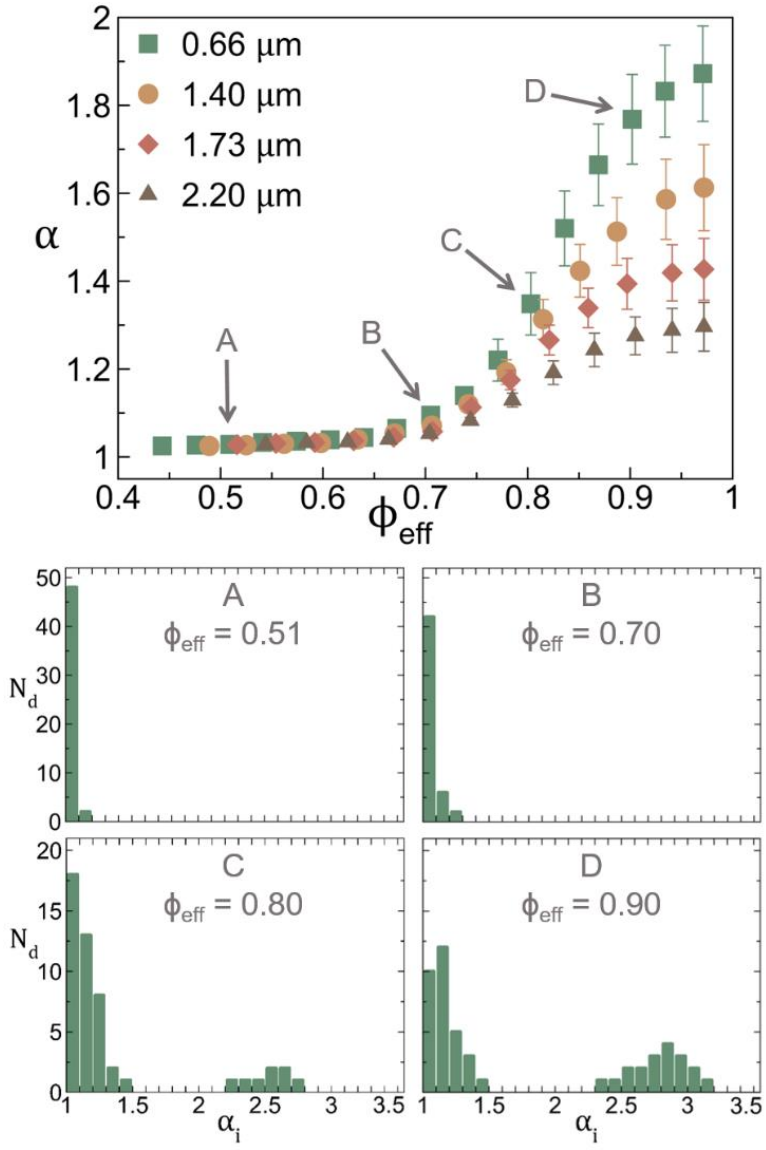

Figure 2.3. The average droplet aspect ratio, α, plotted versus the effective dispersed volume fraction, ϕ_{eff} (top). Error bars denote the standard error in α. Distributions in droplet aspect ratios, α_i, are shown for the labeled samples, which are part of the emulsion series stabilized by 0.66 µm particles (bottom). Note, confocal images of these four samples are shown in Figure 2.

Inspecting in Figure 2.2 the microstructures of the samples with $\phi_{eff} = 0.51$ and $\phi_{eff} = 0.70$ (denoted in Figure 2.3 as Samples A and B, respectively), both are found to be comprised almost entirely of undeformed droplets. This qualitative observation is reflected in their α_i distributions in Figure 2.3, where most droplets are seen to possess an aspect ratio of $\alpha_i \approx 1$. Therefore, below $\phi_{eff} \approx 0.70$, increases in ϕ_{eff} can be achieved without significant droplet deformation, causing the

lower $\alpha \approx 1$ plateau seen in Figure 2.3 for all sample series. We now turn to samples above $\phi_{eff} \approx 0.70$, which show a particle-size-dependent pronounced rise in α. Examining the α_i distributions of samples C and D, two distinct populations of droplets are observed: one clustered near $\alpha_i \approx 1$ and a second population at higher aspect ratios, $\alpha_i > 2$, with a clear separation between the two. Note, the emergence of the second droplet population increases the standard error in α, which is denoted by the error bars in Figure 2.3. For Sample C, the first population is attributed to droplets that experience only minimal deformation from their original spherical shape (see the image corresponding to $\phi_{eff} = 0.80$ in Figure 2.2, which contains a significant fraction of such droplets). For Sample D, the population near $\alpha_i \approx 1$ corresponds to droplets that have been compressed into faceted polyhedra in a nearly isotropic fashion, as seen for the majority of cells in the corresponding confocal image (corresponding to $\phi_{eff} = 0.90$ in Figure 2). In the second droplet population $\alpha_i > 2$, seen for both samples C and D, the greater droplet aspect ratios are believed to result from arrested coalescence of neighboring droplet pairs, which become kinetically trapped in an intermediate state of droplet fusion. This phenomenon has been reported in past studies examining the coalescence of particle-armored droplets[59], [74]–[78]. In Figure 2.2, a few faceted cells that appear to have formed from the arrested coalescence of two smaller droplets are highlighted by yellow arrows. Note that this assignment is made purely based on the large aspect ratios of these cells, however we are able to verify the occurrence of droplet coalescence in our experiments by monitoring a sample's microstructure as it ages from a dilute state (refer to Section 2.5.1 for Video V2.2). With the observations made between Figures 2.2 and 2.3 in mind, we argue that the pronounced rise in α above $\phi_{eff} \approx 0.70$ is primarily due to arrested coalescence (the second population with $\alpha_i > 2$), with minor additional contribution from droplet deformation (the first population with α_i only slightly greater than one). Therefore,

noticing the difference in the maximum α achieved between the sample series in Figure 2.3, we postulate that particle size has an impact on droplet stability against coalescence in solid-stabilized HIPEs. In Figure 2.4, we directly examine this notion. Here confocal images of samples at $\phi_{eff} \approx 0.97$, stabilized by the four different particle batches, are shown along with their respective droplet aspect ratio distributions. From the histograms, it is clear that the droplet population at $\alpha_i > 2$ systematically diminishes as larger particles are employed to stabilize the emulsions. Since we argue this population arises from arrested droplet coalescence, Figure 2.4 further corroborates that particle size impacts the stability of solid-stabilized HIPEs, with larger particles imparting greater stability against droplet coalescence. It must be emphasized that, this is in direct contrast with the behavior of dilute emulsions, in which smaller particles are generally observed to impart greater stability through higher interfacial elasticity and enhanced adsorption kinetics[88,95].

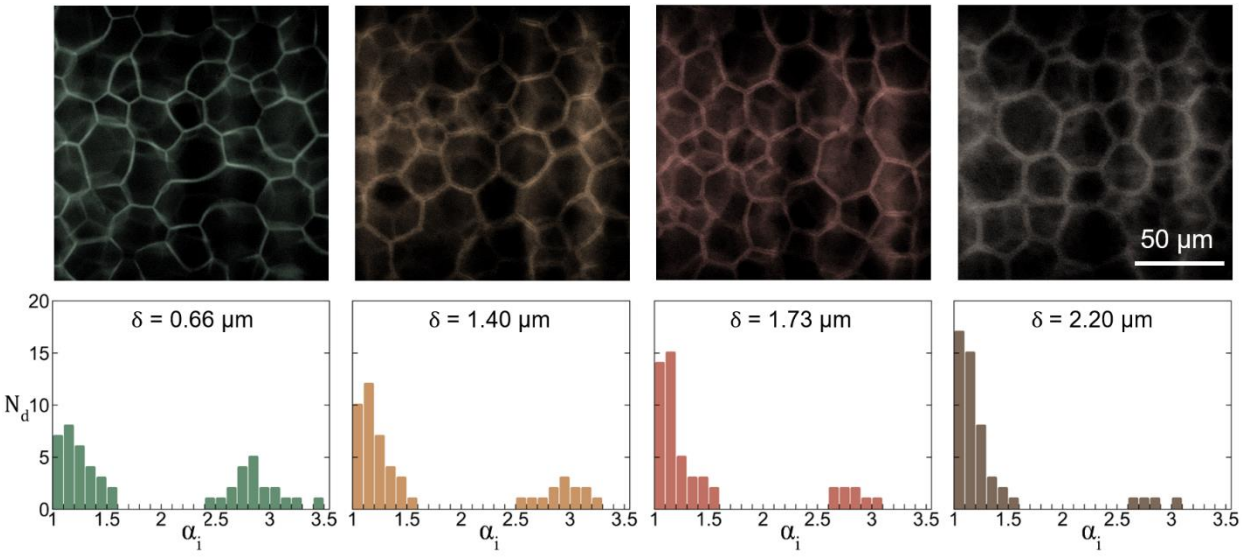

Figure 2.4. Confocal images of HIPE samples, each stabilized at $\phi_{eff} \approx 0.97$ by different size particles (top). For each sample the distribution in droplet aspect ratio, α_i, is shown (bottom).

2.3.2 Particle Monolayer Formation

Our observation of particle size affecting droplet stability in HIPEs is examined further by characterizing the particle-stabilized interfaces present in our samples. Our sample preparation protocol, using a provisional solvent, allows us to directly monitor the particle-laden interfaces as droplets are gradually compressed into their final state during sample aging. In Figure 2.5, we present confocal microscopy snapshots of two representative samples stabilized with 2.20 μm particles, at different stages of aging toward their final HIPE state.

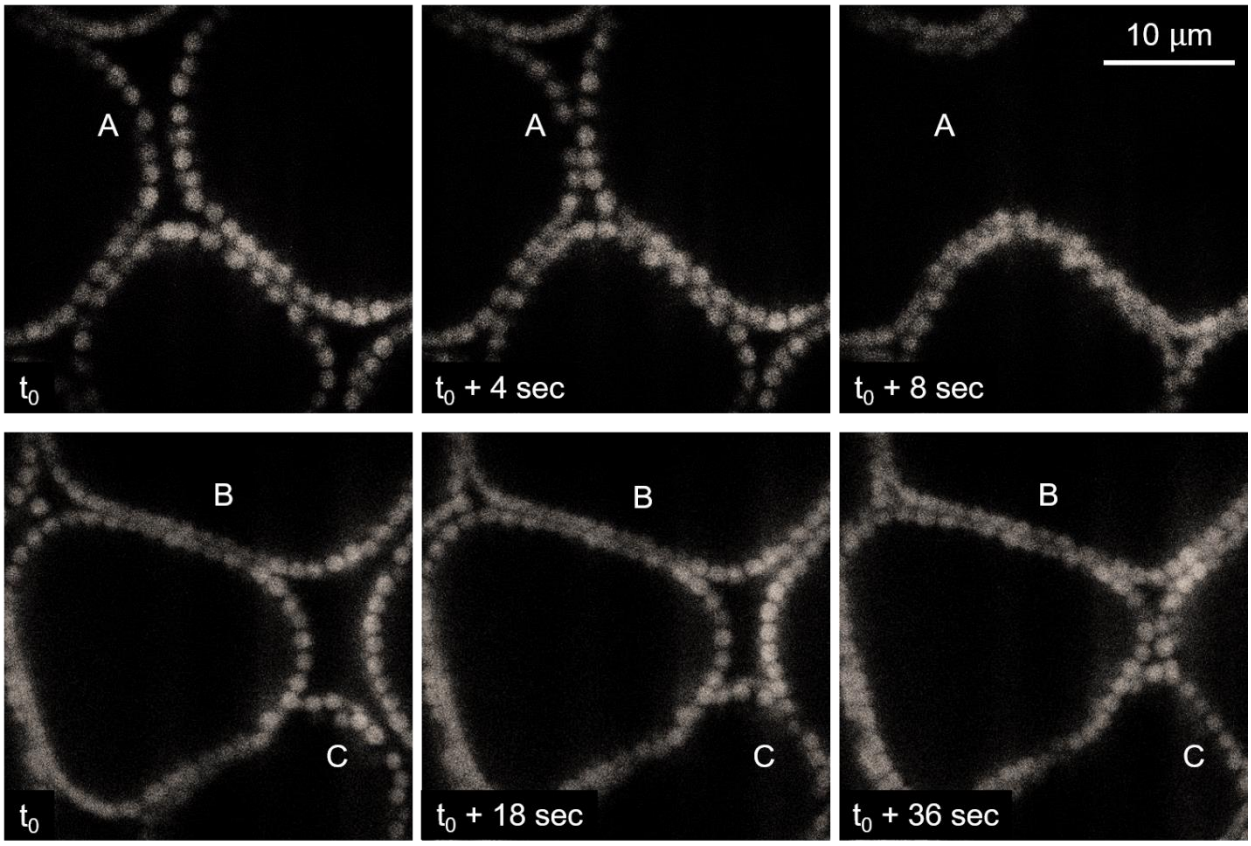

Figure 2.5. Confocal images showing samples, stabilized with 2.20 μm particles, aging to HIPEs. "A" demarks an unstable film that ruptured to result in droplet coalescence, "B" is a stable film with a particle bilayer morphology and "C" illustrates the transition of a particle bilayer to a monolayer in stabilizing an emulsion film. Note these samples are recorded at an intermediate point within their 5 hr aging period and t_0 is time zero of our recording and not the initial time of sample aging.

In the top row, an example of arrested droplet coalescence is shown, as the thin film marked "A" becomes unstable and ruptures. For film "B" in the bottom row, a stable, flat bilayer of particles keeps the droplets stable against coalescence, whereas for film "C", as the particle-laden interfaces are stretched and pressed against each other to accommodate the increase in ϕ_{eff}, a particle monolayer results, bridging two fluid interfaces across a stable film of the continuous phase. It is important to note that the monolayer appears to form via lateral particle rearrangements along the fluid interfaces. Droplet bridging as a mode of particle stabilization has been proposed and experimentally observed by previous researchers[26], [27], [63]. It was highlighted that interparticle interactions play an important role in whether or not a bridged monolayer can form, as they affect particle movements in lateral directions.

Having identified the three different scenarios (film rupture, particle bilayer, and particle monolayer) that can arise during HIPE formation, we approximate the fraction of interfaces exhibiting each scenario, as follows. Our droplet aspect ratio data is used to estimate the fraction of ruptured interfaces, X_r. Since droplets with $\alpha_i > 2$ are argued to have resulted from arrested droplet coalescence, their width, w_i, (measured at the midpoint of the droplet's greatest length, l_i) is taken to represent a ruptured film and X_r is calculated as:

$$X_r = \frac{\sum_1^{N_d(\alpha_i>2)} 2w_i(\alpha_i>2)}{\sum_1^{N_d} \rho_i + \sum_1^{N_d(\alpha_i>2)} 2w_i(\alpha_i>2)} \quad (2.1)$$

In Equation 2.1, ρ_i is an estimated perimeter of each droplet based on its measured aspect ratio. For each sample, four groups of approximately 25 droplets each, from images at random locations, are analyzed, and the average and standard deviation among the four groups are calculated. Please refer to Section 2.5.2 for more details on the aforementioned calculations.

Once X_r is determined, the fraction of unruptured interfaces that are stabilized by a particle monolayer, X_m, is found by analyzing 2D confocal images such as shown in Figure 2.6.

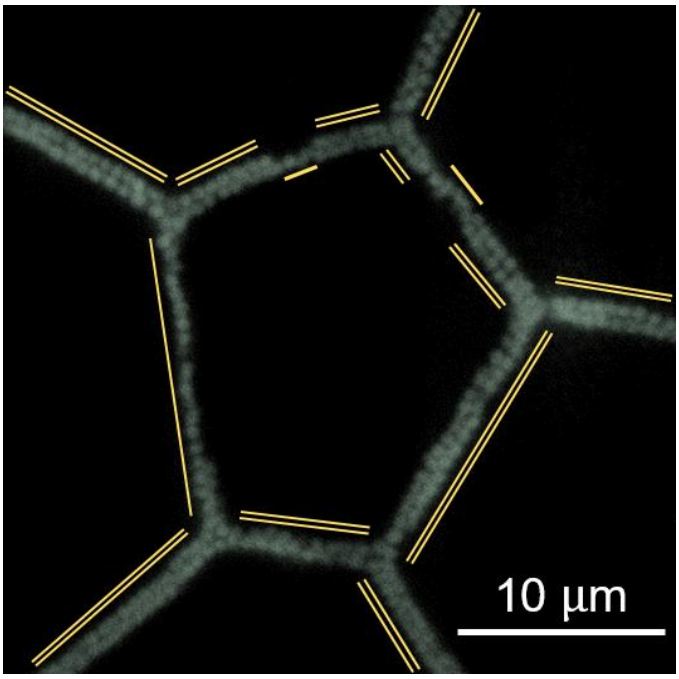

Figure 2.6. A confocal image of a HIPE sample, stabilized with 0.66 μm particles, illustrating the different particle morphologies present in the stable emulsion films.

The lengths of particle monolayers, m_i, and bilayers, b_i, are directly measured in ImageJ software (for each sample, 4 groups of images at 10 random locations are analyzed, giving a total length of ~250 μm for combined monolayers and bilayers in each group), yielding Equation 2.2, with standard deviations calculated to represent variations among the four sets of measurements.

$$X_m = (1 - X_r)\frac{\sum_1^{N_m} m_i}{\sum_1^{N_m} m_i + \sum_1^{N_b} b_i} \tag{2.2}$$

The results of these approximations are shown in Figure 2.7, for samples with $\phi_{eff} > 0.82$ in each emulsion series. Both the fractions of ruptured interfaces, X_r, and particle monolayers, X_m, increase monotonically as ϕ_{eff} rises. This behavior is expected, as these are both mechanisms by which an increase in interfacial area due to droplet deformation can be accommodated.

However, comparing the X_r and X_m variations between the different sample sets, it is apparent that larger particles more readily enable the formation of particle monolayers, whereas film rupture becomes the more likely outcome of droplet deformation with smaller stabilizing particles, at comparable values of ϕ_{eff}. This finding corroborates our earlier observation that larger particles yield greater stability in solid-stabilized HIPEs, and shows that this is likely due to their higher propensity to form particle monolayers. In the next section, we examine the conditions for film rupture in particle bilayers and monolayers, further establishing a connection between monolayer formation and enhanced emulsion stability.

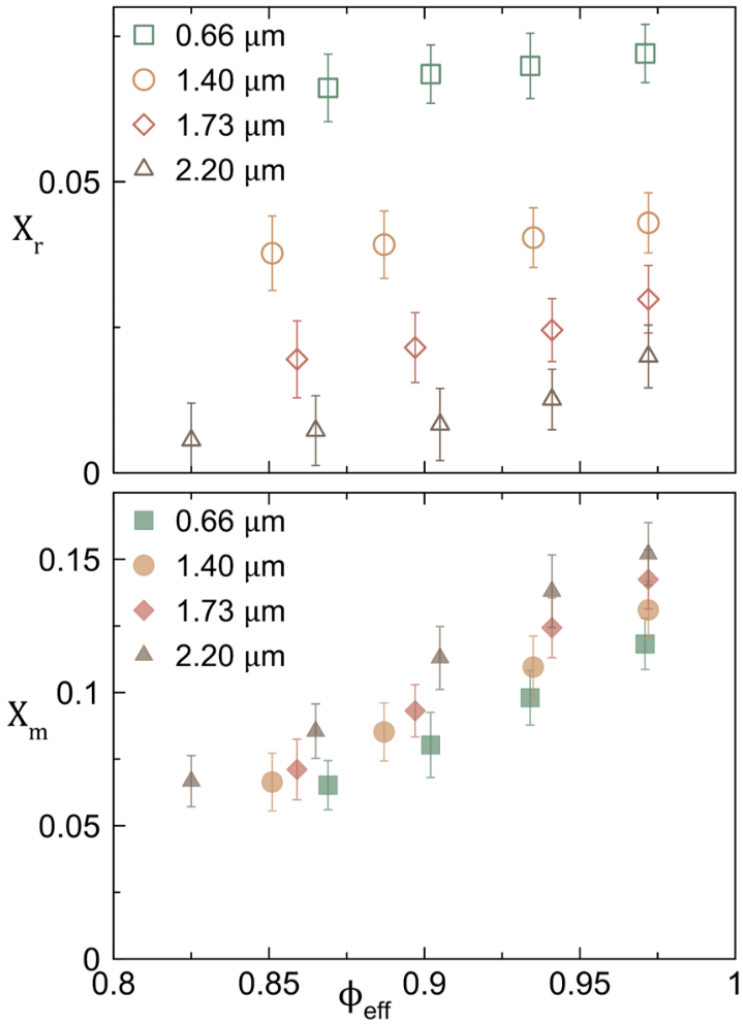

Figure 2.7. The fraction of ruptured interfaces, X_r, (top) and the fraction of droplet interfaces stabilized by particle monolayers, X_m, (bottom) are plotted against the effective dispersed volume fraction, ϕ_{eff}. Error bars denote the standard deviation in X_r and X_m.

2.3.3 Capillary Stabilization

Our experiments have shown that increasing particle size in solid-stabilized HIPEs aids in mitigating droplet coalescence, and results in a greater fraction of interfaces stabilized by particle monolayers. These observations can be reconciled considering the impact of monolayer formation on film stability in HIPEs. To investigate this, we invoke a simple model for a spherical liquid meniscus infiltrating a pore between spherical particles, as shown in Figure 2.8.

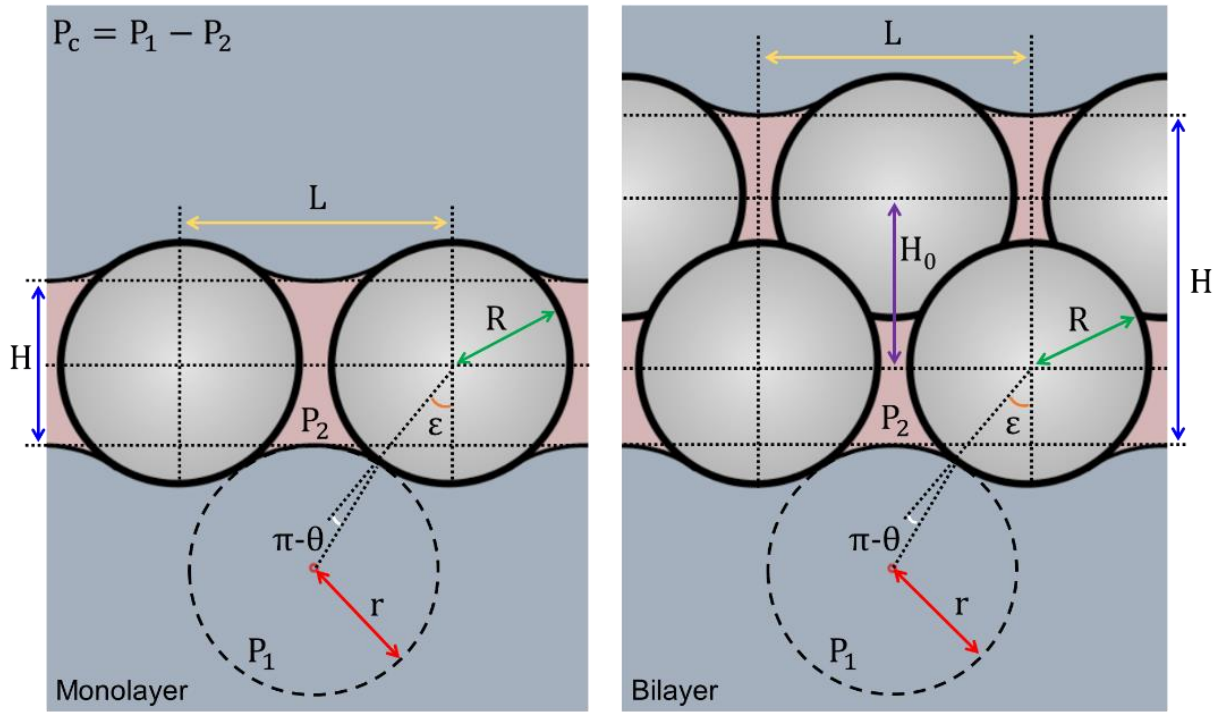

Figure 2.8. Illustrations of the different particle-stabilized films considered in calculating capillary pressure and emulsion film volume. The left image illustrates a bridging particle monolayer, and the right image represents the 3D arrangement of particles in a bilayer.

Our model is inspired by previous investigations of how the capillary pressure across particle-stabilized interfaces varies as a function of film thickness[24], [25], [73], and is built upon the following basic idea. For a given particle radius, R, center-to-center interparticle distance, L, and infiltration angle, ε, the radius of the liquid meniscus, r, that satisfies the equilibrium three-phase contact angle, θ, can be calculated based on geometric arguments. Please

refer to Section 2.5.3 for relevant derivations regarding the liquid meniscus and capillary pressure. The resulting equation for r is shown below.

$$r = \left(\frac{L}{\sqrt{3}} - R\sin(\varepsilon)\right)/\sin\left(\varepsilon - (\pi - \theta)\right) \tag{2.3}$$

With r found and the liquid interfacial tension, σ, known, the capillary pressure associated with the curved liquid meniscus can be calculated, $P_c = {}^{2\sigma}/_{r}$. Defining the normalized capillary pressure as $P_c' = \left({}^{P_c R}/_{2\sigma}\right)$, we have:

$$P_c' = \sin\left(\varepsilon - (\pi - \theta)\right)/\left(\frac{L}{R\sqrt{3}} - \sin(\varepsilon)\right) \tag{2.4}$$

The choice of R in the normalization of P_c' is motivated by the fact that, for a flat arrangement of interfacially-adsorbed particles such as that shown in Figure 2.8, particle size will be the relevant length scale mediating the curvature of the liquid/liquid interface. Note, Equation 2.4 is applicable for films stabilized by either a particle monolayer or bilayer, due to the simplified geometry of the meniscus shape. However, the liquid (oil) film volume, V_o, and total volume of stabilizing particles, V_p, (both similarly determined based on geometry) will vary between the two types of solid-stabilized films. Section 2.5.4 presents detailed volume derivations for each film type. Defining the normalized film volume, $V' = V_o/V_p$, the equation for a monolayer is:

$$V_m' = \frac{\left(\left[\frac{\sqrt{3}}{4}(L)^2\,(S_m)\right] - \left[\frac{2\pi}{3}R^3 - \frac{\pi}{6}(C_m)\left((3(R\sin(\varepsilon))^2) + ((C_m)^2)\right)\right] - \left[\frac{2\pi}{3}(M_m)^2(3r - M_m)\right]\right)}{({}^{2\pi}/_{3})R^3} \tag{2.5}$$

with $S_m = 2R\cos(\varepsilon)$, $C_m = R - R\cos(\varepsilon)$, $M_m = R\cos(\varepsilon) - \frac{H}{2}$, and H the liquid film thickness as defined in Figure 2.8. Similarly, for a bilayer we obtain:

$$V_b' = \frac{\left(\left[\frac{\sqrt{3}}{4}(L)^2\,(S_b)\right] - \left[\frac{4\pi}{3}R^3 - \frac{\pi}{6}(C_b)\left((3(R\sin(\varepsilon))^2) + ((C_b)^2)\right)\right] - \left[\frac{2\pi}{3}(M_b)^2(3r - M_b)\right]\right)}{(4\pi/3)R^3} \qquad (2.6)$$

with $S_b = 2R\cos(\varepsilon) + H_0$, $C_b = R - R\cos(\varepsilon)$, $M_b = R\cos(\varepsilon) + \frac{H_0 - H}{2}$, and H_0 the center-to-center vertical particle separation as defined in Figure 2.8. Equations (2.4), (2.5), and (2.6) allow the capillary pressure within the liquid film to be monitored as the film volume is reduced during HIPE formation. In Figure 2.9, we plot the theoretically calculated P_c' versus the normalized film volume, $V' = V_o/V_p$, for four different scenarios including particle bilayers of various interparticle separations, and a close-packed particle monolayer. Here, CPML, CPBL, and LPBL stand for a close packed monolayer, close packed bilayer, and loosely packed bilayer (of particles), respectively. Generic examples of some of these scenarios occurring in our samples are shown in the accompanying confocal micrographs of Figure 2.9. In calculations of P_c', the three-phase contact angle is fixed at $\theta = 153°$, as measured for our fluid system.

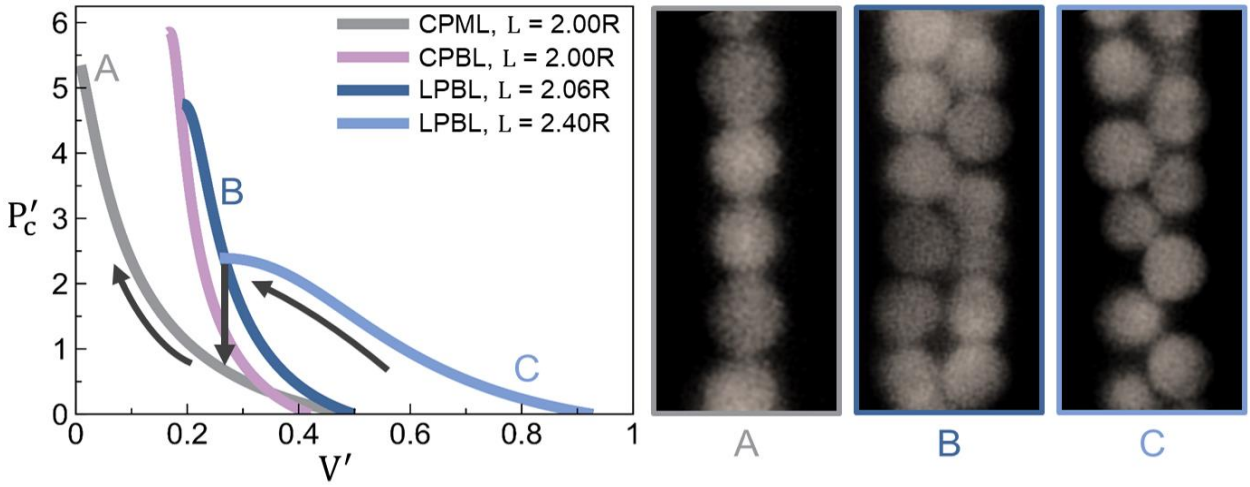

Figure 2.9. Theoretical curves of normalized capillary pressure versus normalized film volume, as defined in the text, for films stabilized by particles in different configurations: close packed monolayer (CPML), close packed bilayer (CPBL) and loose packed bilayer (LPBL). The confocal images show experimental films that illustrate the different films labeled in the capillary pressure plot.

The pressure curves in Figure 2.9 reveal several important points pertaining to film rupture and arrested droplet coalescence in solid-stabilized HIPEs. Each curve displays a

maximum P_c', occurring at a different value of V'. Placed in the context of HIPE preparation, as the volume fraction of the continuous phase is decreased (e.g. by evaporation of a provisional solvent as done in our experiments), initially the meniscus will slide further into the pore to accommodate the reduction in film volume, and simultaneously increase its curvature to maintain the equilibrium three-phase contact angle, resulting in an increase in P_c'. Because of the curved solid walls (particles), there exists a critical V', any further reduction in which would result in a decrease in meniscus curvature to maintain the equilibrium θ, and in turn a drop in P_c'. As such, the corresponding value of V' represents a mechanical stability limit, and sets a criterion for film rupture during HIPE formation. Within this framework, an examination of the different cases in Figure 2.9 provides insightful information on the impact of monolayer formation, which is more commonly seen with larger particles, on HIPE stability. For example, a particle bilayer with average interparticle separation of L=2.40R (Case C in Figure 2.9) will not withstand a reduction in V' below ~ 0.3 (note, however, that the interparticle spacing is not uniform, and locations with greater spacing will be even more prone to rupture). With a reduction in particle spacing to L=2.06R (Case B), the maximum capillary pressure increases significantly, and this arrangement allows further reduction of V' to ~0.2. Most notable, however, is the impact of monolayer formation on film stability. Since our initial droplets are nearly fully covered by particles, we argue that monolayers only form in close-packed arrangement. In other words, the near-complete initial coverage provides ample particles to fully pack the shared interface between two droplets upon monolayer formation, which we have confirmed by examining our confocal micrographs (for example, see Case A in Figure 2.9). Therefore, the transition from a bilayer to a packed monolayer corresponds to a jump from a low-stability curve to Case A in Figure 2.9, which sustains a remarkably low value of V' and a very large maximum P_c'. The

details of such a transition depend on the interparticle separations in the bilayer. However, one representative path is schematically shown by arrows in Figure 2.9, for illustrative purposes. It is worth noting that a close packed bilayer can sustain an even higher maximum capillary pressure than a monolayer, but this will occur at $V' \sim 0.2$, and any further increase in the dispersed phase volume fraction (reduction in V') will result in film rupture, whereas a monolayer enables reduction of V' to miniscule values with a large associated value of P_c'. Recall that our experiments showed a higher tendency for monolayer formation, and a smaller fraction of ruptured interfaces, when large particles are used to stabilize HIPEs. Our theoretical calculations demonstrate that, through monolayer formation, solid-stabilized HIPEs are able to withstand a larger capillary pressure and a lower volume fraction of the continuous phase without loss of stability. Therefore, our findings establish a better understanding of how increasing particle size can enhance the stability of solid-stabilized HIPEs. Importantly, this result contrasts the stability considerations for dilute solid-stabilized emulsions, where the use of small particles is generally recommended because of higher interfacial elasticity (stronger capillary attractive interactions) and faster adsorption kinetics[68], [79]. We argue that in HIPE formation, the weaker capillary attractive interactions associated with larger particles are indeed beneficial, as they more easily allow the reorganization of particles into a staggered configuration for monolayer formation. Other modes of interparticle interactions, especially long-range electrostatic forces, can also influence the particle dynamics and configurations as the droplets are concentrated into a HIPE state[26], [27]. To rigorously examine this notion, future research must investigate the interfacial rheology of particle-laden interfaces and the dynamics of particle rearrangements during deformation modes relevant to HIPE formation, and address the role of particle size in mediating the associated dynamics. Before closing, we must note that the capillary pressure model utilized

in this study is static in nature, while film rupture can also involve several dynamic and kinetic factors[74]. Given that our sample preparation timescales are on the order of several hours, we believe that the use of a static model as a first approximation is warranted. For scenarios involving rapid transitions from a dilute emulsion to a HIPE, for example by filtration[80], the dynamics of film drainage and rupture should also be considered to obtain a more realistic picture.

2.4 Summary

We have characterized the microstructures of four different solid-stabilized HIPE series to investigate the impact of particle size on droplet stability against coalescence at high dispersed volume fractions. We unveiled a systematic trend, where the use of smaller particles resulted in a higher probability of ruptured films and partially coalesced droplets, whereas larger particles resulted in a higher fraction of bridged particle monolayers between neighboring droplets. We adopted a simple model of film rupture based on previous investigations, which established a connection between monolayer formation and film stability at high volume fractions of the dispersed phase. Collectively, these findings demonstrate that the use of larger particles will enhance the stability of solid-stabilized HIPEs. As has been proposed by other researchers, the morphology that colloids adopt in stabilizing a liquid film between droplets is influenced by their interactions along the same droplet interface, as well as those with particles across the liquid film[26]. Our study indicates that these interactions can be tuned with particle size, and provides useful insights for the formulation of solid-stabilized HIPEs and how particles can influence their stability. Finally, our work introduces new questions for future research in this area to better understand how the dynamics of monolayer formation is mediated by the interfacial rheology of particle-laden interfaces.

2.5 Supporting Information

2.5.1 Supplementary Figures and Videos

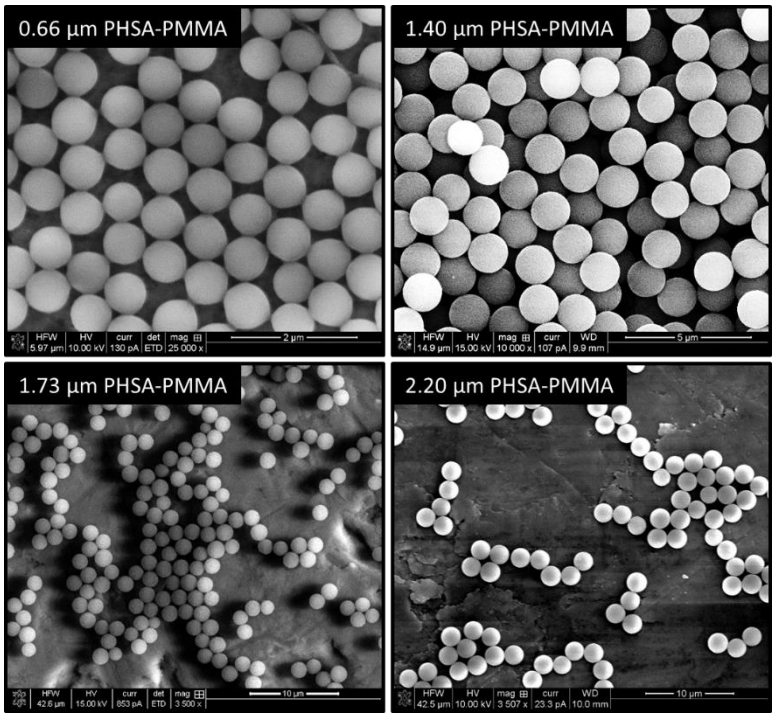

Figure S2.1. Scanning electron microscopy images of each particle batch utilized within the study of Chapter 4. Particles were initially suspended in and cast out of dodecane.

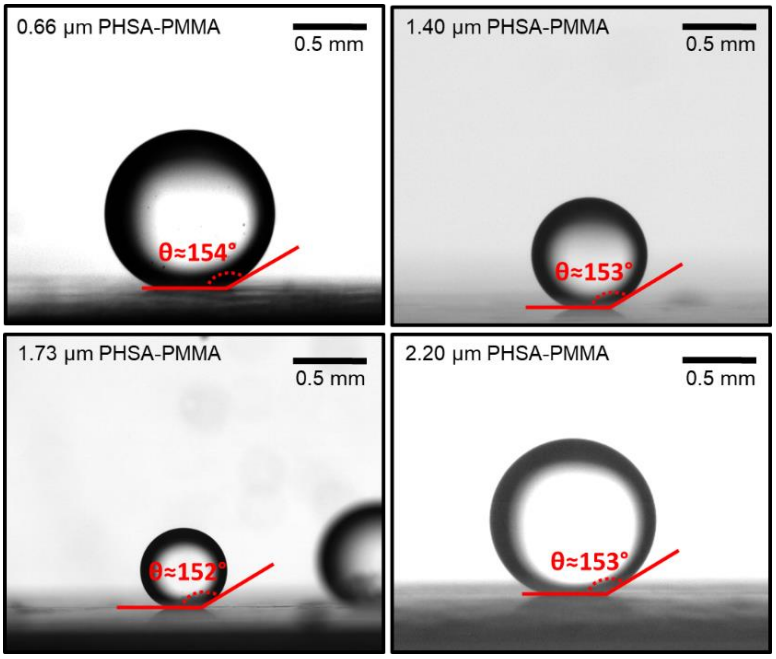

Figure S2.2. The average static contact angle measured by the immersed droplet method for each batch of particles used in the study. In this method an aqueous droplet sits on a glass coverslip, coated with particles by drop casting, within the organic fluid phase.

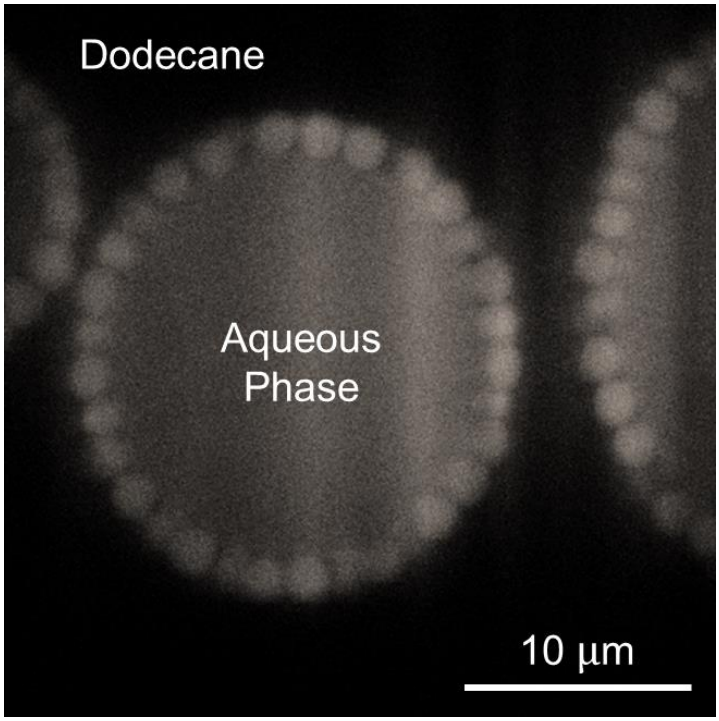

Figure S2.3. The formation of water-in-oil emulsions is confirmed by selectively dying the aqueous phase with rhodamine B fluorescent dye, which allows it to be distinguished from dodecane via confocal imaging.

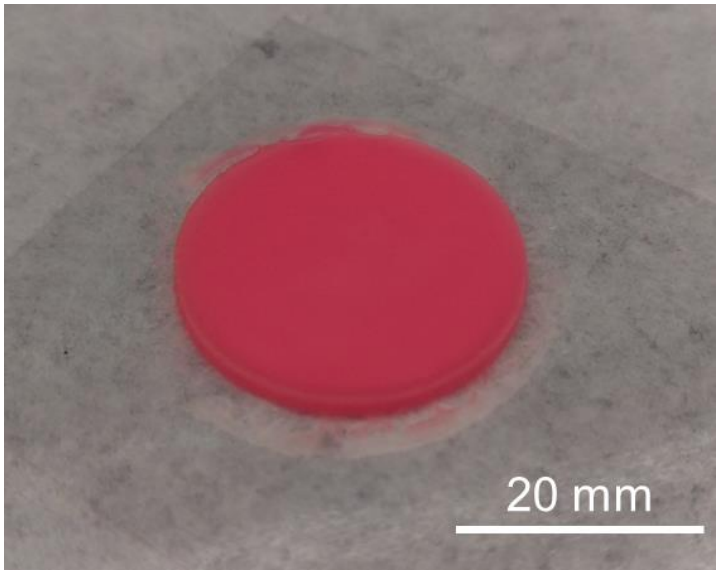

Figure S2.4. A characteristic emulsion sample, stabilized by PHSA-grafted PMMA particles. The sample shown has been aged for 5 hours to allow the evaporation of hexane, and the cylindrical tube it was initially surrounded by has been removed. The disk-shaped sample has a diameter of 25 mm and height ~1 mm.

Video files are available free of charge on the ACS Publications website at:
http://pubs.acs.org/doi/abs/10.1021/acs.langmuir.9b02223

V2.1: 32 × 32 μm video showing the z-stack of a particle coated droplet, 1 um step size, playback is at 6 fps (AVI)

V2.2: 157 × 157 μm video of an emulsion exhibiting droplet coalescence events during sample aging, played at 60x real time (AVI)

V2.3: 32 × 32 μm video of a film rupturing between droplets during sample aging, played at 3x real time (AVI)

V2.4: 32 × 32 μm video of a stable particle bilayer, as well as a transition to a monolayer, observed during sample aging, played at 3x real time (AVI)

2.5.2 Interface Fraction Calculations

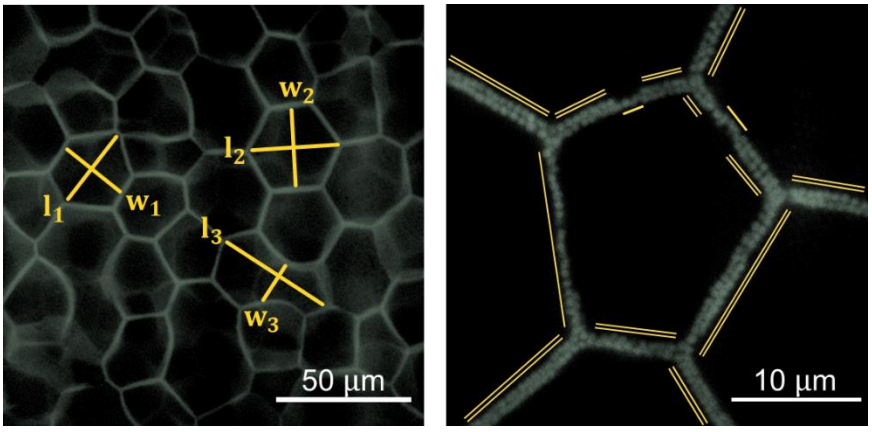

Figure S2.5. A high internal phase emulsion sample imaged with a 20X objective (left) and a 100X objective (right).

Figure S2.5 shows confocal images of an experimental sample, taken at different magnifications. As discussed within sections 2.2.3 and 2.3.1, and illustrated in Figure S2.5, droplet aspect ratios can be quantified from the images taken with a 20X objective. For each droplet, l_i and w_i represent its greatest length and width, respectively, while the ratio of the two is its aspect ratio, α_i (Note that w_i, is measured perpendicular to l_i at its median). This data has been recorded for ~50 droplets in each experimental sample. For high internal phase emulsion (HIPE) samples, $\phi_{eff} > 0.80$, images were also taken with a 100X objective, which allow visual observation of the different particle stabilized interfaces present. Here we will show how we can estimate the fraction of interfaces that had ruptured in our HIPE samples, as well as the fraction of interfaces that are stabilized by either a particle monolayer or particle bilayer. From the droplet aspect ratio analysis done in Section 2.3.1, it was argued that droplets with an aspect ratio greater than 2 were a result of droplet coalescence. The total length of interfaces that constituted unstable films which ruptured is taken as twice the sum of w_i for all droplets with aspect ratios greater than 2.

$$L_r = \sum_1^{N_d(\alpha_i>2)} 2w_i(\alpha_i > 2) \quad \text{(S2.1)}$$

To determine the total length of stable interfaces in a HIPE sample the perimeters of all the droplets, examined for their aspect ratio, are estimated and summed.

$$L_s = \sum_1^{N_d} \rho_i \tag{S2.2}$$

The perimeter of each droplet, ρ_i, is evaluated by taking its l_i and w_i as the major and minor axis of an ellipse, respectively, and utilizing the Ramanujan approximation shown below.

$$\rho_i \approx \pi(l_i + w_i)\left(1 + \frac{3\lambda}{10+\sqrt{4-3\lambda}}\right) \tag{S2.3}$$

The parameter λ is given by the following.

$$\lambda = \frac{(l_i - w_i)^2}{(l_i + w_i)^2} \tag{S2.4}$$

The fraction of ruptured interfaces, X_r, is written out as seen in Section 2.3.2 (Equation 2.1), by utilizing equations S2.1 and S2.2.

$$X_r = \frac{\sum_1^{N_d(\alpha_i>2)} 2w_i(\alpha_i>2)}{\sum_1^{N_d} \rho_i + \sum_1^{N_d(\alpha_i>2)} 2w_i(\alpha_i>2)} \tag{S2.5}$$

Equation S2.5 was utilized in generating the error bars shown in Figure 2.7 of Section 2.3.2. For each sample plotted in Figure 2.7, four different sets of ~25 droplets were analyzed for their droplet aspect ratio data, used to estimate X_r. The average and standard deviation of these four values are plotted in Figure 2.7.

In order to calculate the fraction of stable interfaces, 1-X_r, that are stabilized by either a particle monolayer or bilayer, sample images taken with the 100X objective are analyzed. As seen in Figure S2.1, the different films are denoted by single lines for monolayers and double lines for bilayers. Their respective lengths, m_i and b_i, are summed up to give the total amount of monolayer and bilayer stabilized interfaces, as shown below.

$$L_m = \sum_1^{N_m} 2m_i \quad \text{(S2.6)}$$

$$L_b = \sum_1^{N_b} 2b_i \quad \text{(S2.7)}$$

The film lengths in Equations S2.6 and S2.7 are multiplied by 2 to capture the two droplet interfaces present in each film. For each sample the total amount of L_m and L_b analyzed is ~1000 μm. Equations S2.5-S2.7 are used to express the fraction of interfaces stabilized by particle monolayers, X_m, as found in Section 2.3.2 (Equation 2.2).

$$X_m = (1 - X_r)\frac{\sum_1^{N_m} m_i}{\sum_1^{N_m} m_i + \sum_1^{N_b} b_i} \quad \text{(S2.8)}$$

For the samples plotted in Figure 2.7, four different sets of L_m and L_b were measured, each summing up to ~250 μm, to evaluate X_m (The average X_r for each sample was used in calculating X_m). The average and standard deviation of these four X_m values are plotted in Figure 2.7. Note, the fraction of particle bilayer stabilized interfaces, X_b, can be determined from X_r and X_m.

$$X_b = 1 - X_r - X_m \quad \text{(S2.9)}$$

2.5.3 Capillary Pressure Calculations

Our derivation for the capillary pressure that arises during the thinning of a liquid film between particle-coated droplets follows the theoretical model reported by G. Kaptay[24]. This model simplifies the shape of the menisci infiltrating the pores formed between neighboring interfacial particles, allowing the capillary pressure at different extents of film thinning to be evaluated geometrically. Two configurations are considered for the stabilizing particles present in the liquid film between droplets: particle monolayer and particle bilayer. For both, the meniscus going through a pore created by three spherical particles is approximated as a segment of a sphere (spherical cap). The two particle configurations are illustrated below in Figure S2.6 (Figure 8 of Section 2.3.3). Note, the illustrations show a cross-sectional view of the particle-stabilized films, where the two droplets interfaces are at the top and bottom of the particle layers.

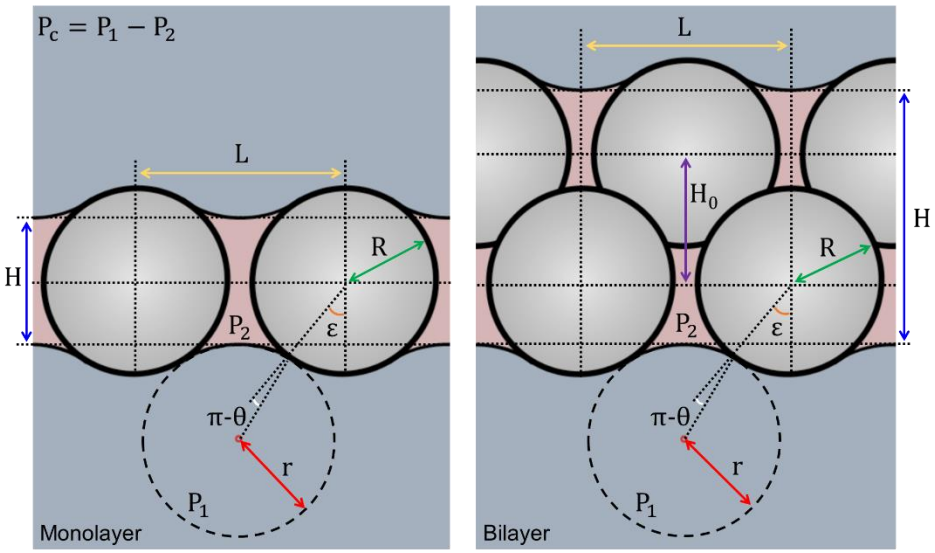

Figure S2.6. Illustrations of the two configurations in which particles can stabilize the liquid film formed between two droplets.

The known or set parameters in Figure S2.6 are: separation distance between particle centers, L, particle radius, R, infiltration angle, ε, and particle contact angle, θ, as measured against the aqueous fluid phase (the dispersed phase for our experimental system). P_1 represents the pressure

in the droplet phase and P_2 is the pressure in the liquid film. Capillary pressure, P_c, is the difference between P_1 and P_2. At the lowest possible ε, $\varepsilon_0 = \pi - \theta$, the capillary pressure is zero and the meniscus is flat. To determine P_c at a degree of infiltration above ε_0 the assumed spherical shape of the infiltrating meniscus, and Young-Laplace equation are utilized. First, the radius of the sphere that the meniscus is taken to be a segment of, r, is determined geometrically. Its equation at a specified ε is given below.

$$r = \left(\frac{L}{\sqrt{3}} - R\sin(\varepsilon)\right) / \sin\left(\varepsilon - (\pi - \theta)\right) \tag{S2.10}$$

Once r is determined, the Young-Laplace equation is employed to calculate P_c as shown below.

$$P_c = \frac{2\sigma}{r} \tag{S2.11}$$

Here σ represents the interfacial tension between the fluids in the droplet and film. Scaling P_c by $2\sigma/R$ gives the equation for the dimensionless capillary pressure, P_c', as reported in Section 2.3.3 (Equation 2.4).

$$P_c' = \sin\left(\varepsilon - (\pi - \theta)\right) / \left(\frac{L}{R\sqrt{3}} - \sin(\varepsilon)\right) \tag{S2.12}$$

It is important to note that with the simplified model used, Equation S2.12 applies for films stabilized by either a particle monolayer or bilayer. Though the same P_c' is found at a set ε, for either particle configuration, the film thickness, H, at which this occurs will differ. As with r, an equation for a H can be geometrically derived for either film type as given below.

$$H_m = 2R\cos(\varepsilon) + 3\left(\frac{L}{\sqrt{3}} - R\sin(\pi - \theta)\right)\left(\cot\left(\varepsilon - (\pi - \theta)\right) - \frac{1}{\sin(\varepsilon - (\pi - \theta))}\right) \tag{S2.13}$$

$$H_b = H_m + H_0 \tag{S2.14}$$

Equation S2.13 gives the thickness of a film stabilized by a particle monolayer, H_m, while Equation S2.14 is for a bilayer stabilized film, H_b. In Equation S2.14, H_0 represents the distance between the medians of each particle layers found in a film stabilized by a bilayer, as seen in Figure S2.6. H_0 depends on the interparticle separation in the two particle layers as found below.

$$H_0 = \sqrt{4R^2 - \left(\frac{L}{\sqrt{3}}\right)^2} \tag{S2.15}$$

Note at the limit $L = 2R\sqrt{3}$, $H_0 = 0$, meaning the interparticle separation is such that the two particle layers can merge to form a monolayer. Though equations for film thickness have been presented, in our analysis of the difference in stability between monolayer and bilayer stabilized films we do not compare the two film types on this basis. Rather, we argue a volumetric basis is most appropriate for comparing between the two types of films at a consistent degree of film thinning. In Section 2.5.4 we outline the equations derived to estimate film volume at different infiltration angles. We may not explicitly consider film thickness, but Equations S2.13 – S2.15 are utilized within our film volume calculations.

2.5.4 Film Volume Calculations

In order to adequately compare between films stabilized with either a particle monolayer or bilayer, we examine their thinning behavior on a volumetric basis instead of film thickness. The parameter V' represents the volume of the continuous fluid phase (oil phase for our experimental system) present in the film, scaled by the total volume of particles stabilizing the film, $\mathrm{V_p}$. Shown below is the general equation used to evaluate V'.

$$\mathrm{V'} = \frac{(\mathrm{V_t} - \mathrm{V_s} - \mathrm{V_a})}{\mathrm{V_p}} \tag{S2.16}$$

Here we derive the explicit equations for the parameters seen in Equation S2.16, which are defined as follows: total volume of a measured film segment, $\mathrm{V_t}$, the volume of solid particles present in the segment, $\mathrm{V_s}$, and dispersed fluid phase volume present due to the spherical menisci, $\mathrm{V_a}$ (aqueous phase in our experimental system). In outlining the geometric arguments made to derive these volumetric parameters, references to equations in Section 2.5.3 are made. In Figure S2.7, the unit cells considered for each film type are represented, as viewed from above the particle layer(s).

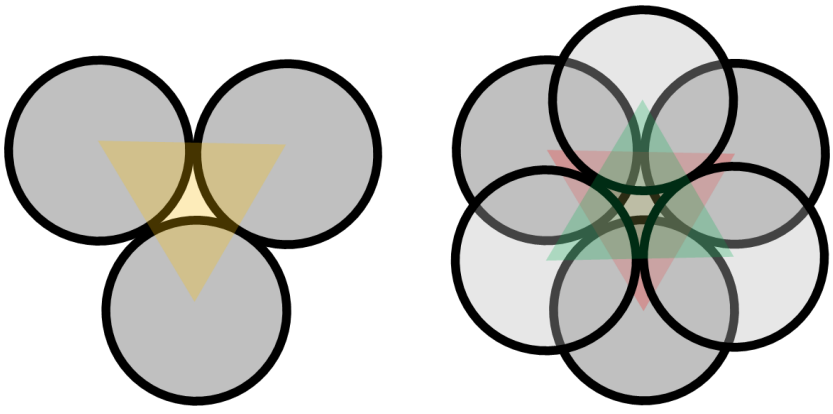

Figure S2.7. The unit cell for a film stabilized by either a particle monolayer (left) or particle bilayer (right) is denoted by the shaded triangles, as viewed from above the particle layer(s).

The yellow shaded triangle, in Figure S2.7, outlines the unit cell for a particle monolayer film. The same cell stacked upon itself to create an octahedral hole/pore between the two particle layers, gives the unit cell for a film stabilized by a bilayer, as denoted by the red and green shaded triangles. From these unit cells the total volume of stabilizing particles for a monolayer, V_{pm}, and bilayer film, V_{pb}, are determined, noting the spherical particle segments contained within them.

$$V_{pb} = 2V_{pm} = \frac{4\pi}{3}R^3 \tag{S2.17}$$

We will first consider the derivation of Equation S2.16 for a film stabilized by a particle monolayer, as illustrated in Figure S2.8 below.

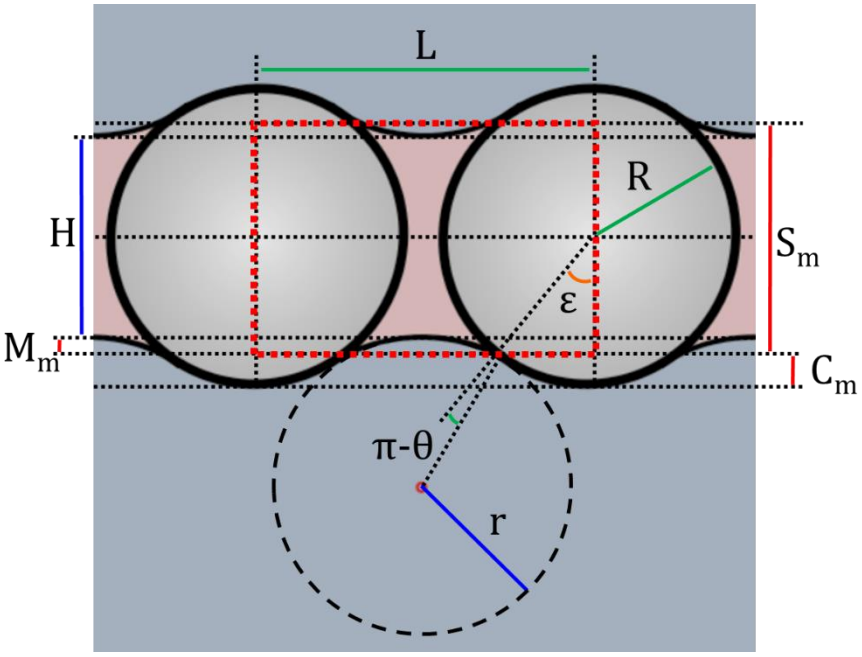

Figure S2.8. An illustration of film stabilized by a particle monolayer.

In the Figure S2.8, the known or set parameters are: separation distance between particle centers, L, particle radius, R, infiltration angle, ε, and particle contact angle, θ, as measured against the aqueous fluid phase (the droplet phase for our experimental system).

The film segment considered for Equation S2.16 is outlined by the red dashed lines. We can determine the total segment volume for a monolayer stabilized film, V_{tm}, by first evaluating its height, S_m, geometrically from Figure S2.8.

$$S_m = 2R\cos(\varepsilon) \tag{S2.18}$$

V_{tm} can then be calculated, recalling that the segment will have a triangular base as seen in Figure S2.7, with side lengths set by L.

$$V_{tm} = \frac{\sqrt{3}}{4}\,(L)^2\,(S_m) \tag{S2.19}$$

The volume in the film segment that is due to the presence of the stabilizing particles, V_{sm}, is also determined geometrically. From Figure S2.7, we note that the spherical particles are 1/6 segments within the unit cell. The height of the particle's spherical caps, C_m, not included in the film segment is governed by ε, as shown below.

$$C_m = R - R\cos(\varepsilon) \tag{S2.20}$$

Since the volume of a sphere and spherical cap is known, we can derive an equation for V_{sm}, the particle volume that is included in our evaluation of V_{tm}.

$$V_{sm} = \frac{2\pi}{3}R^3 - \frac{\pi}{6}(C_m)\left((3(R\sin(\varepsilon))^2) + ((C_m)^2)\right) \tag{S2.21}$$

Note in Figure S2.8, due to the curvature of the infiltrating meniscus some dispersed fluid is included in the total segment volume. To calculate the volume present due to the dispersed fluid phase, V_{am}, the radius of the spherical meniscus, r, and film thickness, H, are first determined (recall Equations S2.10 and S2.13). The height of the meniscus cap, M_m, included in the film segment can be expressed once H is known.

$$M_m = R\cos(\varepsilon) - \frac{H}{2} \tag{S2.22}$$

As with V_{sm}, the equations for the volume of a sphere and spherical cap are used to derive V_{am}.

$$V_{am} = \frac{2\pi}{3}(M_m)^2(3r - M_m) \tag{S2.23}$$

With equations for V_{pm}, V_{tm}, V_{sm}, and V_{am} found, Equation S2.16 can be rewritten for a film stabilized by a particle monolayer.

$$V'_m = \frac{\left(\left[\frac{\sqrt{3}}{4}(L)^2\,(S_m)\right] - \left[\frac{2\pi}{3}R^3 - \frac{\pi}{6}(C_m)\left((3(R\sin(\varepsilon))^2) + ((C_m)^2)\right)\right] - \left[\frac{2\pi}{3}(M_m)^2(3r - M_m)\right]\right)}{(2\pi/3)R^3} \tag{S2.24}$$

The same procedure is followed to derive an equation similar to Equation S2.24 for a film stabilized by a particle bilayer, accounting for the additional film thickness due to H_0, as seen in Figure S2.9.

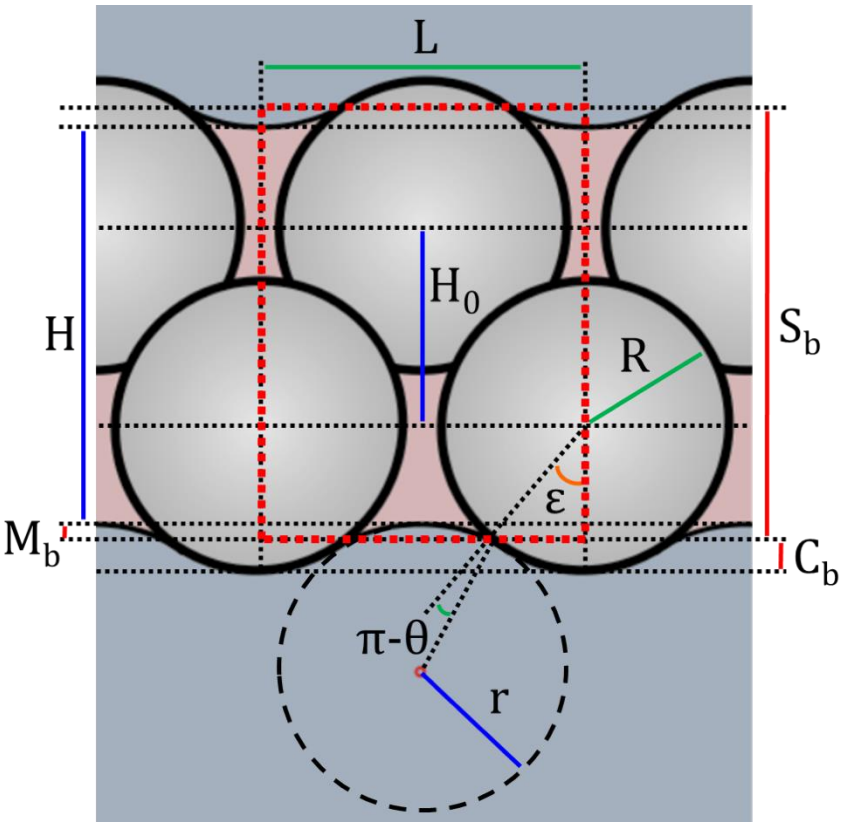

Figure S2.9. An illustration of film stabilized by a particle bilayer.

In the Figure S2.9, the known or set parameters are: separation distance between particle centers, L, particle radius, R, infiltration angle, ε, and particle contact angle, θ, as measured against the aqueous fluid phase (the droplet phase for our experimental system). The height of the film segment, S_b, outlined by the dotted red lines in Figure S2.9, is given below. Recall that H_0 depends on L as was shown in Equation S2.15.

$$S_b = 2R\cos(\varepsilon) + H_0 \tag{S2.25}$$

The total film segment volume, V_{tb}, for a bilayer film is calculated as follows.

$$V_{tb} = \frac{\sqrt{3}}{4}\,(L)^2\,(S_b) \tag{S2.26}$$

The volume included in V_{tb}, due to the presence of the stabilizing particles, V_{sb}, is computed considering the volume of spheres and spherical caps, as was done with a monolayer film. Equations for C_b, the height of the particle spherical caps not included in the film segment, and V_{sb} are shown below.

$$C_b = R - R\cos(\varepsilon) \tag{S2.27}$$

$$V_{tb} = \frac{4\pi}{3}R^3 - \frac{\pi}{6}(C_b)\left((3(R\sin(\varepsilon))^2) + ((C_b)^2)\right) \tag{S2.28}$$

V_{ab}, the dispersed fluid phase present in the total segment volume is also determined considering the volume of spheres and spherical caps. As was done with the monolayer film, the radius of the spherical meniscus, r, and film thickness, H, are first calculated (recall Equations S2.10 and S2.14). These are used to derive expressions for the height of the meniscus cap, M_b, included in the film segment and V_{ab}, as seen below.

$$M_b = R\cos(\varepsilon) + \frac{H_0 - H}{2} \tag{S2.29}$$

$$V_{ab} = \frac{2\pi}{3}(M_b)^2(3r - M_b) \tag{S2.30}$$

With the equations for V_{pb}, V_{tb}, V_{sb}, and V_{ab} derived, Equation S2.16 can be rewritten for a film stabilized by a particle bilayer.

$$V_b' = \frac{\left(\left[\frac{\sqrt{3}}{4}(L)^2\,(S_b)\right] - \left[\frac{4\pi}{3}R^3 - \frac{\pi}{6}(C_b)\left(\left(3(R\sin(\varepsilon))^2\right) + \left((C_b)^2\right)\right)\right] - \left[\frac{2\pi}{3}(M_b)^2(3r - M_b)\right]\right)}{\left(4\pi/3\right)R^3} \tag{S2.31}$$

Equations S2.24 and S2.31 are used with Equation S2.12 to generate the nondimensional capillary pressure plots in Figure 2.9.

CHAPTER 3: ROLE OF PARTICLES IN THE RHEOLOGY OF SOLID-STABILIZED HIGH INTERNAL PHASE EMULSIONS

3.1 Background

Emulsions are mixtures of two immiscible fluid phases, with droplets of one phase typically dispersed within a continuous body of the other. The large, energetically unfavorable interfacial area created by these droplets makes most emulsions thermodynamically unstable, often relying on surfactant molecules to provide kinetic stability against droplet coalescence[6], [81]. Alternatively, as Ramsden[18] and Pickering[19] independently observed more than a century ago, fine solid (colloidal) particles can be used instead of surfactants to stabilize emulsions. This strategy has been utilized in emulsion formulation over the decades, and recent work has suggested that solid particles can enhance emulsion stability by providing steric hindrance to droplet coalescence, mitigating Ostwald ripening/droplet coarsening, and inhibiting film drainage[82], [83]. Both surfactant- and solid-stabilized emulsions are found in various consumer products and technological applications such as agrochemicals, pharmaceuticals, paints, cosmetics, food formulations, and enhanced oil recovery[6], [81], [33], [84]–[86]. Moreover, porous materials derived from emulsions find applications in tissue engineering, separations, catalysis, and electrochemical sensing[12], [87]–[90]. The performance of emulsions in many of these applications is heavily influenced by their rheology, which governs their mechanical stability and shelf life, texture, and processing conditions. Therefore, understanding how to manipulate emulsion rheology is important in the refinement and optimization of such products, especially in concentrated systems where inter-droplet interactions can result in remarkable viscoelasticity[31]. The rheology of surfactant-stabilized emulsions has received ample consideration in the scientific literature[28], [29], [32], [42], [91].

However, the same is not true for solid-stabilized systems. This points to an important knowledge gap in the field, because the use of particles in lieu of surfactant molecules can alter emulsion rheology in fundamental ways that need to be better understood to further drive and expand their technological applications.

Early studies have reported the salient physicochemical variables that influence the rheology of surfactant-stabilized emulsions, such as the viscosities and volumetric ratio of the constituent phases, and inter-droplet interactions[28], [48], [91]–[93]. One of the more important parameters revealed is the volume fraction of the dispersed phase, ϕ_D. As ϕ_D is increased from below to above a critical $\phi_{D,c} = 0.64$, a relatively sharp transition from viscous (liquid-like) to mostly elastic (solid-like) behavior is observed[28], [39]. It is important to recognize that this solid-like rheology emerges in a system that is comprised entirely of liquids (and surfactant molecules), which can be explained in the context of arrested dynamics and resistance to deformation in a concentrated emulsion. Above $\phi_{D,c}$, low applied stresses result in droplet deformation (but no rearrangement due to caging by neighboring droplets), which is resisted by surface tension, storing energy at droplet interfaces and giving rise to an elastic strain[28], [39]–[41]. With surfactant-stabilized emulsions, a universal scaling of emulsion elasticity, as measured by its zero-shear elastic modulus normalized by the Laplace pressure of the dispersed droplets, was reported for $\phi_D > 0.64$[56]. The Laplace pressure scaling implies that in these systems, elasticity is governed by droplet deformation, particularly the system's tendency to resist the accompanying increase in interfacial area, and interactions other than excluded volume between droplets are typically negligible[31], [94]. Such concentrated emulsions feature microstructures spanning from close-packed spherical to highly faceted droplets. Systems with $\phi_D > 0.74$ are often defined as high internal phase emulsions (HIPEs)[11], though it has been

suggested that the definition should be extended to include ϕ_D as low as ~ 0.60[95]. As we will reveal shortly, ϕ_D alone does not provide enough information to make this distinction in our ternary systems. Therefore, to stay in accord with previous definitions, here the term HIPE is used in reference to emulsions with $\phi_D < 0.40$, where ϕ_C denotes the volume fraction of the continuous fluid phase. Preliminary studies on solid-stabilized HIPEs have noted a similar rheological transition as reported previously, with the mixture's elastic modulus rapidly rising past a critical dispersed volume fraction, albeit to values generally larger than those observed in surfactant-based emulsions[30], [96]. The greater elasticity in these studies was attributed to lateral interparticle interactions along the droplet interfaces, absent in surfactant-stabilized systems. This may be one ramification of having particle-laden interfaces in emulsions. But considering the differences between particles and surfactants, we believe two other mechanisms specific and unique to solid-stabilized emulsions can influence (and be used to control) their rheology. First is the significant difference in size between the stabilizing species (colloidal particles versus surfactant molecules), which can lead to pronounced and tunable excluded volume effects in solid-stabilized HIPEs. Namely, the presence of colloidal particles on droplet interfaces can appreciably alter the effective volume fraction of the dispersed phase, especially when the droplet-to-particle size ratio is not too large, thereby influencing the transition to arrested dynamics and solid-like rheology. Second, consider how colloidal interactions in particulate suspensions can lead to the formation of viscoelastic materials that have no molecular analog, namely colloidal gels[97], [98]. In a similar manner, attractive interparticle interactions through the continuous phase may influence HIPE rheology (note this mode of attraction concerns interactions between particles attached to the surfaces of different droplets, and is fundamentally distinct from the lateral capillary interactions along the droplet interface

mentioned earlier). However, the influences of excluded volume and attractive colloidal interactions on the rheology of solid-stabilized emulsions have not been systematically considered and characterized yet. To this end, our study reports the rheological behavior of four solid-stabilized emulsion systems, formulated with particles of different sizes or surface chemistries, over a broad range of sample compositions. The mechanical properties and microstructures of these emulsions are characterized by dynamic oscillatory rheology and confocal microscopy, respectively. Similar to surfactant-stabilized HIPEs, the zero-shear elastic modulus is shown to be tunable by manipulating sample composition, for example through ϕ_D. However, with solid-stabilized systems, the solids loading can be used in ways previously unrevealed, to tune rheological behavior. Considering the microstructural and rheological transitions of these samples, we determine the first of three consequences of colloid-laden interfaces on emulsion rheology: The particle excluded volume is significant, and an effective volume fraction of the dispersed phase must be defined to take this into account and properly normalize the data. Second, interparticle interactions through the continuous phase can influence the rheology of solid-stabilized HIPEs, resulting in finite elasticity even at moderate volume fractions. The third consequence is the presence of lateral capillary interparticle interactions along the fluid interfaces. Previous studies have suggested the general need to consider these interactions and their impact on the interfacial energy of particle-stabilized droplets[30]. However, they have not addressed how such interactions can influence solid-stabilized HIPEs, where thin films of the continuous fluid separate droplet interfaces covered with particles.

In our study, the wide physicochemical space available for engineering the elasticity of solid-stabilized HIPEs is systematically traversed, as emulsions stabilized by particles of different sizes and surface chemistries are examined at varying mixture compositions. We show

that the composition of solid-stabilized HIPEs can be employed to tune their rheology over an extensive range, and rationalize our data employing concepts previously developed for surfactant-stabilized emulsions, considering the aforementioned three consequences of using solid particles in lieu of surfactants. Our study provides a foundation for understanding the rheology of the broader class of particle-stabilized emulsions such as bicontinuous interfacially jammed emulsion gels (bijels)[34], [99], as well as important guidelines for tuning the mechanical properties of particulate multiphase systems in industrial applications and product formulation.

3.2 Experimental Methods

3.2.1 Sample Formation

Solid-stabilized emulsions were created by using colloidal particles to stabilize droplets of a 65:35 v/v mixture of dimethyl sulfoxide (99.9% Alfa Aesar) and deionized water (Millipore), hereon referred to as the aqueous phase, within a continuous oil phase of dodecane (99% Sigma Aldrich). Our choice of these particular fluid mixtures was steered by the requirement to achieve the following: 1) ability to stabilize spherical monodispersed aqueous droplets with both silica and PHSA-PMMA particles, 2) ability to image samples via Confocal Microscopy, and 3) ability to instigate a gradual and uniform increase in the dispersed phase volume fraction from dilute to any final desired concentration, by selective evaporation of one component in the continuous phase. The four-component fluid system we used was able to adequately meet all three conditions, as will be shown and discussed below. A force tensiometer (Sigma 701) was used to measure the interfacial tension between the aqueous and oil phases to be $\sigma = 25$ mN/m at 25°C. Four different batches of monodispersed (coefficient of variation CV $\leq$ 5%) fluorescently labeled colloids were employed throughout the study: 660 nm, 1400 nm, 2200

nm polymethylmethacrylate (PMMA) particles with a grafted layer of polyhydroxystearic acid (PHSA), labeled with Nile red fluorescent dye (technical grade Sigma Aldrich), and 660 nm silica nanoparticles labeled with fluorescein isothiocyanate (90% Fisher Scientific). The PMMA particles were generated from previously reported synthesis procedures[69], [70], and a modified Stöber process[64], [100], [101] was used to synthesize fluorescent silica particles whose surfaces were subsequently treated with hexamethyldisilazane to render them interfacially active with respect to the fluid phases used in this study. Each particle batch was imaged via Scanning Electron Microscopy (Quanta 3D FEG, Thermo Scientific) to characterize particle size and monodispersity (see Figure S3.1 in Section 3.5.1). In calculating experimental particle volume fractions, the densities of silica and PHSA-grafted PMMA particles were taken to be 2.02 mg/μL[101] and 1.17 mg/μL[69], respectively. The particles' wetting behaviors with respect to the fluid phases were characterized on an optical tensiometer (Attension Theta, Biolin Scientific), by estimating their equilibrium three-phase contact angles via the immersed droplet method[71] (see Figure S3.2 in Section 3.5.1). All four particle batches exhibited contact angles of ~140°-147°, and were experimentally observed, by confocal microscopy, to stabilize aqueous-in-oil droplets (the fluids can be distinguished from one another by selectively dyeing the aqueous phase with rhodamine B (95% Sigma Aldrich) to help determine the type of emulsion formed). To reduce droplet polydispersity, HIPE samples were derived from emulsions that were initially formed at a 30:70 fluid volume ratio between the aqueous and oil phase (thereby reducing droplet collisions during preparation). The oil phase in this initial state was a mixture of dodecane and hexane (98.5% Fisher Scientific). Subsequent evaporation of hexane then concentrated the emulsions into HIPEs. The initial, dilute emulsions were prepared in 1.5 mL centrifuge tubes charged with a recorded mass of solids, to which 0.36 mL aqueous phase and

0.84 mL oil phase were added. An ultrasonic probe (Sonifier 250, Branson Ultrasonics) emulsified the samples, running continuously at 2 W power for ~45 sec, followed by vortex mixing (Vortex Genie 2, Science Industries) for 5 min at the highest speed setting. Samples were then decanted into custom-made sample holders (50-mm tall polycarbonate tubes with inner diameter ID = 25 mm each placed upright, but not attached, in a polystyrene petri dish whose surface was coated with nail polish to prevent sample slip during oscillatory rheometry). To assure complete transfer of the samples into the sample holders, the decanted centrifuge tubes were washed out with 0.50 mL hexane. Once in the holders, samples were aged for 5 hr before the polycarbonate tube was carefully raised away and the resulting disk-shaped specimens were immediately used for rheology experiments (A characteristic sample is shown in Figure S3.3 of Section 3.5.1). Sample preparation was staggered such that each sample was tested at 5 hr of aging. As the evaporation rate for hexane is far greater than dodecane or the encapsulated aqueous phase (see Figure S3.4 in Section 3.5.1), hexane is argued to be selectively and entirely removed from HIPE samples after 5 hr. As such, the initial amounts of dodecane and hexane, along with particle loading, can be varied to achieve solid-stabilized emulsions with different compositions. With 5 hr of aging, we observe that samples reach a quasi-steady state in regards to their microstructure (see Figure S3.5 in Section 3.5.1). It is important to re-emphasize that hexane is only a provisional solvent used for initial sample preparation, and is not expected to be present in the final specimens that are examined. Gas Chromatography was utilized to analyze aliquots of the continuous oil phase present immediately after sample formation and after 5 hours of aging. These tests verify the evaporation of hexane, as well as confirm that a negligible amount of dimethyl sulfoxide is solubilized within the continuous phase (see Section 3.5.2 for more details on Gas Chromatography experiments). In addition, monitoring the mass of various

mixtures of dodecane and hexane over 5 hours of aging further corroborated that hexane is nearly completely removed from the continuous phase within this timeframe (see Figure S3.4 in Section 3.5.1 for mass loss experiments).

3.2.2 Confocal Microscopy

Solid-stabilized HIPE samples were visualized on a custom microscopy stage coupled to a confocal scanner (Vt-eye, Visitech International), using a 20X NA = 0.4 objective (Carl Zeiss AG) to image the overall sample microstructure, and a 100X NA = 1.4 oil-immersion objective (Carl Zeiss AG) to verify the bilayer of particles separating droplets. To enable imaging with the oil-immersion objective, the sample preparation protocol outlined earlier was slightly modified to have samples aged on 40 x 50 mm optical glass coverslips. Importing confocal micrographs to ImageJ software, the average droplet diameter was evaluated with the "straight line" tool and by manually recording the diameters of ~20 droplets within each sample. When measuring droplet diameters, only the inner dark region of each droplet was considered. Confocal imaging was typically done at a distance ~25 μm away from the bottom coverslip to avoid significant wall effects while ensuring sufficient spatial resolution to discern droplet diameters.

3.2.3 Rheometry

A stress-controlled rheometer (AR-G2, TA Instruments) was used to characterize the rheology of solid-stabilized HIPEs. Samples, prepared as outlined above, were fastened onto the rheometer stage held at 25°C. A sandblasted parallel-plate geometry (diameter d = 25 mm) was slowly brought into contact with the disk-shaped specimen. Each sample underwent an oscillatory strain sweep spanning $\gamma = 0.01 – 1000\%$ at a constant frequency $f = 1$ Hz, throughout which the storage and loss moduli, G' and G'', were recorded. The zero-shear elastic modulus, G'_0, was calculated as the average value of G' over the range $0.01\% < \gamma < 0.1\%$ within the

oscillatory strain sweep, where a plateau in G′ was observed. Due to the large number of individual specimens (161 distinct compositions) examined within our study, single experiments were performed on the majority of samples. However, the reproducibility of our data was tested by performing three true replicate experiments on HIPEs stabilized with 660 nm PMMA particles, at three different sample compositions (see Figure S3.6 in Section 3.5.1).

3.3 Results and Discussion

3.3.1 Compositional Trajectories and Resulting Microstructural Changes

The experimental parameter space explored in this investigation is outlined in Figure 3.1, where the compositions of all the solid-stabilized HIPE samples examined are marked on a ternary plot and categorized into four different trajectories.

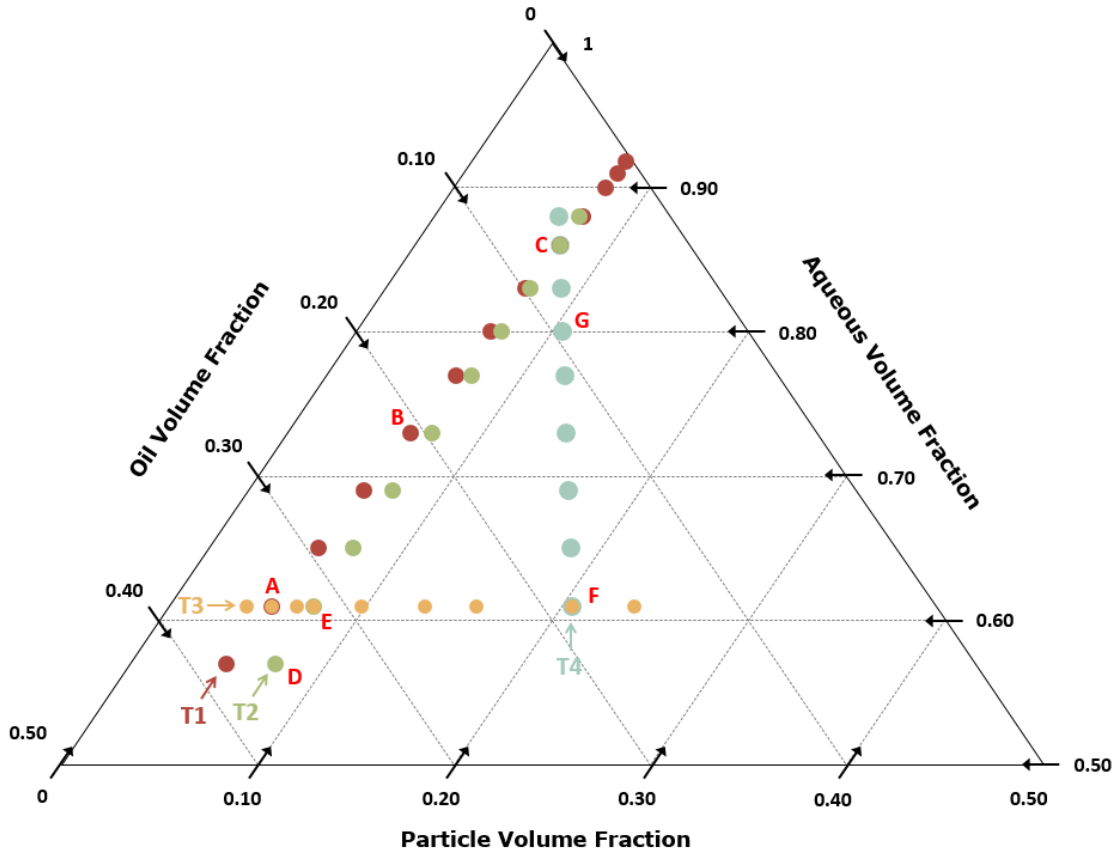

Figure 3.1. Ternary composition plot of the various solid-stabilized HIPE samples examined, which feature aqueous-in-oil droplets stabilized by colloidal particles. The sample trajectories T1, T2, T3 and T4 are color coded as maroon, green, yellow, teal, respectively; as well as denoted by the inserted arrows and labels. This trajectory color coding corresponds with Figures 3.2, 3.4, and 3.6. Samples demarked with red letters are shown in Figure 3.2.

A broad range of compositions is achieved by exploiting the multiphase nature of these emulsions, which feature aqueous-in-oil droplets stabilized by partially hydrophobic particles. The trajectories examined here represent four different ways of tuning these multiphase formulations, in each case holding one of the key compositional parameters constant, while varying the others. The resultant map is discussed further below in the context of the trajectories illustrated in Figure 3.1. To better explain the changes along each trajectory, we will present and discuss them in conjunction with the microstructural information presented in Figure 3.2, in which confocal microscopy images are false-color-coded to match the trajectories in Figure 3.1.

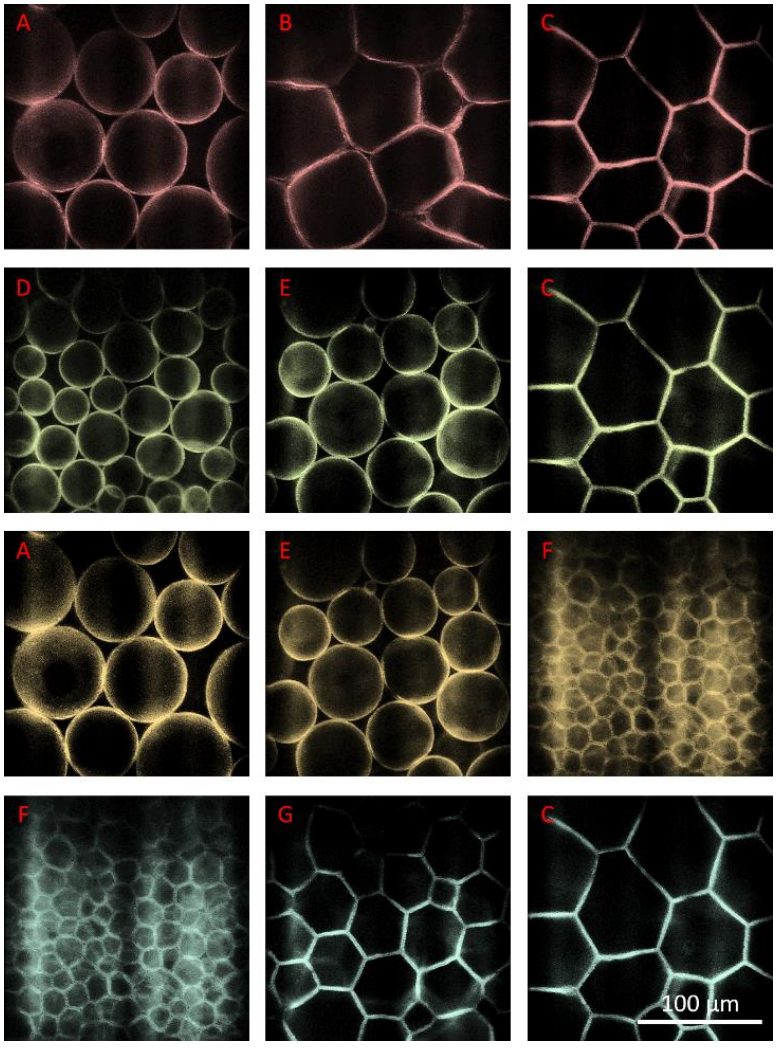

Figure 3.2. Confocal images of emulsion samples stabilized by 1400 nm PMMA particles. The color coding (top to bottom) corresponds with the sample trajectories T1, T2, T3, T4 respectively of Figure 3.1. As do the red letters, to denote the specific sample composition of each emulsion.

The first trajectory, T1, shown by maroon circles in Figure 3.1, features emulsion specimens that become more concentrated (increasing their dispersed phase volume fraction) in the direction shown by the maroon arrow, while maintaining a constant droplet diameter, δ. Therefore, the oil volume fraction, ϕ_O, the aqueous volume fraction, ϕ_A, and particle volume fraction, ϕ_P, all change along T1. This is a typical trajectory analyzed in past studies on both surfactant-stabilized[25] and solid-stabilized HIPEs[30]. It is usually achieved by progressively diluting a highly-concentrated emulsion with the continuous fluid phase. However, our method of sample preparation is based on selective removal of a volatile fluid component of the continuous phase, as explained above. Therefore, T1 samples are formulated as follows. All specimens are prepared with the same initial volumes of particles and aqueous and oil fluid phases, in which the ratio of hexane to dodecane in the oil phase is varied to yield the desired target composition once all the hexane evaporates. Constant droplet size is achieved by holding the volume ratio of particles to aqueous phase constant among the initial samples[72], and has been verified experimentally. For example, see Figures 3.2A, 3.2B, and 3.2C (Row 1 in Figure 3.2), which show representative microstructures along T1 (note these samples are also marked as points A, B, and C in Figure 3.1). As ϕ_A is increased from sample A to C, the droplets remain approximately constant in size but begin to deform into faceted cells, due to crowding. Therefore, the microstructural changes along T1 can be summarized as droplet deformation, likely due to crowding, at constant droplet size. In the next trajectory (T2) samples are formulated at a constant particle volume fraction $\phi_P = 0.074$. The initial oil phase composition, as well as particle volume, is varied among T2 samples to achieve specimens with the target compositions denoted by green circles in Figure 3.1. In the direction marked by the green arrow in Figure 3.1, T2 samples become more concentrated (their ϕ_A increases) at constant $\phi_A = 0.074$.

The most important microstructural consequences of these changes are shown in Figures 3.2D, 3.2E, and 3.2C (Row 2 in Figure 3.2), where the droplet diameter increases with increasing ϕ_A, and the droplets eventually become faceted. Note that composition C in Figure 3.1 is a point of intersection between trajectories T1, T2, and T4, and therefore image 3.2C repeats itself in three different rows in Figure 3.2, which is done on purpose to better illustrate how each trajectory can lead to faceting in these systems. To better assess the connection between the rheology and microstructural transitions in these systems (with discussions of the rheology to follow below), in a third trajectory, T3, the aqueous volume fraction is held near but just below the random close packing limit of hard spheres ($\phi_{RCP} = 0.64$) at $\phi_A = 0.61$, as marked by yellow circles in Figure 3.1. In the direction of the yellow arrow shown, ϕ_P increases while ϕ_O decreases to compensate for the increase in ϕ_P while keeping ϕ_A constant. Representative images for samples in this trajectory are shown in Figures 3.2A, 3.2E, and 3.2F (Row 3 in Figure 3.2), again color-coded to match Figure 3.1. Given that ϕ_A stays below ϕ_{RCP}, in surfactant-based systems such a trajectory is not expected to result in a change in droplet shape (or, as will become relevant later, a significant change in the mixture's rheology). However, as shown in Figure 3.2, this is not the case in solid-stabilized systems: an increase in ϕ_P along this trajectory results in a transition from spherical to faceted droplets, with a concomitant decrease in droplet size. Recall that, along T3, we maintain $\phi_A = 0.61$ by systematically reducing ϕ_O as ϕ_P is increased, effectively replacing the continuous fluid phase with particles along the direction marked by the yellow arrow in Figure 3.1. The observation that this effect results in confinement and deformation of droplets into faceted cells illustrates the importance of particle excluded volume in mediating the microstructure and dynamics of solid-stabilized HIPEs. The significance of particle excluded volume may also be evident in the fourth sample trajectory, T4 (note this trajectory also shares

composition F as a point of intersection with T3). Here the volumetric ratio of the oil phase (dodecane) to particles is held constant at 0.9:1. This particular ratio is estimated geometrically to result in a film between dispersed droplets just thick enough to accommodate a bilayer of spherical particles. Therefore, the samples along T4 are expected to display a foam-like faceted microstructure, with their droplet size increasing in the direction of the teal arrow in Figure 3.1. This is experimentally confirmed in images 2F, 2G, and 2C. Trajectory T4 illustrates that a foam-like morphology can be retained in solid-stabilized emulsions even at a dispersed phase volume fraction below ϕ_{RCP}. For example, the specimen shown in Figure 3.2F is prepared at ϕ_A = 0.61, and yet exhibits highly faceted droplets. This is another indication of the strong impact that particles can have on the microstructure of solid-stabilized HIPEs, and potentially their rheology, which is examined in the next section. Before moving on, it is important to note that the images in Figure 3.2 are all of emulsions stabilized by 1400 nm PMMA particles. The same microstructural trends are observed for samples stabilized by the other particles employed in this study. The main difference is, for a given composition, samples stabilized by larger or smaller particles systematically exhibit larger or smaller droplets, respectively. The overall range of droplet diameters are 14 – 67 μm for 1400 nm PMMA-stabilized samples, 21 – 86 μm for 2200 nm PMMA-stabilized samples, and 7 – 42 μm for emulsions stabilized by 660 nm particles (both silica and PMMA).

3.3.2 Solid-Stabilized Emulsion Rheology

Figure 3.3 shows the results of oscillatory strain sweeps conducted on three different HIPEs stabilized with 660 nm silica, within trajectory T3.

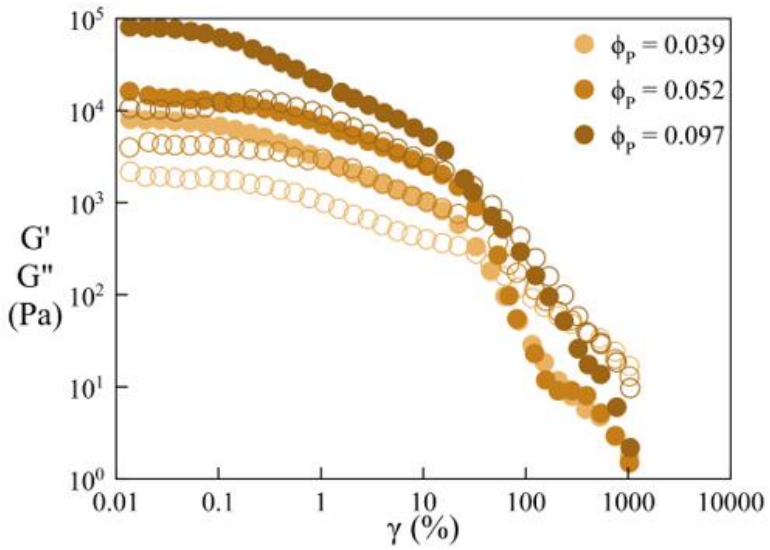

Figure 3.3. Oscillatory strain sweeps, conducted at a constant frequency f = 1 Hz, on emulsion samples within trajectory T3. These three samples are stabilized with 660 nm silica at a constant ϕ_A= 0.61 and the denoted ϕ_P. G' and G'' are represented by solid and hollow markers, respectively.

The general behavior seen in Figure 3.3 is representative of all emulsion samples tested. Specifically, samples exhibit signatures of gel-like rheology with a $G' > G''$ plateau at small strains, and a drop in the elastic modulus and crossover to $G'' > G'$ at large strains. From such measurements, for each sample we extract the zero-shear elastic modulus, G_0', estimated as the average G' value at the lowest strain amplitudes where G' approximately plateaus ($0.01\% < \gamma < 0.1\%$). We focus on the dependence of G_0' on sample composition, tested along the trajectories outlined in Figure 1. Before we discuss the complete set of results, it is worth noting that an increase in the particle loading (ϕ_P) at constant volume fraction of the dispersed phase (ϕ_A) results in an increase in the sample's strength (the plateau in G' at low γ), as shown in Figure 3.3. This observation readily hints at how particle loading can be used as an important control knob to tune the rheology of solid-stabilized HIPEs. While an increase in the elastic modulus with solids loading is not surprising for a particulate system, its exact mechanism, functional form, and range of tunability are not obvious in this case, especially when we view it in the context of

emulsion rheology[28] and recognize that the dispersed (aqueous) phase volume fraction was held constant in Figure 3.3. We will discuss this issue in more detail below.

To put our results in the conventional context of emulsion rheology, and particularly demonstrate the additional level of tunability afforded by the particles, in Figure 3.4 we plot G_0' as a function of ϕ_A for four different particle batches collectively representing three different sizes and two different surface chemistries, along the compositional trajectories shown in Figure 3.1. Note that the different symbols represent the particle batches used, with color coding that corresponds to the trajectories in Figure 3.1. The large number of samples presented in Figure 3.4 precluded us from performing replica measurements for each. However, we performed three true replicate measurements for T1 samples stabilized with 660 nm PMMA, at ϕ_A = 0.61, 0.77 and 0.86, which demonstrated great reproducibility in the value of G_0' extracted from oscillatory strain sweep experiments (see Figure S3.6 in Section 3.5.1).

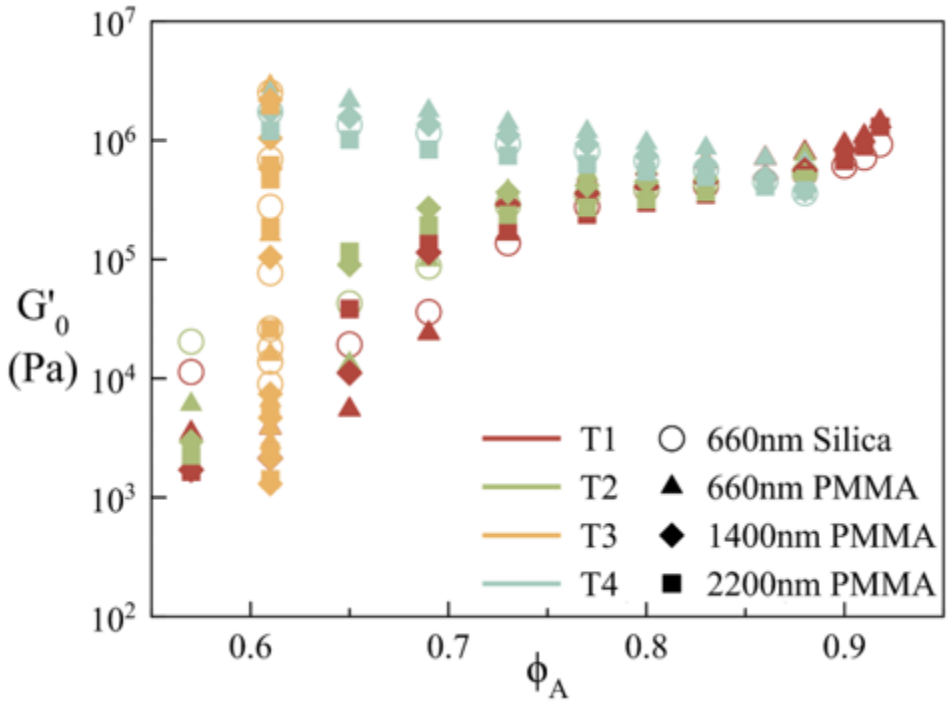

Figure 3.4. Zero shear elastic modulus, G_0', plotted against the dispersed liquid (aqueous phase) volume fraction, ϕ_A, for solid-stabilized HIPEs. The particles are denoted by the different symbol shapes. Samples within each trajectory are color-coded in correspondence with Figure 3.1.

First, similar to surfactant-based and a limited number of solid-stabilized systems reported, a dramatic (more than three orders of magnitude in this case) increase in the elastic modulus is observed over a moderate range of $0.57 < \phi_A < 0.91$. In surfactant-based systems, most of the transition to solid-like rheology occurs over a narrow window near the random close packing limit of hard spheres ($\phi_{RCP} = 0.64$), whereas here, such a sharp and well defined transition cannot be discerned from the data presented. Of the trajectories tested, the data from T1 and T2 show some similarity to what has been previously reported, with a pronounced rise in G_0' as ϕ_{RCP} is increased. However, the data for T1 and T2 from different particle batches do not overlap, and the transition from low to high G_0' is not as sharp, extending to $\phi_A \approx 0.75$. Further, and more importantly, trajectories T3 and T4 exhibit behaviors that initially appear at odds with surfactant-based systems, and each show in a different way how significant the role of particles is in the rheology of solid-stabilized emulsions. Specifically, T3 illustrates that by varying the solids loading, G_0' can be tuned over more than three orders of magnitude at a constant dispersed fluid volume fraction ($\phi_A = 0.61$) which, notably, is below ϕ_{RCP}. Separately, T4 shows how G_0' can be even made to decrease with increasing ϕ_A, which is the opposite of what happens in surfactant-based emulsions, again by tuning the volume fraction of particles. The final notable feature in Figure 3.4 is a second rise in G_0' at the highest values of ϕ_A. Next we will examine these observations in more detail, and provide an initial framework for rationalizing the rheology of solid-stabilized emulsions in light of the basic interfacial and colloidal interactions at play.

3.3.3 Effect of Particle Excluded Volume

To better convey the ideas that follow, we will discuss them in the context of both the microstructural (Figure 3.2) and rheological (Figure 3.4) results presented above. Let us focus on T3 again. Along this trajectory, for a given total sample volume, oil is being systematically

replaced by particles while the volume of the aqueous phase is held constant. As shown in Figures 3.2 and 3.4, this rise in particle volume fraction results in a continuous reduction in droplet size, eventually leading to faceting, concomitant with an increase by more than three orders of magnitude in G_0'. Since ϕ_A is being held constant, it is clear that the colloidal particles play a critical role in the transition from liquid-like to solid-like behavior in these systems. A similar conclusion can be drawn from the behavior of samples along T4. From Figure 3.4, G_0' is seen to increase along T4 with decreasing ϕ_A, notably even as ϕ_A spans below the random close packing limit of hard spheres. A foam-like microstructure with highly faceted droplets is also maintained along this trajectory, even below ϕ_{RCP}, as shown in Figure 3.2. To rationalize these trends, here we propose the simplest correction, which is to report the data in terms of an effective dispersed phase volume fraction that accounts for particle excluded volume interactions. This is done simply by incorporating the monolayer of particles, present at the droplet interfaces, into a corrected droplet diameter, δ_{EFF}, as shown in Figure 3.5, to convert ϕ_A into an effective dispersed volume fraction, ϕ_{EFF}.

$$\phi_{EFF} = \phi_A\left(\left(1+\frac{2x}{\delta}\right)^3\right) \tag{3.1}$$

In Equation 3.1, δ is the diameter of the liquid droplets, measured as described in Section 3.2.2, and the parameter x accounts for how far each particle protrudes from the droplet interface into the continuous phase due to its wetting characteristics. The dependence of x on particle diameter, δ_P, and the equilibrium three-phase contact angle, θ, is as follows:

$$x = \frac{\delta_P}{2}\left(1+\sin\left(\theta-\frac{\pi}{2}\right)\right) \tag{3.2}$$

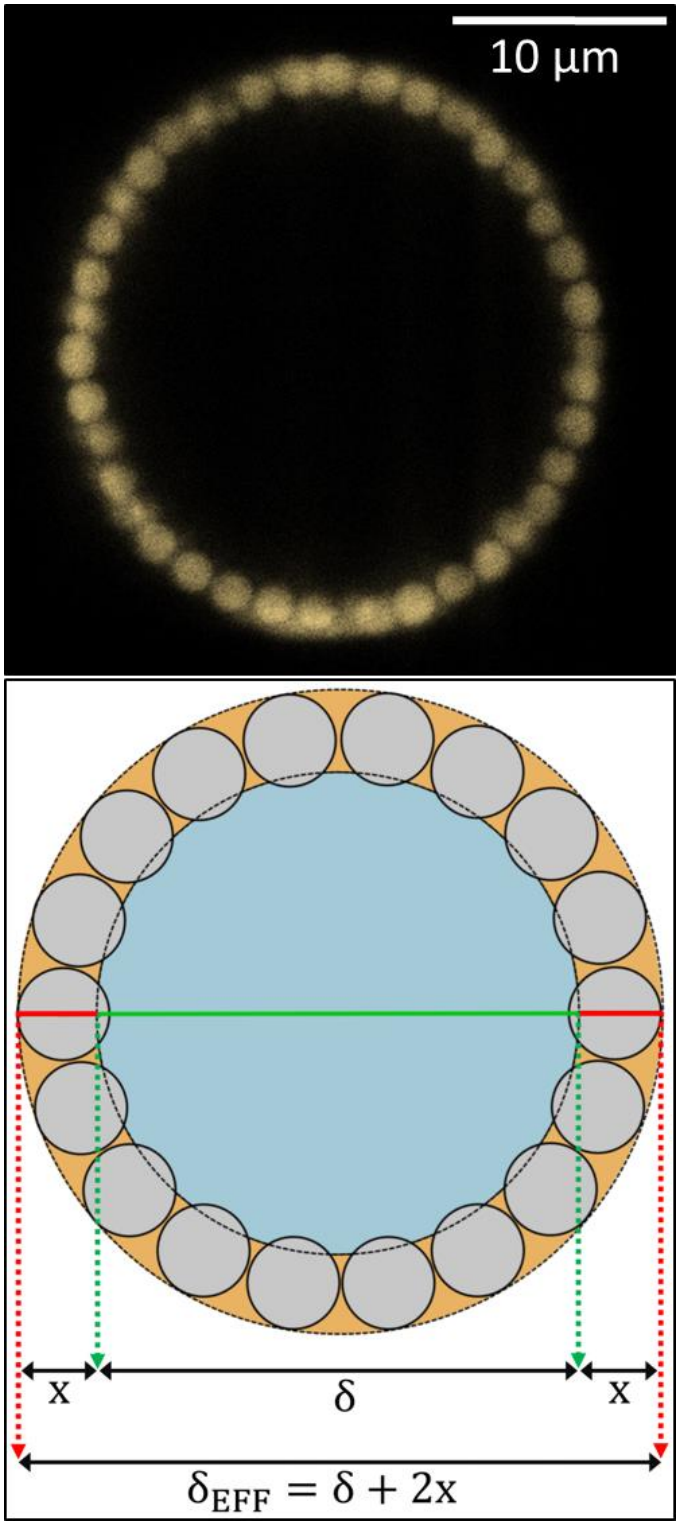

Figure 3.5. An experimental image of a droplet stabilized by 2200 nm PHSA-PMMA particles (top). Illustration of how the adsorbed particle monolayer impacts the effective diameter, δ_{EFF} (bottom). The liquid droplet diameter is δ, and x measures how far the particles protrude from the droplet interface.

The derivation of Equations 3.1 and 3.2 are outlined in Section 3.5.3. Reporting the data in terms of ϕ_{EFF} will account for the contribution of particle excluded volume to inter-droplet interactions. We also choose the parameter σ/R as the relevant scale to normalize G_0' with, where σ is the interfacial tension between the two fluid phases and R is the droplet radius ($R = \delta/2$). This parameter, also equal to the Laplace pressure of the dispersed liquid droplets, is a measure of the interfacial energy per unit volume of the mixture[39], [40], [56], [102]. Previous research on concentrated surfactant-stabilized emulsions has shown a collapse of experimental data with different droplet sizes onto a master curve when G_0' is scaled with σ/R and plotted against the dispersed phase volume fraction, ϕ_D[56]. Figure 3.6 shows the scaled zero-shear elasticity of all solid-stabilized emulsions tested as a function of the effective dispersed volume fraction (same data as Figure 3.4 but scaled as explained above).

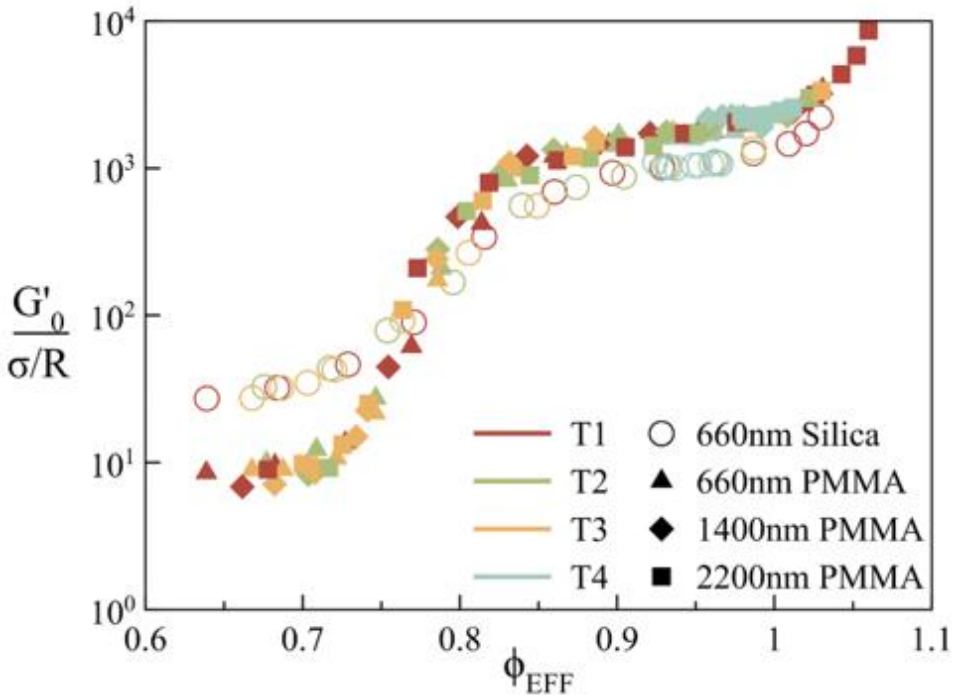

Figure 3.6. Zero-shear elastic modulus, G_0', in solid-stabilized HIPEs, scaled by Laplace pressure of the dispersed liquid droplets, σ/R, plotted against the effective dispersed volume fraction, ϕ_{EFF}. The particles are denoted by the different symbol shapes. Samples within each trajectory are color-coded in correspondence with Figure 3.1. Note, ϕ_{EFF} values greater than 1 are an artifact of the definition of ϕ_{EFF} that results in a collapse of data (see discussion in text).

When presented in this manner, the data from all trajectories appear to fall onto two distinct master curves. Similar to surfactant-stabilized systems, both curves have a region of low G_0' that rapidly grows past a critical effective dispersed volume fraction, here at $\phi_{EFF} \approx 0.80$. Direct comparison to the master curve reported for surfactant-stabilized emulsions[39], [56] (see Figure S3.7 in Section 3.5.1), shows this transition occurs closer to $\phi_{EFF} \approx 0.64$ in those systems, which also exhibit lower values of G_0' than solid-stabilized HIPEs. The observed shift in ϕ_{EFF} occurs throughout the range of compositions examined, and stems from the way that ϕ_{EFF} is defined in our study: the effective volume of a dispersed droplet is based on an imaginary sphere whose diameter fully engulfs the particles residing at the interface (sphere of diameter δ_{EFF}, shown by the outer dashed circle in Figure 3.5). With this definition, a finite amount of the continuous fluid phase, located between adjacent particles along the interface, is included in the droplet's calculated effective volume. Our rationale behind this treatment is that the onset of dynamic arrest due to crowding is likely set by the overlap concentration of spheres of diameter δ_{EFF}. Note that this definition also results in calculated values of ϕ_{EFF} that can be larger than 1 (see Figure 3.6). We will return to this issue later in the paper. Nevertheless, the collapse of data onto master curves based on this definition of ϕ_{EFF} corroborates its relevance for describing the transition to solid-like rheology in these systems. Importantly, it also demonstrates that to properly account for the excluded volume of particles, their three-phase contact angle must be known. Recall that in trajectory T3, samples are all prepared at $\phi_A = 0.61$, but show signs of becoming more concentrated with particle loading, with droplets transitioning from spherical to highly faceted cells (Figure 3.2) and a rise by three orders of magnitude in G_0' (Figure 3.4). Once ϕ_{EFF} is considered, the cause of these transitions becomes apparent as T3 samples are seen to span a range of effective dispersed volume fractions in Figure 3.6. Our simple correction also

rationalizes the data for T4, where faceted droplets were retained even when ϕ_A dropped below ϕ_{RCP} (Row 4 in Figure 3.2). From Figure 3.6, all samples in T4 are seen to fall above the critical dispersed volume fraction, where the expected microstructure is a crowded system of faceted droplets. Simply put, along T4, the decrease in ϕ_A is compensated for by a rise in ϕ_P, which allows the composite dispersed droplets to remain highly concentrated. Therefore, the rich rheological behavior reported in Figure 3.4 can be generally understood by applying simple corrections to the data to properly account for the particle excluded volume and the relevant interfacial energy scale in the system. In previous research done on particle-stabilized emulsion rheology, the effect of particle excluded volume is often neglected[103], [104], [38]. Some of these studies are limited to either dilute emulsions (dispersed fluid volume fraction < 50%) or small (~10 nm) stabilizing particles, where the impact of particle excluded volume is not as prevalent. Our sample formulations extend to a region where these effects are fully accessible, enabling their quantification via systematic experiments. The master curves obtained in Figure 3.6 then allow us to examine the more intricate aspects of how various colloidal interactions may affect the rheology of solid-stabilized HIPEs. We will discuss this issue next, focusing on the differences between the two curves. Before closing the discussion of the particle excluded volume, it is worth noting that an alternative and more intuitive definition of ϕ_{EFF} in which the volume fractions of the particles and the dispersed liquid phase are added, $\phi_{EFF} = \phi_P + \phi_A$, does not result in a collapse of data onto a master curve (see Figure S3.8 in Section 3.5.1). This important observation supports our hypothesis that, to correctly account for dynamic arrest and transition to solid-like rheology in solid-stabilized emulsions, an effective diameter that fully engulfs the interfacially adsorbed particles and accounts for their three-phase contact angle, δ_{EFF}, must be considered (see Figure 3.5).

3.3.4 Colloidal Interactions Imparted by Particle-Laden Interfaces

Our use of two different surface chemistries and three different sizes for the particles in this study allows us to investigate the possible role of these two parameters (surface chemistry and size) in the rheology of solid-stabilized emulsions. Let us point out two important features in the master curves of Figure 3.6. First, the most pronounced difference between the two master curves is in their G_0' plateau values at low ϕ_{EFF}. Given that this plateau occurs below the critical ϕ_{EFF}, the mixture's elasticity in this region cannot be attributed to bulk crowding. Our microstructural data confirms this, as undeformed spherical droplets are observed over this range of ϕ_{EFF}. We postulate that the disparity between the two curves arises from attractive colloidal interactions through the oil phase. To test this hypothesis, we performed oscillatory strain sweep measurements on suspensions of silica and PMMA particles (separately) at a particle volume fraction $\phi_P = 0.4$ in pure dodecane (see Figure S3.9 in Section 3.5.1). Both systems exhibited weak gel-like behavior, which is indicative of attractive interparticle interactions through the continuous phase of our HIPEs (dodecane). However, the interactions are far stronger for silica particles ($G_0' \sim 525$ Pa for silica, and $G_0' \sim 25$ Pa for PMMA). Therefore, the elastic moduli at low ϕ_{EFF} in Figure 3.6 are likely dominated by such interactions through the continuous phase, and the higher plateau value seen for the silica samples is probably due to the attractive forces being stronger in that system. These interactions are expected to be at play throughout the entire range of ϕ_{EFF}, and are not captured by the Laplace pressure scaling implemented in Figure 3.6, which is based on the interfacial tension of the particle-free fluid interface, σ. Previous researchers, comparing between solid-stabilized and surfactant-stabilized emulsions, have proposed that an effective interfacial elasticity, ε, is a better measure of the interfacial energy of a particle-laden interface[30], with factors such as hydrogen bonding[105] or other lateral interparticle

interactions potentially contributing to this parameter. This suggests that G_0' should be scaled by ε/R, instead of σ/R, as the salient interfacial energy scale in solid-stabilized emulsions. From Figure 3.6, the greater elastic moduli observed for PMMA samples at higher ϕ_{EFF} suggest that ε dominates emulsion elasticity rather than the attractive interparticle interactions through the continuous phase, and that the use of PMMA particles in our system results in a more rigid droplet interface than that of a silica-stabilized system. However, experimental evaluation of ε for fluid interfaces laden with large particles is nontrivial. Further, even with knowledge of this parameter, a full collapse of our data between different particle chemistries is not expected, since this parameter too fails to fully capture the attractive colloidal interactions between different droplets through the continuous phase. Still, the rheology data as presented in Figure 3.6 allow us to discern the different contributions solid particles make to the rheology of solid-stabilized HIPEs.

The second notable feature in Figure 3.6 is a final rise in the scaled elastic modulus at the high-end of the ϕ_{EFF} range, which is a unique feature not observed in surfactant-stabilized systems. The rise in the scaled elastic modulus is observed for both HIPEs stabilized with PMMA and silica particles, and occurs as the sample composition goes past a 0.9:1 volumetric ratio of oil to particles. Recall that the ratio 0.9:1 should result in a thin film between faceted droplets just sufficient to accommodate a bilayer of particles, as seen experimentally in the top row of Figure 3.7, and illustrated in the second row. With the definition of ϕ_{EFF} shown in Equation 3.1, the second row in Figure 3.7 corresponds to $\phi_{EFF} \sim 1$, and any further reduction in V_O will correspond to $\phi_{EFF} > 1$. Based on this realization, we propose the following explanation for the late rise in G_0'. As the dispersed volume fraction is increased, the liquid film continues to thin, resulting in a curved fluid interface between particle neighbors along the droplet interface,

which is schematically shown in the third row of Figure 3.7. This in turn gives rise to strong capillary lateral forces between the particles, due to the curved interface between them. Such capillary interactions have been shown to result in extremely strong networks in both granular and colloidal systems[106]–[110]. However, to our knowledge, they have not been previously shown in solid-stabilized HIPEs. At even higher ϕ_{EFF} and oil volume fractions insufficient to sustain a continuous sample-spanning film between the droplets, a possible transition may occur from a highly faceted solid-stabilized HIPE to a pendular gel[109]–[112] with an ordered network of particles held together through interstitial liquid bridges (however, this could not be confirmed in our system as we do not have the means to image the oil film with sufficient spatial resolution). A three-dimensional geometrical model incorporating surface energetics would be required to evaluate the complex capillary forces present in these cases. Such an effort is beyond the scope of this study, but points to a possible future research direction in this area. From our findings we are able to illustrate the impact of particle-laden interfaces on emulsion rheology, and highlight the different mechanisms through which they can influence the elasticity of solid-stabilized HIPEs.

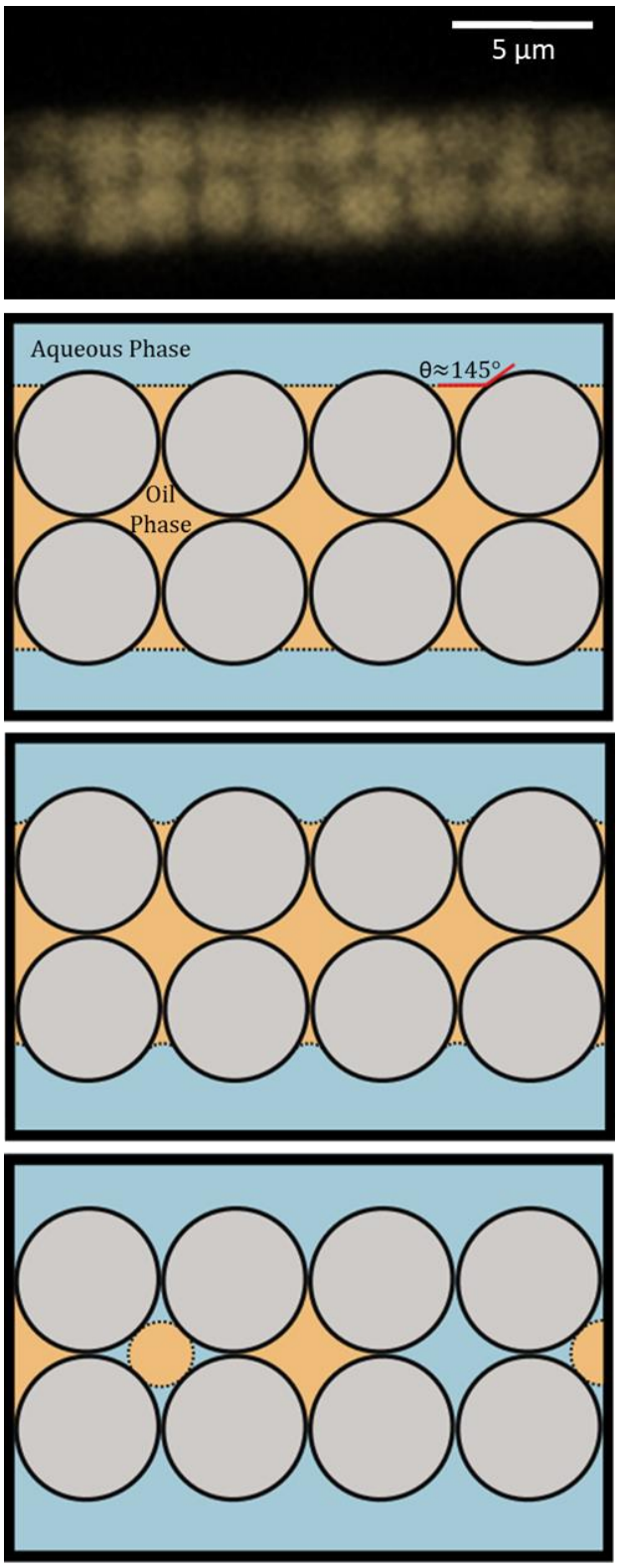

Figure 3.7. A confocal image of a liquid film stabilized by a bilayer of 1400 nm PMMA particles (top). The illustration in rows two to four, show the complex capillary interactions induced in the thin films between highly faceted droplets of solid-stabilized HIPEs. Moving from row two to row four, the volume of the continuous oil phase decreases, higher ϕ_{EFF}.

3.4 Summary

Our results provide a basis for understanding how the solids loading can be used to tune the rheology of concentrated solid-stabilized emulsions over a wide range. Analyzing the zero-shear elastic modulus and microstructure of emulsions formulated over a broad spectrum of compositions along four different trajectories in their ternary state diagram, we report three independent mechanisms, unique to solid-stabilized emulsions and absent in their surfactant-based counterparts[39], that play a significant role in their rheological behavior. First, excluded volume interactions between the solid particles alter the volume fraction of the dispersed phase and enable a transition to dynamic arrest at lower dispersed liquid contents. To properly account for these interactions, the particle position at the interface, characterized by their three-phase contact angle, must be known. We provide evidence for this mechanism with our microstructural images, and by rescaling the normalized zero-shear elastic modulus of our samples with an effective dispersed phase volume fraction, which collapses several compositional trajectories onto master curves based on particle chemistry. The significant impact of particle excluded volume that we demonstrate has been overlooked by earlier investigations on similarly concentrated solid-stabilized emulsions[30], [96], [113]. Second, attractive colloidal interactions through the continuous phase between particles residing at the interfaces of different droplets give rise to a finite elastic modulus even at effective volume fractions below the transition to crowding and full dynamic arrest. Our data suggests that the particle surface chemistry may be used as a means to tune the magnitude of these interactions, and the resulting mixture elasticity. Third, attractive lateral capillary interactions between particles residing on the same fluid interface lead to a second growth in the zero-shear elastic modulus at very high dispersed-to-continuous-phase volumetric ratios. This behavior has not been reported previously, for either

surfactant-stabilized[39] or solid-stabilized systems[30], [96], and is here hypothesized to be a result of capillary forces induced by the thinning of the continuous fluid film between faceted droplets. Lateral attractions between particles on the same interface have been proposed by past researchers[30], [96] to explain the greater rigidity of solid-stabilized emulsions, relative to surfactant-stabilized emulsions. However, further investigation of these interactions, especially their intricate nature in thin fluid films between particle-stabilized interfaces, is warranted to better understand their role in mediating the rheological behavior of solid-stabilized high internal phase emulsions.

3.5 Supporting Information

3.5.1 Supplementary Figures

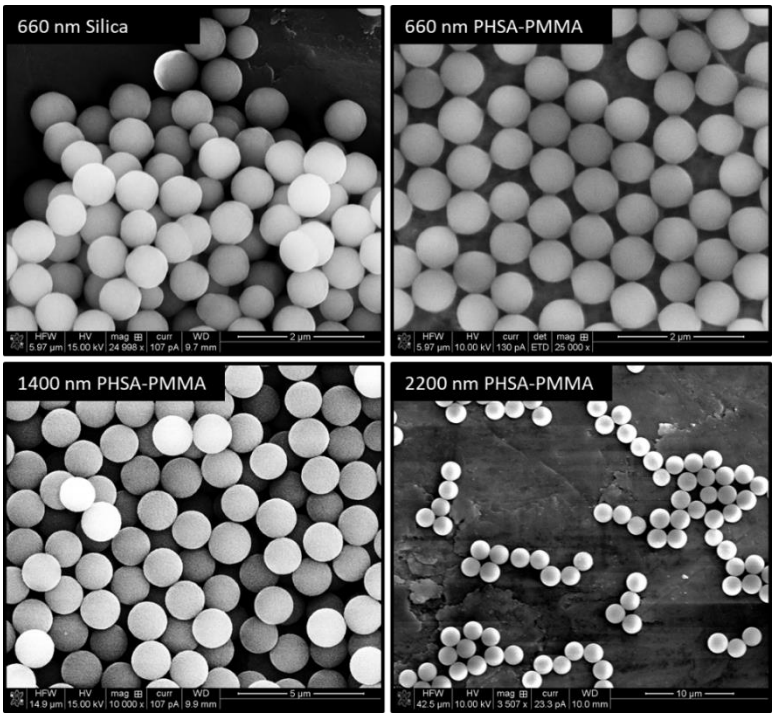

Figure S3.1. Scanning electron microscopy images of each particle batch utilized in the study. The PHSA-PMMA particles were drop casted out of dodecane and silica particles were drop casted out of

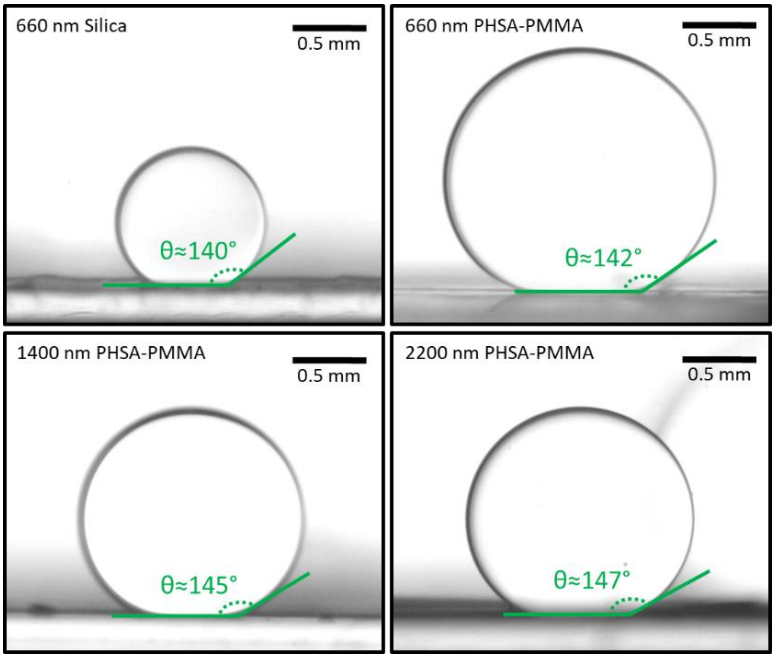

Figure S3.2. The average static contact angle measured by the immersed droplet method for each batch of particles used in the study. In this method an aqueous droplet sits on a microscopic slide, covered with particles by drop casting, within the organic fluid phase.

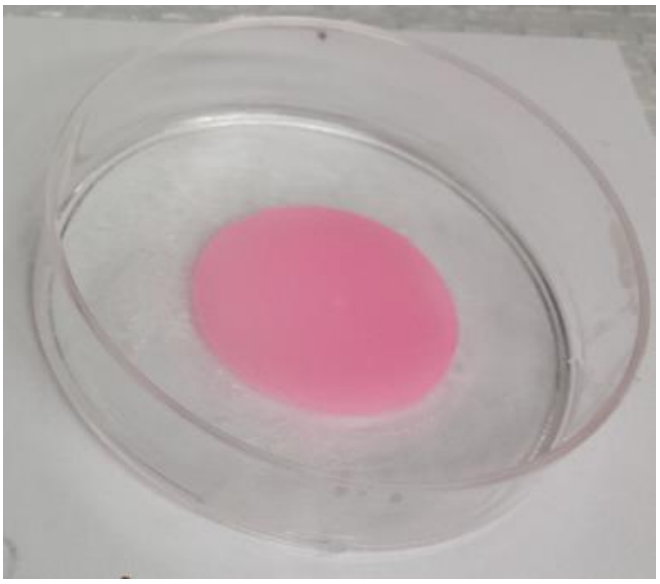

Figure S3.3. A characteristic HIPE sample that has been aged for 5 hours to allow the evaporation of hexane, and the cylindrical tube it was initially surrounded by has been removed. The disk-shaped sample has a 25 mm diameter and ~1 mm height.

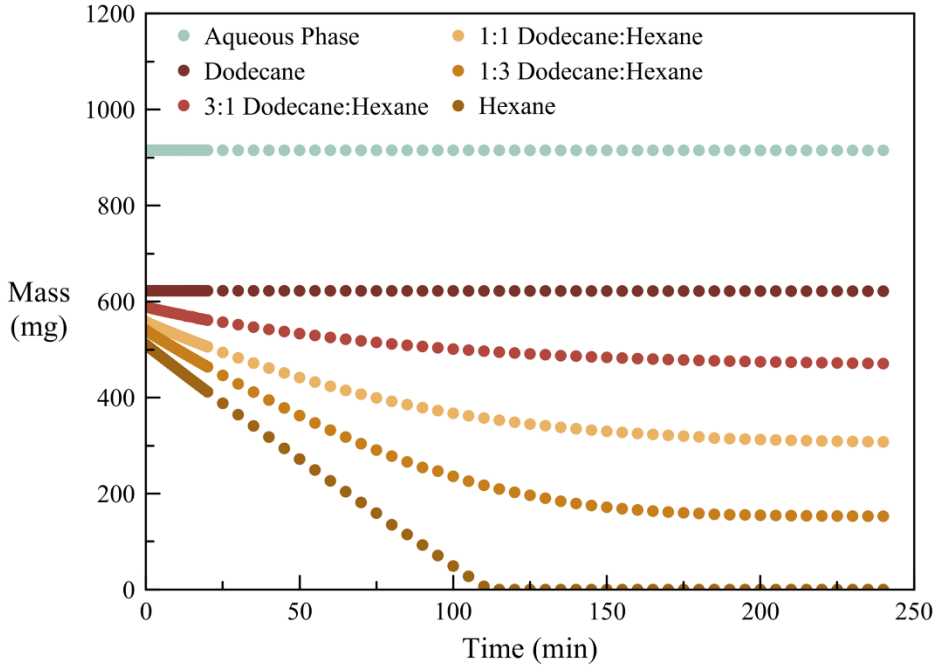

Figure S3.4. The masses of various fluid mixtures relevant to our study, tracked as they evaporate from a 25 mm cross-sectional area glass beaker, at room temperature.

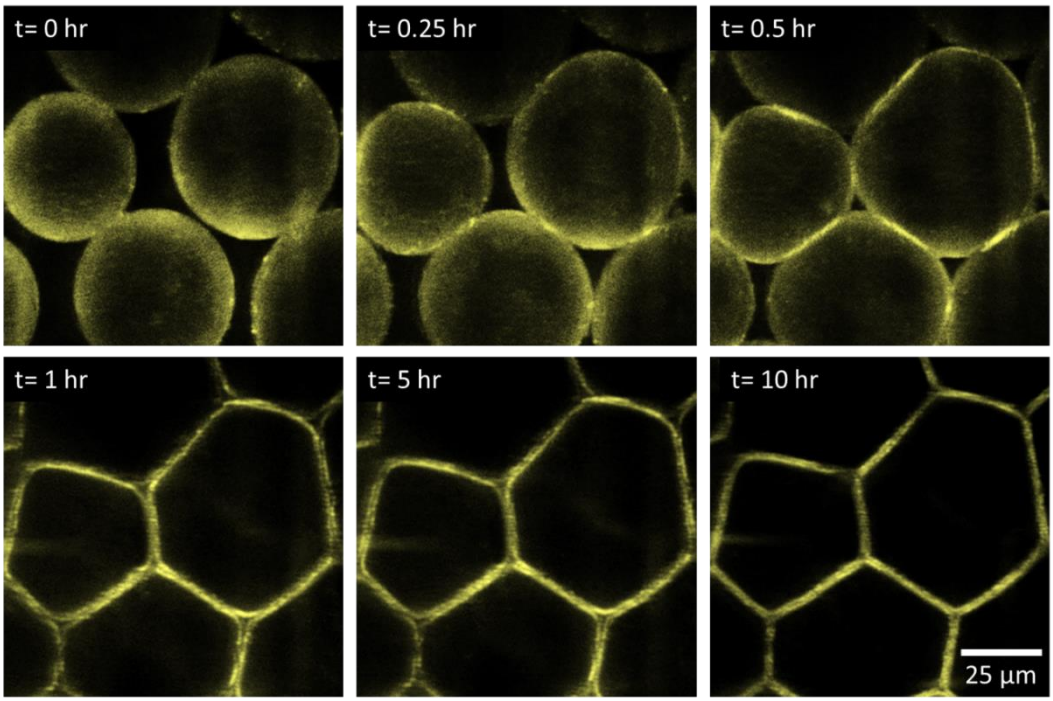

Figure S3.5. The observed microstructure of a trajectory T2 HIPE sample, ϕ_A = 0.77, over a ten-hour aging period. Note this sample was not used for rheological characteristic, but to illustrate the quasi-steady state microstructure our samples exhibit by the five-hour mark.

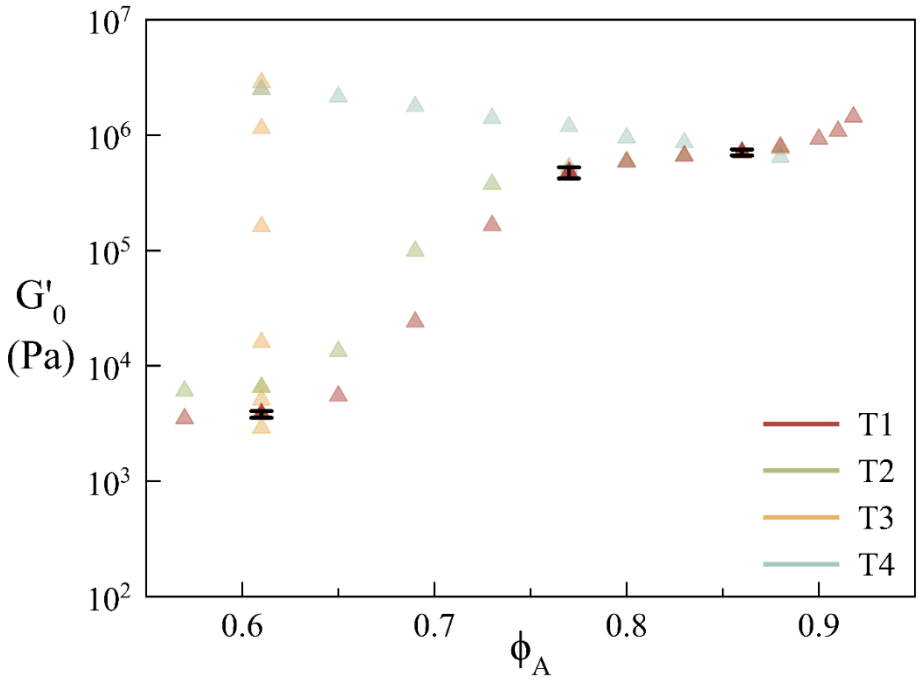

Figure S3.6. G_0' for emulsion samples stabilized by 660 nm PMMA particles, taken from Figure 3.4. To illustrate the reproducibility of our rheology measurements, we have conducted three true replicate measurements on T1 samples formulated with ϕ_A = 0.61, 0.77, 0.86. The error bars at these points illustrate the standard deviation of the three measurements conducted.

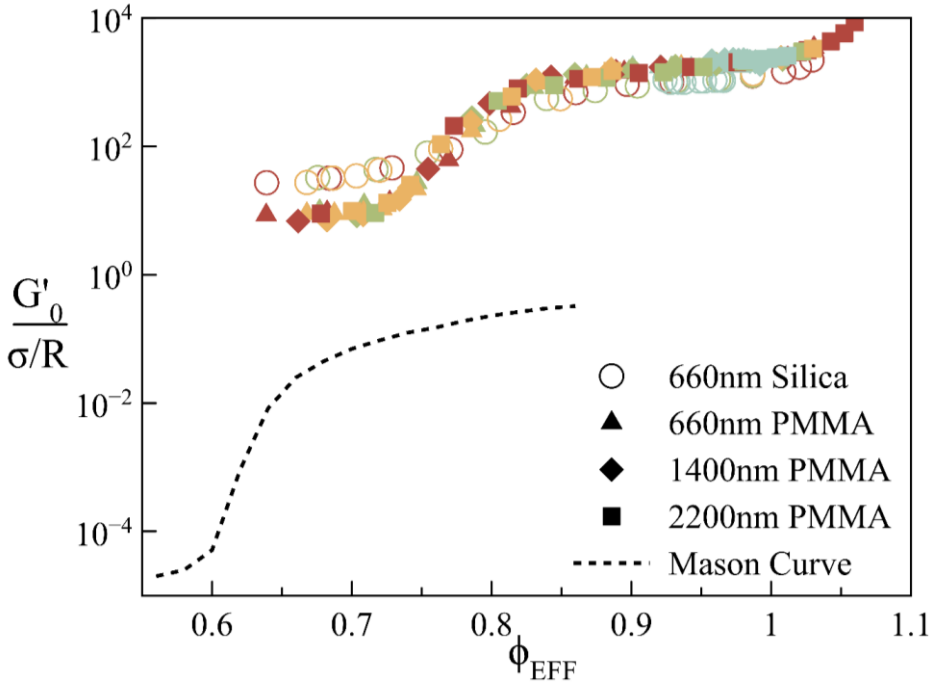

Figure S3.7. Data from Figure 3.6 juxtaposed with the master curve reported for surfactant-stabilized emulsions by Mason et al[56]. Discussion of the noted differences between the data for solid-stabilized and surfactant-surfactant emulsions is found in Section 3.3.3.

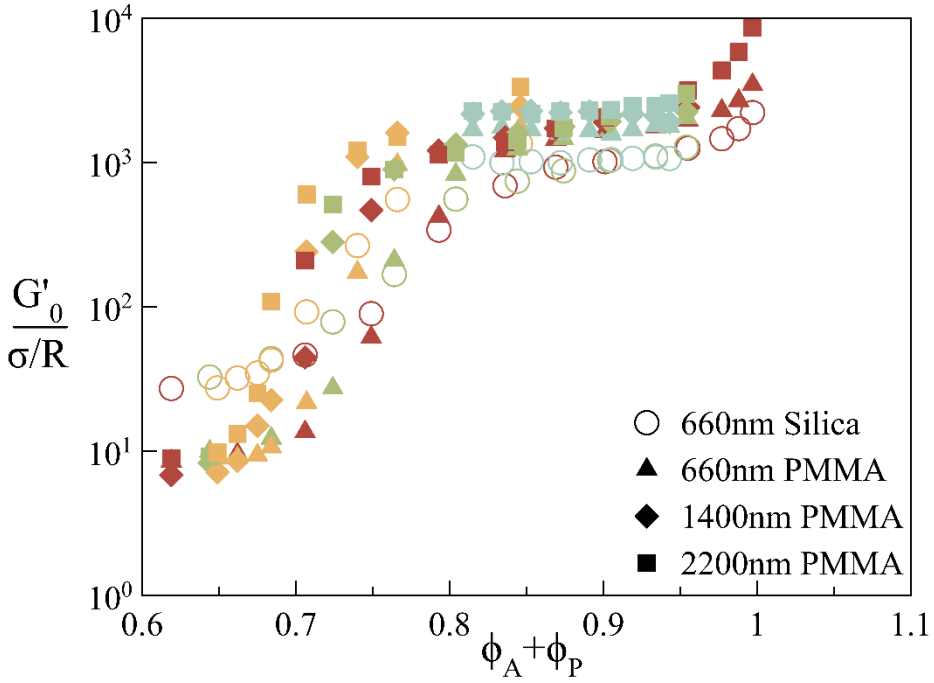

Figure S3.8. Data from Figure 3.6, replotted against an effective volume fraction where the dispersed fluid volume fraction, ϕ_A, is summed with the particle volume fraction, ϕ_P.

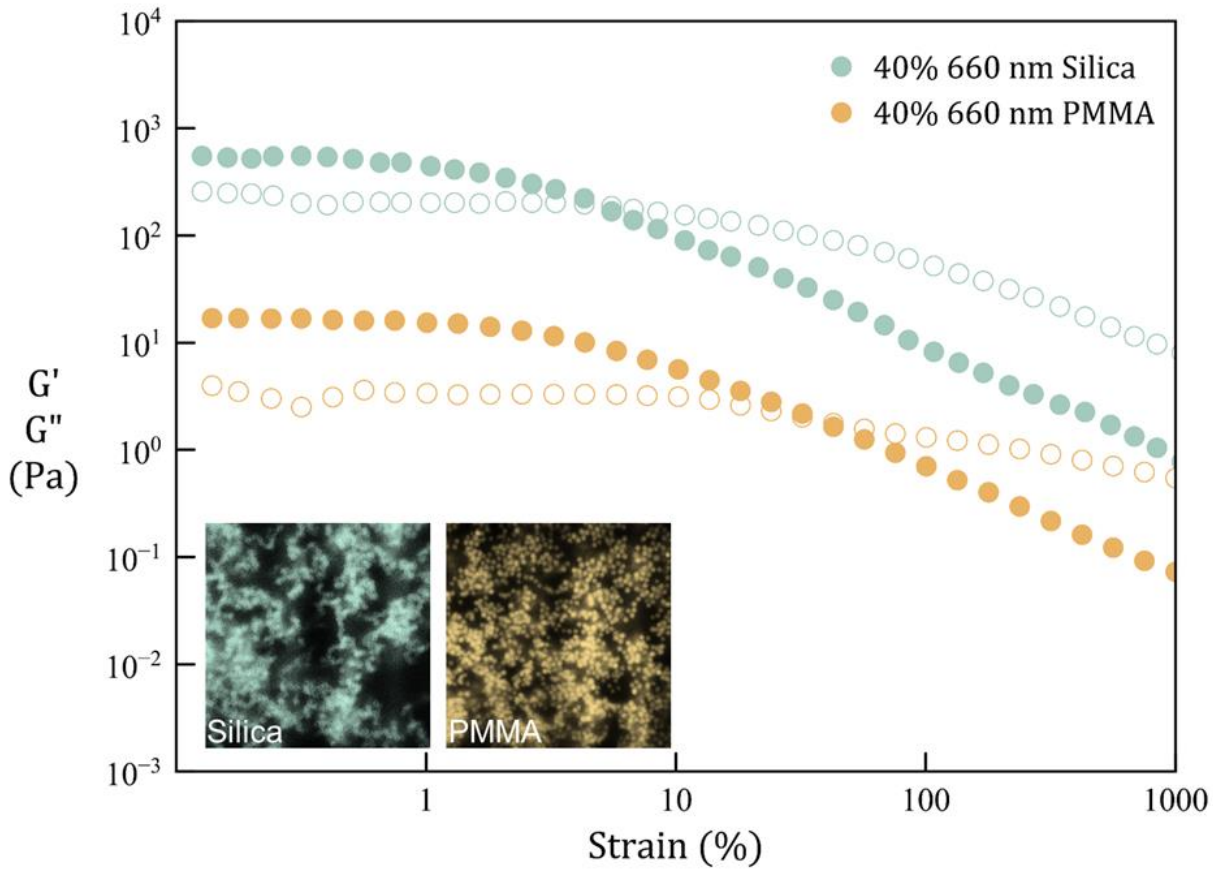

Figure S3.9. Oscillatory strain sweeps, conducted at a constant frequency f = 1 Hz, on particles dispersed in dodecane, at 40% by volume. The storage modulus, G′, and loss modulus, G″, are represented by solid and hollow markers, respectively. The inserted confocal images (30 x 30 μm) show 40% by volume dispersions of either 660 nm PMMA or 660 nm silica particles in dodecane.

3.5.2 Gas Chromatography Experiments

All Gas Chromatography (GC) tests were done with an Agilent 6850 (Agilent Technologies) equipped with a flame ionization detector. The chromatogram operated in a constant pressure mode at 3.66 psi, with inlet and detector temperature held at 250°C and 260°C, respectively. Samples passed over an Agilent DB-WAXetr capillary column (30 m x 0.56 mm x 1 μm) with helium as the carrier gas. Air and hydrogen were supplied to the detector at 350 mL/min and 40 mL/min, respectively. All gases used in GC experiments were purchased from Airgas (Radnor Township, PA). Samples, diluted 20-fold in ethyl acetate, were injected at a volume of 5 μL and a split ratio of 2:1. To yield an appropriate separation of our sample components, the oven was initially held at 50°C for 1 min, then ramped to 120°C at 15°C/min, followed by a 20°C/min ramp to 230°C, and held for 3 min. Elution times were as follows: hexane (1.5 min), ethyl acetate (2.8 min), dodecane (5.0-7.0 min), dimethyl sulfoxide (9.5 min).

In Figure S3.4, the evaporation of dodecane/hexane mixtures, tracked by mass, indicate hexane is removed within the 5 hours of sample aging. To confirm the assumption that our samples are practically devoid of hexane, GC experiments, as described above, were performed to investigate the evaporation of a 1:15 dodecane/hexane mixture. This mixture ratio is characteristic of the oil compositions utilized in formulating our solid-stabilized HIPEs. The total fluid volume was the same as was used in experimental sample formulations and evaporation took place in a 10 mL beaker with a similar 25 mm cross-sectional area as our experimental sample holders. Aliquots of 10 μL were sampled from the mixture when it was initially created and after aging for 5 hours. Our GC results give an initial hexane concentration of 622 mg/ μL and a final concentration of 0.03 mg/ μL. Taking the initial mixture volume as the sum of dodecane and hexane, and the final volume approximately that of the initial amount of dodecane,

these results justify the assumption that hexane evaporates completely (>99.99% removal of hexane).

In calculating the composition of our solid-stabilized HIPEs, dimethyl sulfoxide (DMSO) is assumed to be solely present in the aqueous droplets, though it may be partially solubilized in hexane (29 mg/mL) or dodecane (3.8 mg/mL). To examine the amount of DMSO that partitions into the oil phase, a dilute (ϕ_{EFF}=0.45) HIPE sample was prepared. The initial oil phase consisted of 510 μL dodecane and 830 μL hexane. The HIPE sample was prepared as outlined in Section 3.2.1, and set to age for 5 hours. A 10 μL aliquot of the oil phase was taken when the sample was initially set to age and another 10 μL was taken after 5 hours of aging. The concentrations of DMSO and hexane in the two aliquots are summarized in Table S1. It is evident that the final concentration of DMSO in the oil phase is well below its solubility in dodecane, which is likely because the aqueous phase is not pure DMSO. If we assume the remaining oil is mostly dodecane, as indicated by our hexane evaporation tests, we estimate ~0.07wt% DMSO present in the final oil phase (using a density for DMSO of 1.1 mg/mL and 0.75 mg/mL for dodecane). This result coupled with the evaporation date on the aqueous fluid phase, shown in Figure S4, verifies that DMSO will remain within the particle-stabilized droplets of our HIPE samples. The data in Table S3.1, also helps reaffirm that hexane will almost completely evaporate from the continuous phase after 5 hours of sample aging.

Table S3.1. Gas chromatography results on the solubility of DMSO in the continuous oil phase

t (hr)	Dimethyl Sulfoxide Concentration (mg/mL)	Hexane Concentration (mg/mL)
0	1.27 (0.18 wt%)	275.72 (0.61 wt%)
5	0.58 (0.07 wt%)	3.81 (<0.01 wt%)

3.5.3 *Effective Dispersed Volume Fraction Calculations*

To correct the volume fraction of the dispersed aqueous fluid phase, ϕ_A, into the effective dispersed volume fraction, ϕ_{EFF}, the presence of particles at the droplet interface is noted. In Figure S3.10, the position of a partially hydrophobic particle, $\theta > 90°$, is shown in comparison to a neutral wetting particles, $\theta = 90°$, both with a particle diameter, δ_P.

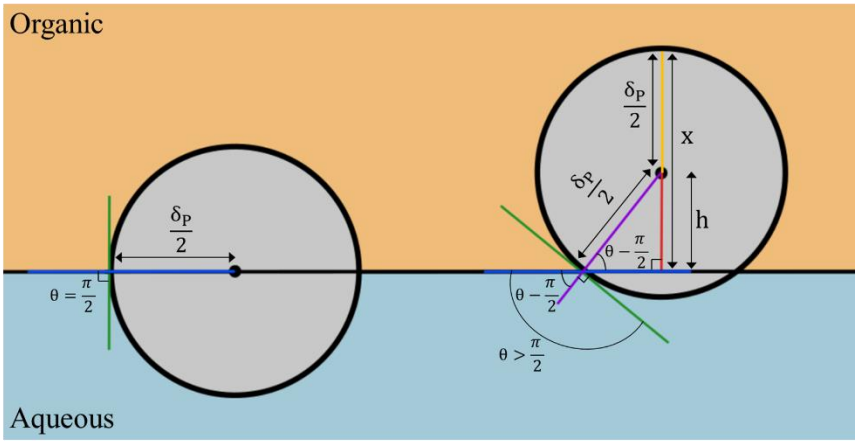

Figure S3.10. An illustration of how a neutral wetting particle, left, sits at a flat fluid interface versus how a partially hydrophobic particle sits at the interface, right.

The hydrophobic particle is observed to sit at a position in which a greater portion of the particle is in the organic phase. The additional amount the particle protrudes from the interface is captured by h, and depends on particle contact angle, θ, and particle diameter, δ_P, as expressed in Equation S3.1.

$$h = \frac{\delta_P}{2}\sin\left(\theta - \frac{\pi}{2}\right) \tag{S3.1}$$

Notice in Figure S3.10, the total amount that the particle protrudes from the interface is x, which includes h as well as half the particle diameter. The value of x is given below in Equation S3.2, and shown in Section 3.3.3 as Equation 3.2.

$$x = \frac{\delta_P}{2}\left(1 + \sin\left(\theta - \frac{\pi}{2}\right)\right) \tag{S3.2}$$

Stepping back to a broader view, Figure S3.11 illustrates a particle monolayer on a droplet interface.

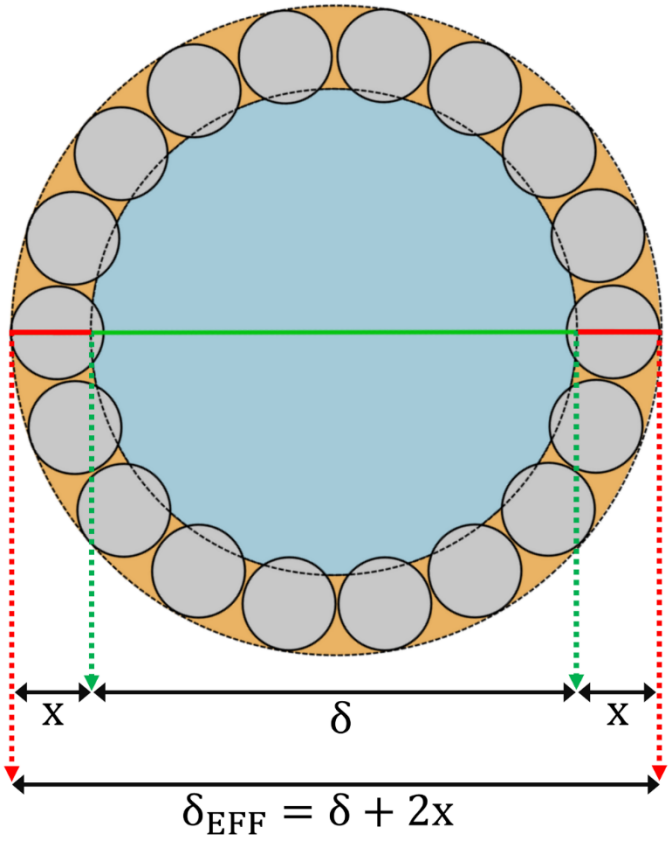

Figure S3.11. An illustration of a solid-stabilized droplet showing the impact particles have on its effective droplet diameter. Note the same figure is presented in Section 3.3.3 as Figure 3.5.

From Figure S3.11, it is evident that the effective diameter, δ_{EFF}, of the solid-stabilized droplet is larger than the bare liquid droplet diameter, δ. Accounting for this difference in droplet diameters allows ϕ_{EFF} to be determined from ϕ_A, as is done in Equation 3.1 in Section 3.3.3. The first step in evaluating ϕ_{EFF} is done by calculating the volume fraction of droplets with the effective droplet diameter, δ_{EFF}, and taking its ratio with the volume fraction of droplets with diameter, δ.

$$\frac{\phi_{EFF}}{\phi_{AQS}} = \frac{\eta^*\left(\frac{\pi^*(\delta_{EFF})^3}{6}\right)}{V_{total}} \Bigg/ \frac{\eta^*\left(\frac{\pi^*(\delta)^3}{6}\right)}{V_{total}} \tag{S3.3}$$

Note, in this conversion, the only difference considered is the droplet diameter, such that the number of droplets, η, and the total system volume, V_{total}, cancel within the calculation. Equation S3.3 simplifies to Equation S3.4, shown below, in which the relationship between δ_{EFF} and δ is inserted (see Figure S3.11).

$$\frac{\phi_{EFF}}{\phi_{AQS}} = \left(\frac{\delta+2x}{\delta}\right)^3 \tag{S3.4}$$

Further simplification and rearrangements results in Equation 3.1 of Section 3.3.3, shown below as Equation S3.5. Note that this method assumes spherical droplets, which may no longer be present in highly concentrated emulsions with faceted droplets. Also faceted droplets in highly concentrated emulsions may begin to overlap through the continuous fluid phase, assumed to be present in the particle monolayer surrounding dispersed liquid droplets. At these conditions the over estimation of ϕ_{EFF} can result in values greater than 1.

$$\phi_{EFF} = \phi_{AQS}\left(\left(1+\frac{2x}{\delta}\right)^3\right) \tag{S3.5}$$

CHAPTER 4: NON-MONOTONIC DEPENDENCE OF PICKERING EMULSION GEL RHEOLOGY ON PARTICLE VOLUME FRACTION

4.1 Background

Pickering emulsions are multiphase mixtures in which fine solid particles, typically in the colloidal range, reside at the interface between two immiscible fluids such as oil and water, kinetically stabilizing droplets against coalescence to form an emulsion[18], [19]. The equilibrium position of these interfacial particles is characterized by a three-phase contact angle, θ, which is governed by the surface energies at play as described in Young's equation[20].

$$\cos(\theta) = \frac{\sigma_{PO} - \sigma_{PA}}{\sigma_{OA}} \tag{4.1}$$

Here, σ_{PO}, σ_{PA}, and σ_{OA} refer to the interfacial tensions at the particle-organic fluid, particle-aqueous fluid, and organic-aqueous fluid interfaces, respectively. Traditionally, θ is measured through the aqueous phase in systems comprised of aqueous and organic fluids. The interfacial adsorption of a near neutral wetting ($\theta \approx 90°$) particle is typically irreversible, as the detachment energy can be several orders of magnitude greater than the particle's thermal energy, kT, where k is Boltzmann's constant and T is absolute temperature[1]. Partially hydrophobic particles with $\theta > 90°$ can still exhibit significant detachment energies for large enough fluid interfacial tensions and particle radii. In order to realize $\theta > 90°$, such particles favor the formation of aqueous-in-organic emulsions, where they slightly protrude from the aqueous droplets into the continuous organic phase. This configuration allows efficient particle packing, and sterically stabilizes the system against droplet coalescence. Since their introduction in the early 20th century, Pickering emulsions have been widely used in consumer products, from cosmetics and pharmaceuticals to food items[4], [114]. More recently, the use of solid-stabilized

emulsions in medicine[115], composite materials[116], [117] and the oil industry[118] has motivated the need to understand the salient microstructural and mechanical characteristics of these complex fluids, particularly their rheology, at a more detailed level. Specific interest in the rheology of solid-stabilized emulsions is twofold: from a technological standpoint, the rheology of Pickering emulsions directly mediates their mechanical stability, shelf life, and processability, which are crucial aspects of their use in any of the applications mentioned above. From an academic perspective, the multiphase nature of solid-stabilized emulsions and the rich interfacial phenomena at play in these systems give rise to complex mechanical properties, which have been characterized and briefly discussed in a number of earlier studies[35], [80], [99], [113], [119]–[122]. In one particular class of solid-stabilized mixtures called Pickering emulsion gels, remarkable gel-like rheology has been reported and loosely linked to bridging of droplets by colloidal particles[84]. This bridging phenomenon is schematically illustrated in Figure 4.1 for an aqueous-in-organic emulsion.

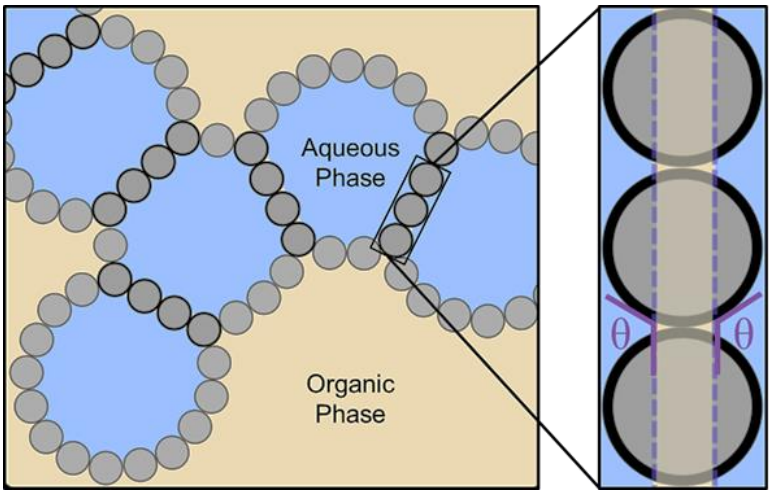

Figure 4.5. An illustration of droplet bridging in Pickering emulsion gels stabilized by spherical particles. Bridging particles are colored darker with thicker outlines for clarity, and can be seen to satisfy their equilibrium contact angle on each droplet interface they reside on.

Here, partially hydrophobic particles with $\theta > 90°$ sufficiently protrude into the continuous phase, allowing them to simultaneously adsorb onto another interface and form a

bridge between two droplets[63], [123]. As seen in Figure 4.1, particles that are shared between droplets can satisfy their equilibrium contact angle at both fluid/fluid interfaces that they reside on. Initial studies have noted strong adhesion forces between fluid interfaces that shared a bridged particle monolayer[123]–[126]. In light of this important observation, Pickering emulsion gels can be viewed as sample-spanning networks of deformable liquid droplets that are held together by adhesive bridging monolayers of solid particles. Early studies have suggested, and experimentally confirmed, that droplet bridging can yield prolonged mechanical stability and gel-like rheology in Pickering emulsions, even at volume fractions of the dispersed fluid phase and colloidal particles well below the random close packing limit of polydisperse spheres[27], [126]–[129]. In addition, droplet bridging can enhance the efficiency of separation and extraction processes in multiphase mixtures with disparate densities[65], and has also been utilized to enhance the mechanical stability of bicontinuous interfacially jammed emulsion gels (bijels) with large characteristic domains[130]. These features emphasize the importance of particle-bridged interfaces in solid-stabilized emulsions, and a number of recent studies have investigated the dependence of bridge formation on solids loading, particle wetting characteristics, and the emulsification technique employed[66], [119], [131]. However, a clear understanding of how the mixture's formulation and preparation details may affect the extent of droplet bridging, and in turn the microstructure and rheology of the final emulsion, is currently lacking. For example, a number of independent physicochemical variables including the liquid and particle volume fractions, fluid interfacial area and tension, three-phase contact angle, and particle size and shape can influence the degree of droplet bridging. Further, gelation in these systems involves an intricate kinetic competition between droplet coalescence, particle adsorption, bridging, and network formation, making *a priori* predictions of the resulting microstructure and rheology

quite difficult, if not impossible. Here we report a systematic study of Pickering emulsion gel rheology and its dependence on the amount of solids loading, liquid volume fractions, and particle size. The gel strength, as measured by the zero-shear elastic modulus, G_0', is seen to have a non-monotonic dependence on the particle volume fraction, ϕ_P. To investigate the microstructural origins of this behavior and its possible connection to droplet bridging, we use fluorescence confocal imaging to measure the average droplet size, δ, in each sample, from which the fraction of particles participating in bridging is indirectly calculated. Following this analysis, we examine the relationship between the microstructure and rheology of Pickering emulsion gels over a range of particle volume fractions and sizes, and volumetric ratios of the fluid phases. Our analysis illustrates that the degree of droplet bridging, which cannot always be systematically controlled or prescribed *a priori* in practice, is a key determinant of rheological properties in these systems. This finding has two important implications:

First, while gel-like properties in these systems stem from a percolating network of solid particles, the amount of solids loading is not the primary variable to control Pickering emulsion gel rheology. Various other factors such as particle size, liquid volume fractions, particle adsorption and droplet coalescence dynamics, and even sample preparation protocol are additionally at play, each influencing the extent of droplet bridging in a nontrivial manner. Therefore, the rheology of Pickering emulsion gels must be reported with this concept in mind, which has been overlooked in previous studies. We examine this notion in Section 4.3.3, and suggest a combination of parameters related to the initial degree of droplet surface coverage, instead of particle volume fraction, to be used in reporting the experiments.

Second, the complex parameter space governing the physics and dynamics of bridging provides a host of potential control knobs for formulation of solid-stabilized emulsions and

precise engineering of their rheology for various end uses. Given that the degree of droplet bridging cannot be readily prescribed in experiments, our study also motivates the need for future research in this area to better understand the means, both kinetic and thermodynamic, to control this parameter and precisely tune the microstructure and rheology of these multiphase complex fluids for each application.

4.2 Experimental Methods

4.2.1 Particle Synthesis

Three batches of fluorescent colloidal silica particles were prepared by a modified Stöber synthesis procedure[100], [101] and characterized by Scanning Electron Microscopy (Quanta 3D FEG, Thermo Scientific). A large batch of particles with diameter δ_p = 675 nm, and coefficient of variation CV = 4.6%, was used to comprehensively investigate the isolated role of solids loading on the rheology of Pickering emulsion gels (17 samples tested at different particle volume fractions and fixed volumetric ratio of the fluid phases). A subsequent large batch of particles, δ_p = 610 nm and CV = 3.1%, was used to add the combined effects of solids loading and volumetric ratio of the dispersed to continuous fluid phases (30 samples tested at varying particle and fluid volume fractions). Finally, a small batch of particles, δ_p = 433 nm and CV = 4.1%, served to add particle size effects to the results of the other two batches. The first step in forming particles was creating a fluorescent dye solution by reacting 18.75 mg fluorescein isothiocyanate (Fisher Scientific) with 79.2 μL 3-aminopropyltriethoxysilane (TCI America) in 15 mL anhydrous ethanol (Fisher Scientific). The reaction was carried out overnight at room temperature in a 20 mL vial under continuous magnetic stirring. For a yield of ~1 g colloidal silica, a 250 mL flask was charged with 56 mL anhydrous ethanol, 10 mL chilled 30 wt% ammonia solution (Fisher Scientific), 4.18 mL tetraethyl orthosilicate (Sigma Aldrich), and 5 mL

dye solution. Particle synthesis was carried out unperturbed in a refrigerator for 3 hours; after which an appropriate amount of hexamethyldisilazane (HMDS, Alfa Aesar, 6.2 mL in this case) was added to the mixture and allowed to react undisturbed overnight, rendering the particles' surface chemistry partially hydrophobic. For a greater yield of silica particles (~7 g), the reaction was scaled up to a 1000 mL flask charged with 370 ml anhydrous ethanol, 60 mL chilled 30 wt% ammonia solution, 30 mL tetraethyl orthosilicate and 30 mL dye solution. The large-scale reaction was carried out overnight at room temperature under continuous stirring by a magnetic stir bar. Addition of HMDS (65 ml) occurred 3 hours into the reaction. All resulting silica particles were collected and washed in 190 proof ethanol by repeated centrifugation, dried at 110°C in a vacuum oven and transferred to a capped vial. The particles' wetting properties with respect to the fluid phases were characterized by measuring the equilibrium three-phase contact angle with the immersed droplet method[71] (see Figure S4.1 in Section 4.5.1). All particle batches utilized in this study exhibited contact angles of ~135°, and were experimentally observed, by confocal microscopy, to stabilize aqueous-in-organic droplets (the fluids were distinguished from one another by selectively dyeing the aqueous phase with rhodamine B) while protruding sufficiently into the organic phase to facilitate droplet bridging.

4.2.2 Sample Formation

Pickering emulsion gels were formed by dispersing a recorded volume fraction of silica particles into an immiscible two-phase liquid mixture, with an ultrasonic probe (Branson Sonifier 250), run continuously for ~20 sec at 2.5 W power. In calculating the experimental particle volume fraction the density of silica was taken to be 2.02 mg/μL[117]. The composition of each fluid phase was chosen to approximately match the refractive index of colloidal silica, $\eta_p \approx 1.43$. The aqueous phase consisted of 65/35 v/v dimethyl sulfoxide and water, while the organic phase

was an 82/18 v/v mixture of dodecane and toluene. The interfacial tension between the two fluid phases was measured to be σ_{OA} = 19.8 mN/m at 25°C with a Sigma 701 tensiometer. Ultrasonication visibly induced gelation as initially liquid-like samples were observed to transition into macroscopically homogeneous self-supporting gels. In all gel samples, the total liquid mixture volume was held constant at 600 μL, while the ratio of aqueous to organic phase and particle volume fraction were adjusted as needed for the various experiments. Each sample was divided into two parts after formation. Approximately 500 μL of the gel was placed on a rheometer stage for mechanical testing. The rest was transferred onto a glass microscope coverslip for confocal imaging.

4.2.3 Confocal Microscopy

Pickering emulsion gel samples were visualized by an inverted microscope (Axio Observer A1, Carl Zeiss Microimaging, Inc.) attached to a confocal scanner (Vt-eye, Visitech International) using a 20X NA = 0.4 objective to image the overall microstructure, and a 100X NA = 1.4 oil-immersion objective for discerning the details of a bridging monolayer. Importing confocal images into ImageJ software, the average droplet diameter was determined by utilizing the "straight line" tool and manually recording the diameter of ~20 droplets within each sample. In performing these measurements, we only considered the inner dark region of each droplet, to account for the fact that particles protrude from the droplet surface in our samples (see Figures S4.7 and S4.8 in Section 4.5.2 for a better illustration of this concept). The analysis of this average droplet size data yielded a measure of the degree of droplet bridging in a Pickering emulsion gel, as discussed in the Section 4.3.1. Imaging was typically done at a distance ~50 μm away from the bottom coverslip to minimize wall effects while obtaining images with sufficient spatial resolution to discern the salient microstructural details.

4.2.4 Rheometry

The rheological behavior of Pickering emulsion gels was characterized using a stress-controlled rheometer (AR-G2, TA Instruments) with a sandblasted parallel-plate geometry (diameter d = 25 mm) at a set temperature of 25°C. After their formation by ultrasonication, gel samples were carefully loaded onto the rheometer stage with a spatula and the upper plate was slowly brought down to a gap height of 300 μm. Each gel sample loaded onto the rheometer first underwent a frequency sweep between f = 0.1 – 80 Hz at a constant oscillatory strain of γ = 0.1%, followed by an oscillatory strain sweep spanning γ = 0.01 – 1000% at a constant frequency f = 1 Hz. Recorded throughout both tests were the storage modulus, G', and the loss modulus, G''. The zero-shear elastic modulus, G'_0, was calculated as the average value of G' over the range $0.01\% < \gamma < 0.1\%$ within the oscillatory strain sweep, where all samples showed a plateau in G'.

4.3 Results and Discussion

4.3.1 Non-Monotonic Dependence of Gel Strength on Particle Volume Fraction

Figure 4.2 shows representative confocal images of Pickering emulsion gels prepared at an aqueous-to-organic volumetric ratio of η = 30/70 and various particle volume fractions, ϕ_P. Their overall microstructure bears close resemblance to dense colloidal gels[43]–[45], [132], as a tenuous, percolating network of aqueous droplets within a continuous organic fluid phase is observed. Droplets within the network interior are primarily bridged with their neighbors by colloidal particles, while the network exterior surfaces comprise fluid interfaces covered and stabilized by particle monolayers, but without bridging. As ϕ_P increases, droplet size is qualitatively seen to decrease. At large ϕ_P, the connectivity of the droplet network begins to diminish, as droplet clusters, disconnected from the percolating network, start to arise.

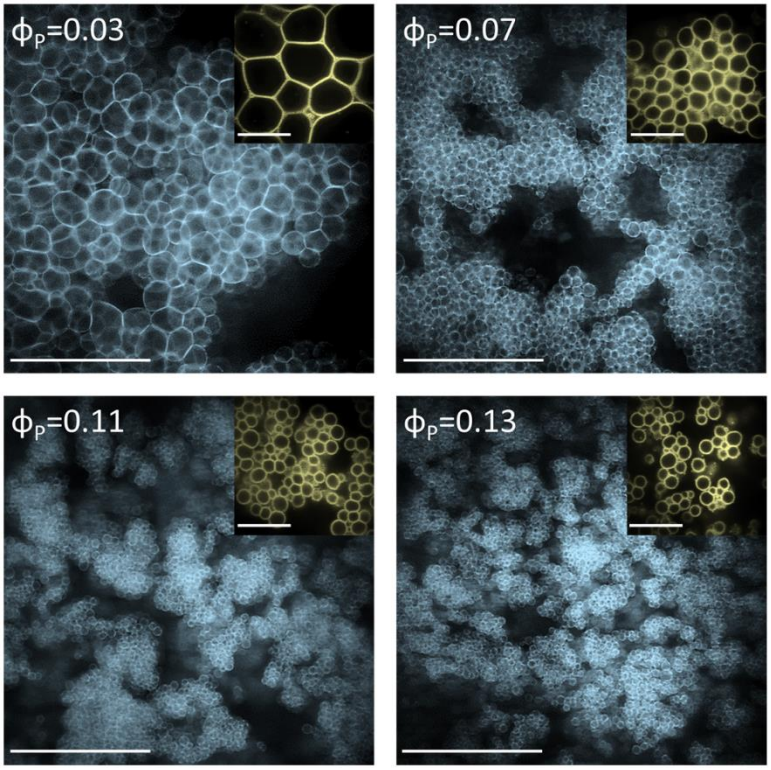

Figure 4.2. Confocal microscopy images of Pickering emulsion gels prepared at η = 30/70 and various particle volume fractions. The increase in solids loading yields a decrease in droplet size and loss of network connectivity at the highest ϕ_P examined. Scale bars of image and inserts correspond to 100 μm and 20 μm, respectively.

At the highest particle loadings shown in Figure 4.2, ϕ_P = 0.13, even individual round droplets are occasionally seen within samples. These microstructural changes point to potentially curious rheological behavior as ϕ_P is varied, which we present below. Frequency sweep tests on representative samples exhibit signatures of gel-like rheology with a nearly frequency-independent $G' > G''$ (see Figure S4.2 in Section 4.5.1). The results of oscillatory strain sweeps on the samples shown in Figure 4.2 are plotted in Figure 4.3. Note for clarity only the first three samples (ϕ_P = 0.03, 0.07 and 0.11) are plotted. Hallmarks of colloidal gel behavior with a plateau in $G' > G''$ at low strains and a crossover to $G' < G''$ at greater strains, indicative of yielding, are evident. It is clear from Figure 4.3 that the strength of Pickering emulsion gels, measured by the elastic modulus plateau, is highly dependent on ϕ_P. This dependence was investigated in depth with samples prepared at η = 30/70 and a relatively wide span of ϕ_P.

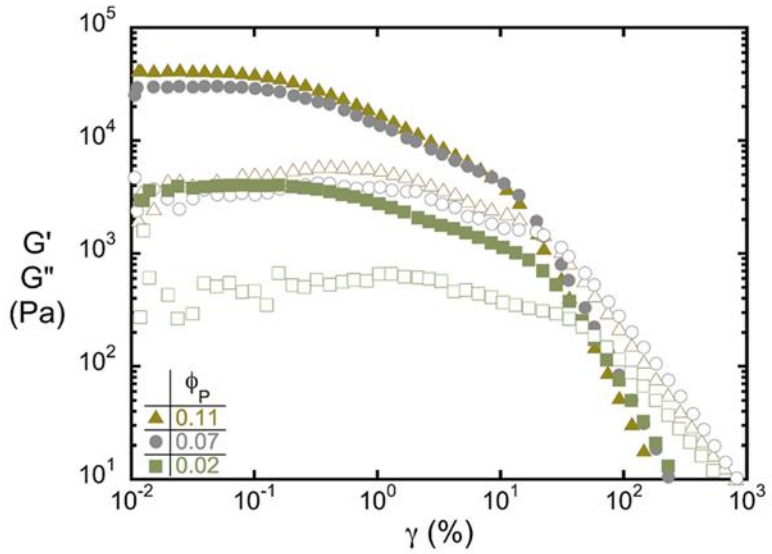

Figure 4.3. Oscillatory strain sweeps, measured at a constant frequency f = 1 Hz, for Pickering emulsion gel samples prepared at η = 30/70 and different particle volume fractions. G′ and G″ are represented by solid and hollow markers, respectively.

The zero shear elastic modulus, G_0', extracted from the G′ plateau in oscillatory strain sweeps, is plotted against ϕ_P in Figure 4.4a, showing a notable non-monotonic dependence on particle volume fraction. From $\phi_P \approx 0.03$ to 0.065 (Region I in Figure 4.4a), the dependence of G_0' on ϕ_P follows a power law scaling with $G_0' \sim \phi_P^{2.3}$ (indicated by a red dashed line). This trend is consistent with previously reported studies of the rheology of Pickering emulsion gels[35], [119], and has been loosely rationalized in light of their microstructural similarity to dense colloidal gels for which power-law scaling of G_0' with ϕ_P is ubiquitously reported and connected to the fractal geometry of the gel backbone[122–125]. Not noted previously, is a departure from power-law dependence observed at larger particle volume fractions. At $\phi_P \approx 0.065$, power-law scaling gives way to an apparent linear growth of the zero shear elastic modulus (Region II in Figure 4.4a, indicated by a blue dashed line) until $\phi_P \approx 0.11$, where G_0' abruptly begins to decrease (Region III in Figure 4.4a).

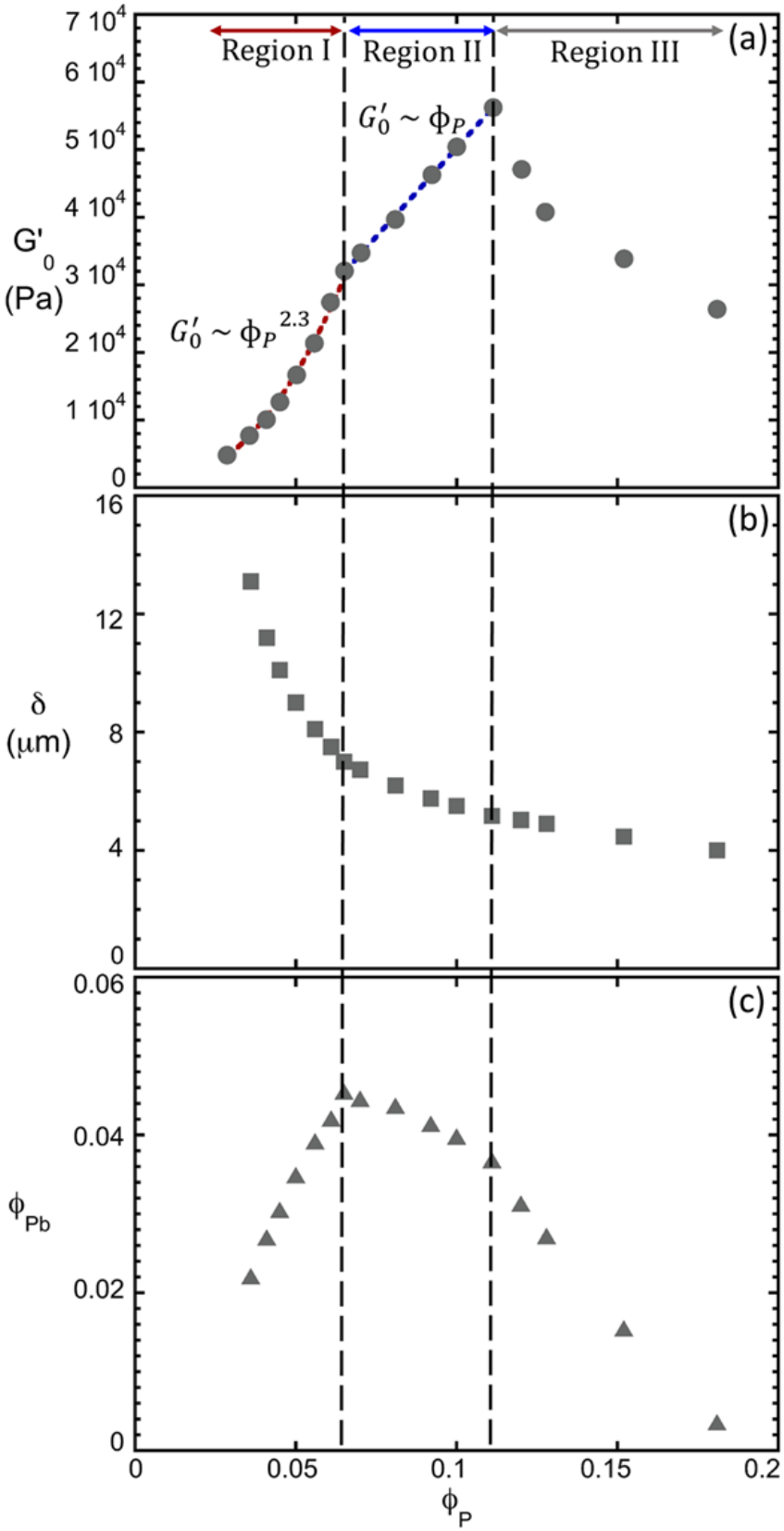

Figure 4.4. Plotted against particle volume fraction is (a) the zero shear elastic modulus, (b) average droplet diameter and (c) bridging density in Pickering emulsion gels prepared at η = 30/70.

These results immediately unravel important rheological features of Pickering emulsion gels that were previously unknown. First and foremost, gel strength does not continuously rise with particle loading. At sufficiently large ϕ_P, the behavior is reversed, and further addition of particles to the mixture results in gel weakening. Second, the strengthening regime itself is comprised of two separate regions with different dependencies of G_0' on ϕ_P. To resolve the microstructural origins of this behavior, we used confocal microscopy to assess the shape and average size of droplets within each tested gel sample. In Figure 4.4b, the average droplet diameter, δ, is seen to sharply drop initially and then asymptotically approach a plateau over the range of ϕ_P investigated. Using the analysis that follows, these extracted values were employed to quantify the extent of particle-induced droplet bridging in each sample. In an ordinary solid stabilized emulsion devoid of bridging, the observed diameter of spherical droplets can be related to the volume of neutral wetting particles ($\theta = 90°$) needed to fully cover the available droplet surface area in a closed packed arrangement, if the particle size and total droplet volume are known[1]. In Equation 4.2 below, we have re-derived this relationship for partially hydrophobic particles ($\theta > 90°$) used in our study (see Section 4.5.2 for the derivation of Equation 4.2).

$$V_{Pt} = \frac{2\pi}{\sqrt{3}} \frac{V_D \delta_P \delta_\theta^2}{\delta^3} \tag{4.2}$$

Here V_{Pt} gives the theoretical volume of particles with diameter δ_P that would be required to achieve full surface coverage in an ordinary Pickering emulsion of spherical droplets with diameter δ and total droplet volume V_D, and δ_θ is an effective droplet diameter that accounts for the protrusion of partially hydrophobic particles from the liquid interface, and is related to the fluid droplet diameter, δ, by the particle contact angle, θ. For an experimental Pickering emulsion gel sample δ_P and V_D are known beforehand such that V_{Pt} can be calculated once the

average droplet diameter is determined by confocal microscopy. The calculated V_{Pt} quantifies the particle volume required to prepare an ordinary Pickering emulsion with the same droplet and particle size as in the experimental sample, but without droplet bridging. Since particles that participate in bridging simultaneously reside on two fluid interfaces, V_{Pt} is expected to be larger than the actual experimental volume of particles, V_{Pe}, used to prepare the Pickering emulsion gel. This is a result of each bridging particle displacing twice as much fluid interfacial area, and therefore being double-counted in the theoretical estimation of particle volume where no bridging occurs. Under this line of reasoning, the difference between V_{Pt} and V_{Pe} will directly give the volume of bridging particles in the experimental sample, V_{Pb}:

$$V_{Pb} = V_{Pt} - V_{Pe} \tag{4.3}$$

Knowing the total liquid volume, V_L, with which the Pickering emulsion gel is prepared, V_{Pb} can be converted to an intensive variable that quantifies the degree of droplet bridging:

$$\phi_{Pb} = \frac{V_{Pb}}{V_L + V_{Pe}} \tag{4.4}$$

With this definition, ϕ_{Pb} represents the volume fraction of particles that simultaneously reside on two fluid interfaces and bridge droplets, or the volume fraction of particle bridges. From hereon, we will refer to this parameter as the bridging density. Note, the ratio ϕ_{Pb}/ϕ_P would quantify the fraction of all particles in the system that participate in bridging. For brevity, we will only discuss the variations in ϕ_{Pb} here, which correctly captures the significance of droplet bridging in Pickering emulsion gel rheology. Figure 4.4c shows variations in ϕ_{Pb}, extracted from measured δ values and Equation 4.4 as described above, with particle loading. An initial rise in ϕ_{Pb} is followed by a sharp drop as the particle volume fraction is increased. As indicated by the first

vertical dashed black line in Figure 4.4, the peak in ϕ_{Pb} coincides with the transition from power law to linear scaling of G_0' with ϕ_P. It is evident that particle loading simultaneously affects the microstructure and rheology of Pickering emulsion gels in a nontrivial manner. To explain the observed trends, we first examine how the microstructure of a Pickering emulsion gel evolves during its formation[66], [72]. In Figure 4.5 we schematically illustrate the evolution of Pickering emulsion gels prepared at a constant η and four representative particle loadings (ϕ_{P1} - ϕ_{P4}) that are presumed to span the three regions of behavior identified in Figure 4.4a. Therefore, the range of ϕ_P represented is considered to be above the minimum particle loading needed for sample-spanning network formation.

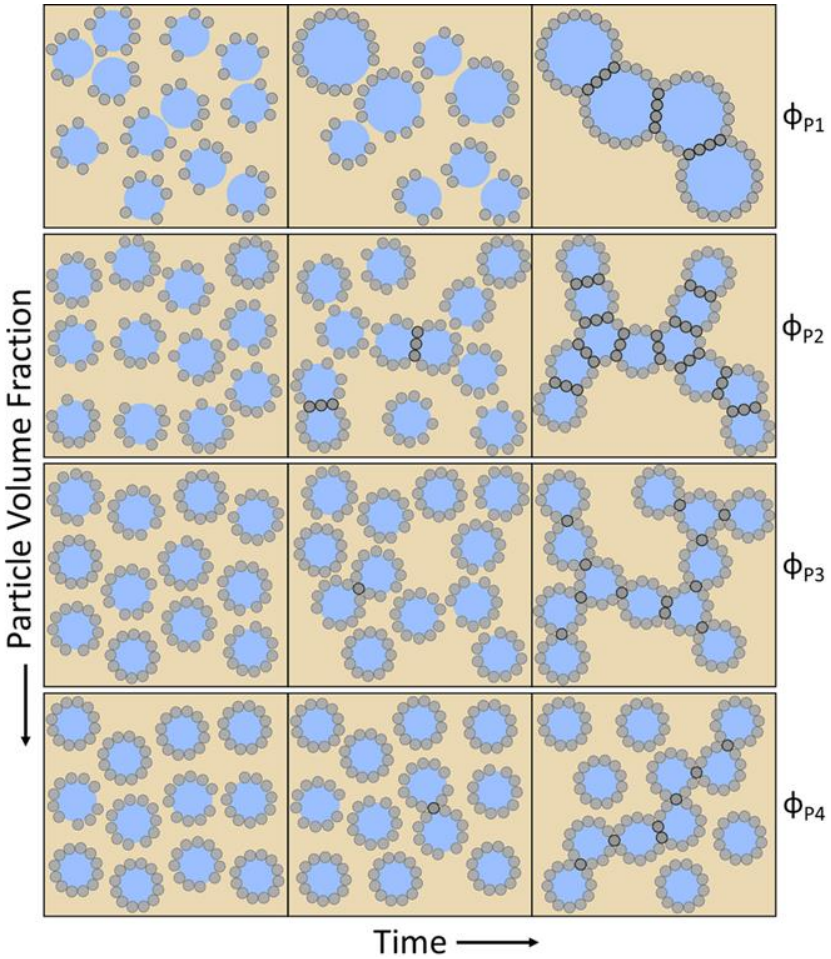

Figure 4.5. An illustration of Pickering emulsion gel formation at four representative particle volume fractions, $\phi_{P1} \rightarrow \phi_P$. Particles that participate in bridging are denoted by bold outlines for easy identification.

For the representation shown in Figure 4.5, the rate of particle adsorption onto available fluid interfaces is taken to be much faster than the droplet coalescence rate. This assumption is justified by the size contrast between the droplets and the particles. These conditions result in an initial population of dispersed droplets that are partially armored with colloidal particles, and subsequently undergo interactions that can result in either full or partial coalescence, particle bridge formation, or stable collisions, with the particular outcome depending primarily on the extent of droplet surface coverage, and, to a secondary level, its uniformity. In such a case, coalescence, bridging, and stable collisions become the dominant inter-droplet interaction modes at low, intermediate, and high (near-full) coverage, respectively. Given the constant ultrasonication power used for initializing the samples throughout our study, it is reasonable to assume that the initial droplets are of similar size but differing degrees of patchiness in the different experiments. We believe this initial droplet patchiness to ultimately govern the resulting microstructures of Pickering emulsion gels and their intriguing rheological behavior. As illustrated in Figure 4.5, at the smallest particle volume fraction shown, ϕ_{P1}, early inter-droplet collisions result in coalescence until the surface coverage grows (through an increase in average droplet size) into the intermediate range, and bridging ensues. The resulting microstructure in this case is a network of bridged droplets with average size larger than the starting value. At $\phi_{P2} > \phi_{P1}$, the initial surface coverage is already in the intermediate range, which curtails droplet coalescence and promotes bridging from the start. The ensuing microstructure is again a network of bridged droplets, but with two important differences as compared to that at ϕ_{P1}: a smaller average droplet size, and a larger number density of particles that participate in bridging. As such, the range of ϕ_P bounded by ϕ_{P1} and ϕ_{P2} exhibits a continuous increase in bridging density, concomitant with a decrease in droplet size. This behavior reasonably captures the trends seen in

Region I of Figure 4.4, and ϕ_{P2} thus represents the particle loading near where ϕ_{Pb} is maximized. Within this framework, the power-law scaling of the zero-shear elastic modulus in Region I probably encompasses a simultaneous increase in both the total amount of solid particles and the bridging density in a tenuous network of bridged droplets. Beyond ϕ_{P2}, the increase in the initial droplet surface coverage progressively decreases the rate of bridge formation in lieu of collisions that are stable against coalescence or bridging. The terminal microstructure in this region, represented by ϕ_{P3}, is a network of droplets at approximately their initial size, but with a smaller bridging density when compared to ϕ_{P2}. Therefore, the region bounded by ϕ_{P2} and ϕ_{P3} is characterized by an increase in total solids loading and a decrease in bridging density while the droplet size remains roughly constant. We assume that increasing the amount of solids within a sample-spanning colloid network will enhance the mixture's elastic modulus. Therefore, the concurrent increase in ϕ_P and decrease in ϕ_{Pb} will presumably have opposing effects on G_0', and their combined outcome is a gradual, linear increase in G_0' with ϕ_P as seen in Region II of Figure 4.4a. By comparing the slope in G_0' over δ^{-1} in this region, ~500 mN/m (see Figure S4.3 in Section 4.5.1), to the interfacial tension, ~20 mN/m, the elasticity of Pickering emulsion gels is not mediated by droplet deformation alone, further corroborating the important role of bridging interactions in the mixture's mechanical properties. Beyond ϕ_{P3}, the initial droplet population is nearly fully armored. The scarcity of bare or patchy droplet interfaces hinders droplet coalescence and bridging, resulting in small clusters of partially coalesced or even individual droplets that coexist with, but disconnected from, the sample-spanning network, as schematically represented by ϕ_{P4} in Figure 4.5. Therefore, this region is characterized by a decrease in both the bridging density and the amount of solid particles within the sample-spanning colloid network (note the disconnected clusters are not counted as part of the percolating network). The net

result is a continuous loss of gel strength with particle volume fraction, as seen in Region III of Figure 4.4a (demarcated by the second vertical dashed black line). A microstructural signature of Region III is the emergence of spherical droplets and a higher occurrence of curved colloid-laden interfaces as opposed to droplets faceted by flat, shared monolayers of particles. This is a natural consequence of the higher initial surface coverage and lower frequency of droplet collisions that result in bridging. The microstructural signatures discussed above can be clearly observed in the confocal micrographs of Figure 4.2, and the variation of δ with ϕ_P presented in Figure 4.4b. Our experimental observations thus corroborate the scenarios illustrated in Figure 4.5, and shed light on the nontrivial role that particle loading has on the microstructure, stability, and mechanical properties of solid-stabilized emulsions and similar multiphase mixtures. Before proceeding, it is important to note that the theoretical particle volume required to stabilize spherical droplets of a known size (Equation 4.2) assumes that every particle in the mixture resides at a fluid-fluid interface. At the highest values of ϕ_P tested, this assumption may no longer be valid, since ultrasonication (here utilized to initialize the samples) can only result in a finite amount of available fluid interfacial area. Our confocal images at $\phi_P = 0.18$ corroborate this notion, as they show a small population of free particles suspended in the continuous phase after the sample has reached its terminal state (see Figure S4.4 in Section 4.5.1). Notwithstanding this observation, the explanation of the trends in ϕ_{Pb} and their correspondence with G_0' still hold.

The connection between bridging density and gel strength in Pickering emulsion gels is also expected to be a key aspect of their yielding in response to external shear stresses. To examine this notion with a simple experiment, a Pickering emulsion gel sample at $\phi_P = 0.05$ and η = 30/70 was subjected to steady shear at $\dot{\gamma}$ = 50 sec^{-1} for 2 min. Microstructural characterization of the sample before and after the application of shear showed a significant loss

of bridges upon shear flow (see Figure S4.5 in Section 4.5.1). Therefore, it is conceivable to assume that mechanical yielding of Pickering emulsion gels, the onset of which appears as a small hump in G'' in Figure 4.3 followed by a precipitous drop in G', also coincides with a loss of inter-droplet bridges. This notion is consistent with the yielding behavior of attractive emulsions reported previously[31], and presents new questions for future research in this area.

Our experiments so far have examined the isolated effects of ϕ_P variations on Pickering emulsion gels. However, the scenarios discussed in Figure 4.5 point to a more convoluted set of variables and control knobs including initial droplet size, liquid volume fractions, and particle size and shape, that can be utilized to tune the bridging density, and, ultimately, the rheology of the resulting mixture. Following experiments look to investigate such scenarios through variations in the fluid volume ratio and particle size. The shear intensity at which a Pickering emulsion gel is formed and its shear history can also influence its resulting rheological behavior[56,105]. These factors have not been thoroughly examined here, but a few equivalent samples at $\phi_P = 0.08$ and $\eta = 30/70$ were formed by systematically reducing the ultrasonication power used to initialize the mixtures. Characterization of these samples showed a decrease in both G_0' and ϕ_{Pb} as ultrasonication power is reduced (see Figure S4.6 in Section 4.5.1); similar to trends noted in earlier investigations[85,105]. These observations further corroborate the scenario depicted in Figure 4.5, and the importance of initial droplet surface coverage as a determinant of the mixture's ultimate rheological properties.

4.3.2 Behavior as the Fluid Ratio is Varied

Figure 4.6 shows the variations of G_0' and ϕ_{Pb} with ϕ_P for three sets of Pickering emulsion gel samples created at different values of η, using the second batch of colloidal particles (δ_P = 610 nm). Immediately observed here is the similar non-monotonic behavior in G_0' and ϕ_{Pb}

discussed earlier, for all three data sets. At each η investigated, the bridging density is seen to initially rise to a peak value and then steadily decrease, similar to that in Figure 4.4c. Further, the peak in ϕ_{Pb} again corresponds with the transition from power law to linear scaling of G_0' with ϕ_P, which is marked by a color-coded dashed line for each sample set. However, this transition is seen to shift to larger ϕ_P for greater values of η. This observation can be explained in light of the gelation mechanism discussed in Figure 4.5.

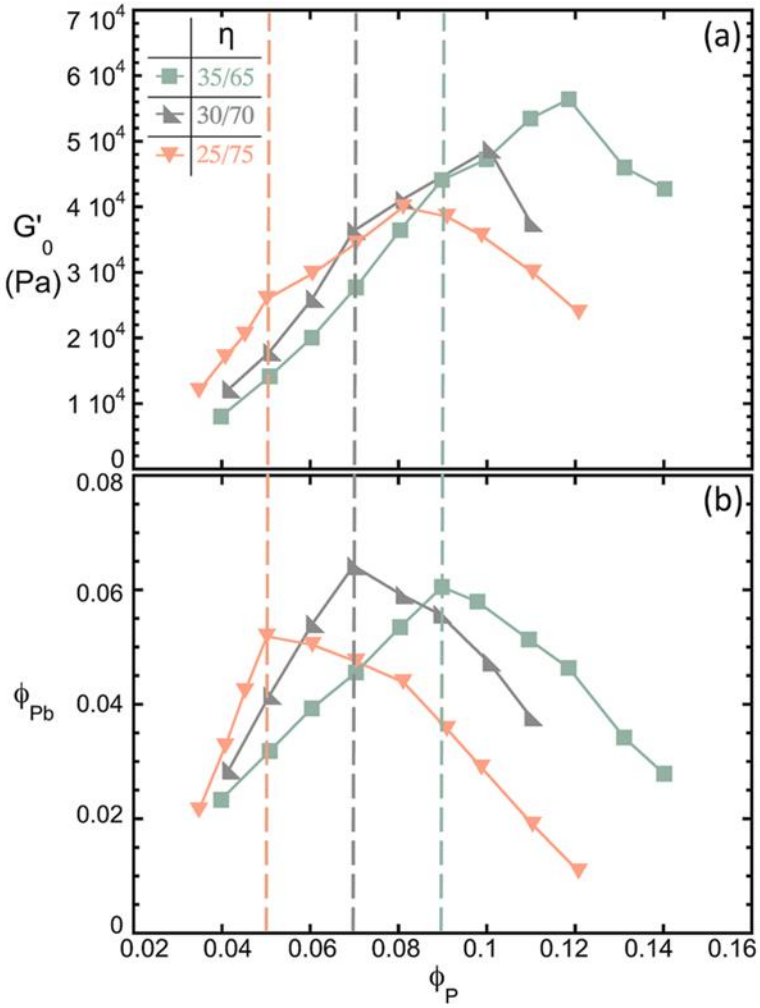

Figure 4.6. (a) Zero shear elastic modulus and (b) volume fraction of bridging particles plotted against the particle volume fraction for Pickering emulsion gels prepared at different volumetric ratios of the aqueous to organic fluid phase.

In this simple representation, the initial droplet surface coverage was proposed to be the primary determinant of bridging density, and subsequently the mixture's rheology. The

variations in η between the three sample sets cause a corresponding difference in the surface coverage of the initial droplet populations. For constant initial droplet size and particle volume fraction, samples prepared at greater dispersed-to-continuous fluid volume ratios experience less initial surface coverage. Similarly, for the same magnitude increase in ϕ_P, samples with greater η span smaller changes in droplet surface coverage. It is this correspondence between ϕ_P, η, and the initial droplet surface coverage that causes the systematic shifts in the behaviors of G_0' and ϕ_{Pb} seen in Figure 4.6. As such, these shifts may be universally captured by an appropriately defined variable that accounts for the initial droplet surface coverage. We explore this possibility next, by combining the results of all experiments conducted on Pickering emulsion gels made at various fluid volume ratios and particle sizes.

4.3.3 A Combined Variable to Parameterize the Variations of G_0' and δ

To test the effect of initial droplet surface coverage on Pickering emulsion gel microstructure and rheology, we included particle size as an additional parameter to control the initial coverage of the fluid interfaces. A set of samples at η = 30/70, using silica particles with δ_P = 433 nm was prepared and subjected to the same testing protocols as before. Together with the data presented in Figures 4.4 and 4.6, our combined experiments span a range of particle sizes and fluid volume ratios with δ_P = 433 nm, 610 nm, and 675 nm, and η = 25/75, 30/70, and 35/65. Note that practical limitations in synthesizing particles that both sufficiently adsorb onto fluid interfaces and bridge droplets, resulted in a ~250 nm particle size range in this study. Figures 4.7a and 4.7c show the collective results of all experiments, including the data of Figures 4.4a, 4.4b, and 4.6a, plotted against the particle volume fraction. As with variations in η, changing particle size results in a similar non-monotonic behavior in G_0' as seen before, with transition points shifted along the ϕ_P axis. Though not shown for the 433 nm particles, the peak

in ϕ_{Pb} is again observed to correspond with the G_0' transition between power law and linear scaling. Note that for a given particle volume fraction and fluid volume ratio, a reduction in particle size results in an increase in fluid interfacial area coverage. Similarly, smaller particles span a greater change in droplet surface coverage for the same magnitude increase in particle volume fraction than larger particles. This explains the data variations among different particle sizes in Figure 4.7a, where for smaller particles, each region of G_0' behavior (as identified previously in Figure 4.4a) is contracted (compare, for example, the data for δ_P = 433 nm and 675 nm at η = 30/70), and the peak in G_0' is shifted to lower ϕ_P.

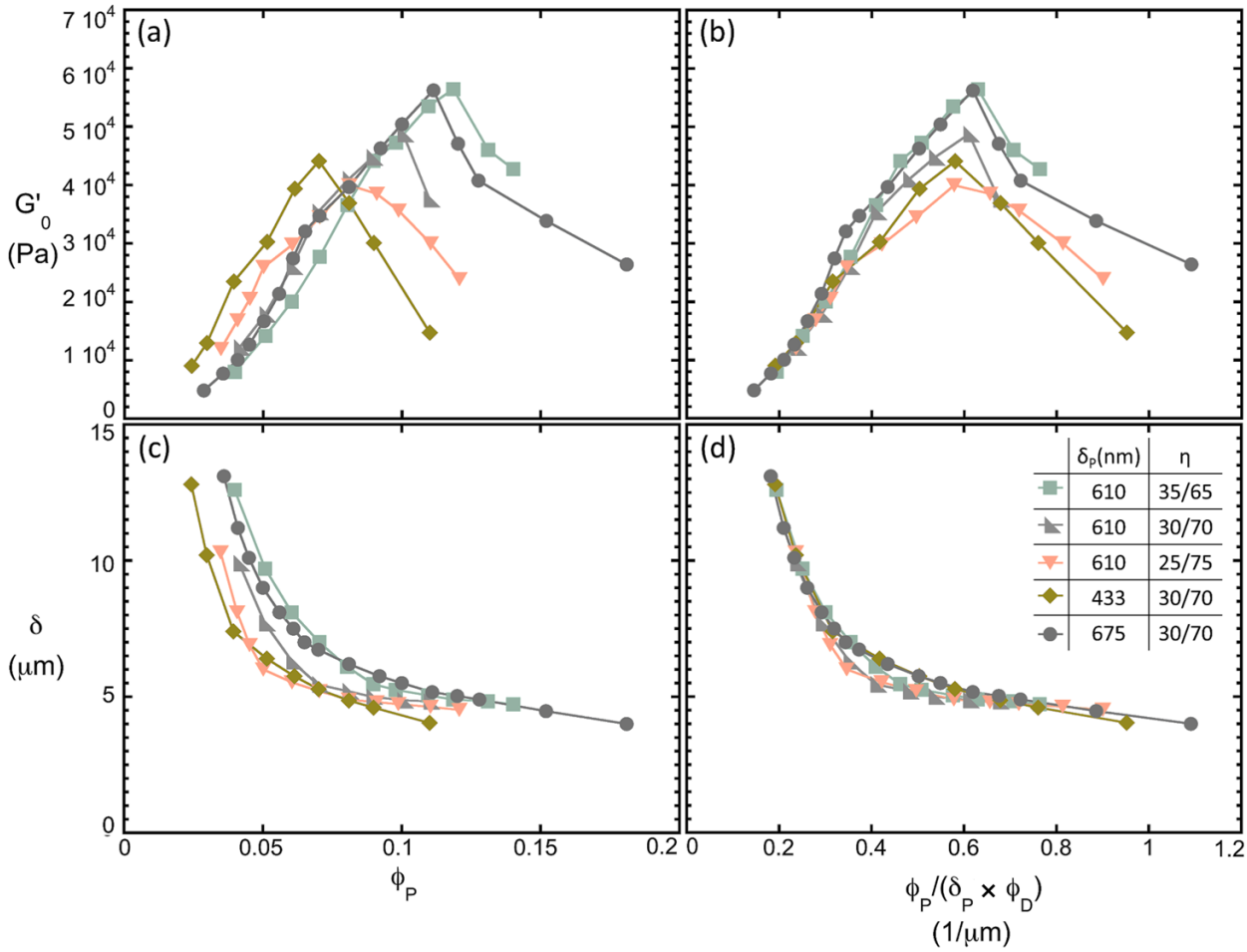

Figure 4.7. (a) G_0' plotted against particle volume fraction, ϕ_P, for various fluid volume ratios and particle sizes (b) same data as panel (a), plotted against the combined variable $\phi_P/(\delta_P \times \phi_D)$. (c) Droplet diameter, δ, plotted against ϕ_P for various fluid volume ratios and particle sizes, (d) same data as panel (c), plotted against the combined variable $\phi_P/(\delta_P \times \phi_D)$.

Collectively, Figures 4.4, 4.6, and 4.7 present a comprehensive data set in which the effects of three independent parameters on the microstructure and rheology of Pickering emulsion gels are characterized. Using this data, we sought a combined variable that would account for the observed microstructural and rheological behavior, and unify the various parameters at play, in the context of initial droplet surface coverage. As discussed earlier, a variable based on initial droplet surface coverage is motivated by the observed correlation between Pickering emulsion gel rheology and bridging density (Figures 4.4a and 4.4c), and the latter parameter's dependence on the surface coverage of initial droplets (Figure 4.5). For same-size starting droplets, surface coverage is proportional to the combined interfacial area displaced by particles divided by the dispersed liquid volume. A properly defined variable in terms of known parameters is then $\phi_P/(\delta_P \times \phi_D)$, where ϕ_D is the volume fraction of the dispersed fluid. Note that this combined variable has units of inverse length, but can be non-dimensionalized using the initial droplet diameter as a characteristic length scale (see Section 4.5.3). This non-dimensionalized variable would more directly represent the initial droplet surface coverage, but requires information (initial droplet size) not readily known before gel formation. In our study we could estimate the initial droplet diameter as its asymptotic value observed at high ϕ_P. However, we would be using information learned after gel formation and not known *a priori* as are the variables in $\phi_P/(\delta_P \times \phi_D)$. To test the applicability of $\phi_P/(\delta_P \times \phi_D)$, in Figures 4.7b and 4.7d we re-plot the data of Figures 4.7a and 4.7c, respectively, as a function of this combined variable. Here, a more coherent data set emerges from the five G_0' curves that represent variations in three independent variables (particle size and volume fraction, and fluid volumetric ratio). A complete collapse of the curves is not observed, nor expected, as the terminal microstructure and rheology of a Pickering emulsion gel depend on a more complex array of variables and kinetic

processes, and are not uniquely predicted by initial droplet surface coverage alone. As seen in Figure 4.7d, the droplet size data also converge into a more coherent set when plotted against this combined parameter. This is not surprising, as the rescaled variable $\phi_P/(\delta_P \times \phi_D)$ is inversely proportional to the theoretical droplet size for complete surface coverage conditions when particles exhibit $\theta = 90°$. Notwithstanding deviations from a complete overlap, the relative consistency among the different data sets of Figures 4.7b and 4.7d further confirms the initial droplet coverage as a variable of primary significance in mediating the terminal microstructure and rheology of Pickering emulsion gels. Note that plotting against the non-dimensionalized variable mentioned earlier would still yield the same level of coherence between data sets as seen with $\phi_P/(\delta_P \times \phi_D)$. Though it may not fully account for all the complex phenomena at play during gel formation, the combined variable, $\phi_P/(\delta_P \times \phi_D)$, provides a foundation for estimating the rheological behavior of Pickering emulsion gels from parameters known before their formation. This is utterly relevant and important for technological applications where particular flow characteristics of multiphase solid-stabilized emulsion systems are desired, and specific rheological properties must be engineered in their formulation.

4.4 Summary

We have investigated the rheology of solid-stabilized emulsions with droplet bridging, which exhibit gel-like dynamics at dispersed phase volume fractions well below the random close packing limit of hard spheres. The microstructure of these multiphase mixtures is comprised of colloid-armored fluid droplets bridged together into a percolating network by a sub-population of particles that simultaneously reside on two fluid interfaces. The zero-shear elastic modulus of these gels showed a non-monotonic dependence on solids loading with regions of power-law and linear strengthening, and subsequent weakening, which coincided with

changes in their microstructure. Specifically, the change from power-law to linear scaling of the elastic modulus coincided with a peak in the bridging density, which we indirectly calculated from the average droplet size, and gel weakening corresponded to loss of network connectivity at low bridging density (high particle volume fraction). We considered a simple representation of how the terminal microstructure of Pickering emulsion gels arises from an initial population of colloid-armored droplets with incomplete surface coverage, which suggested the initial droplet surface coverage to be of primary significance in mediating the bridging density and rheology of the final mixture. This notion was experimentally verified by examining how variations in the solid and fluid volume fractions and particle size mediate the rheology of these mixtures. Based on our findings, we suggested a combined variable, related to the surface coverage of the initial droplets, to be used in reporting the experiments. This variable provides the first means to rationalize the rheology of Pickering emulsion gels from parameters known before their formation. Its further refinement to better capture the intricacies of droplet bridging and network formation in solid-stabilized emulsions would be of great value to many applications that utilize these multiphase mixtures for various products and processes.

4.5 Supporting Information

4.5.1 Supplementary Figures

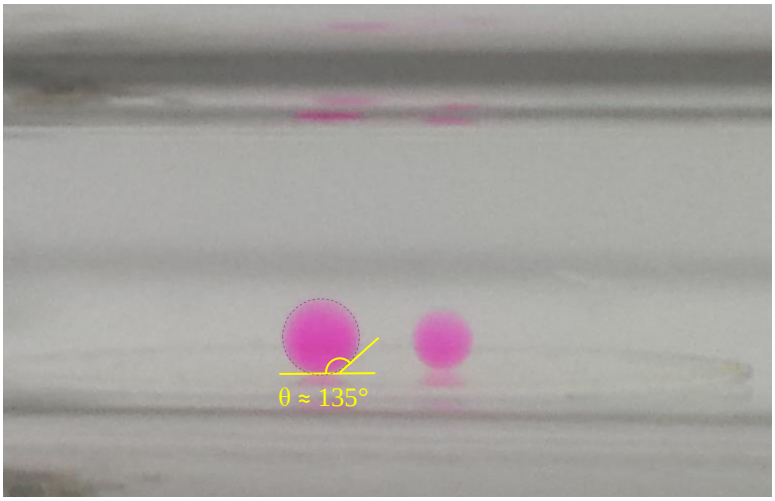

Figure S4.1. The equilibrium three-phase contact angle measured by the immersed droplet method. The aqueous droplet sits on a microscopic slide, drop-coated with silica particles, within the organic fluid phase.

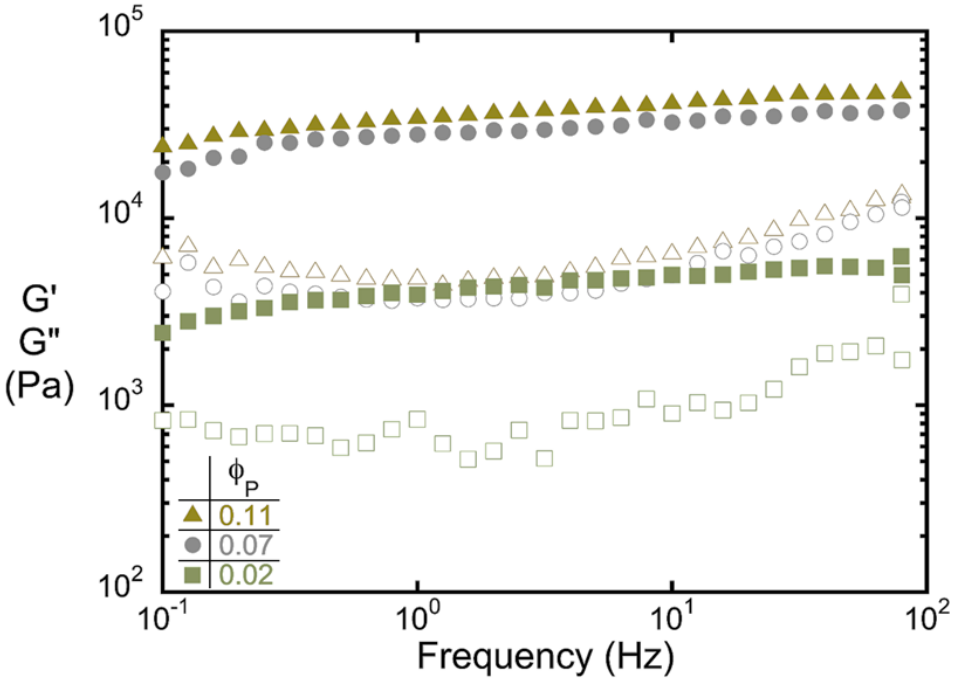

Figure S4.2. Frequency sweep results for the Pickering emulsion gels shown in Figure 4.3.

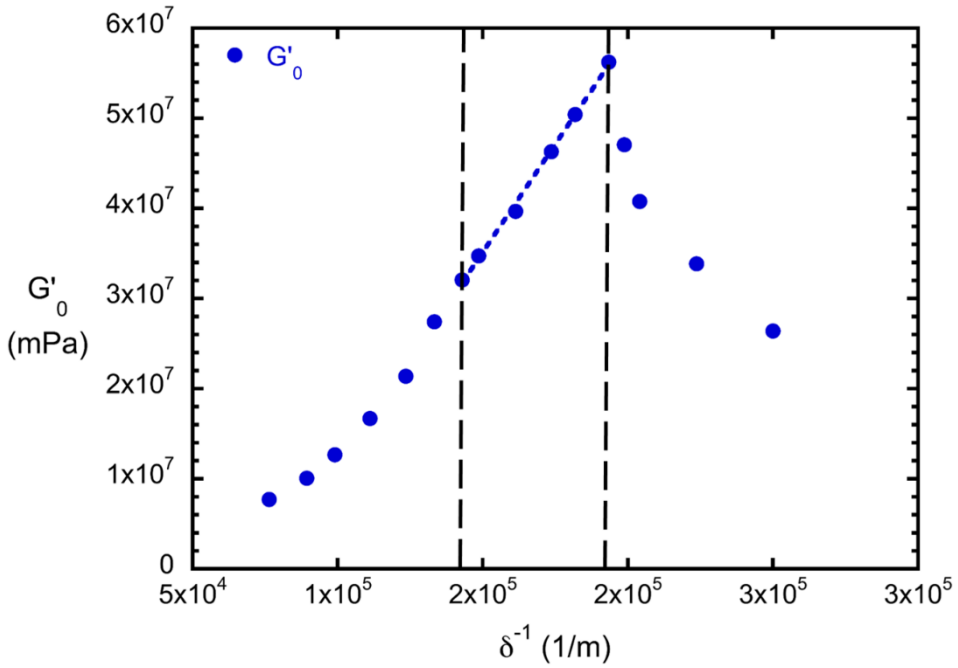

Figure S4.3. G_0' data from Figure 4.4a is plotted against inverse droplet size, 1/δ. The slope of the linear region between the dashed vertical lines is ~500 mN/m.

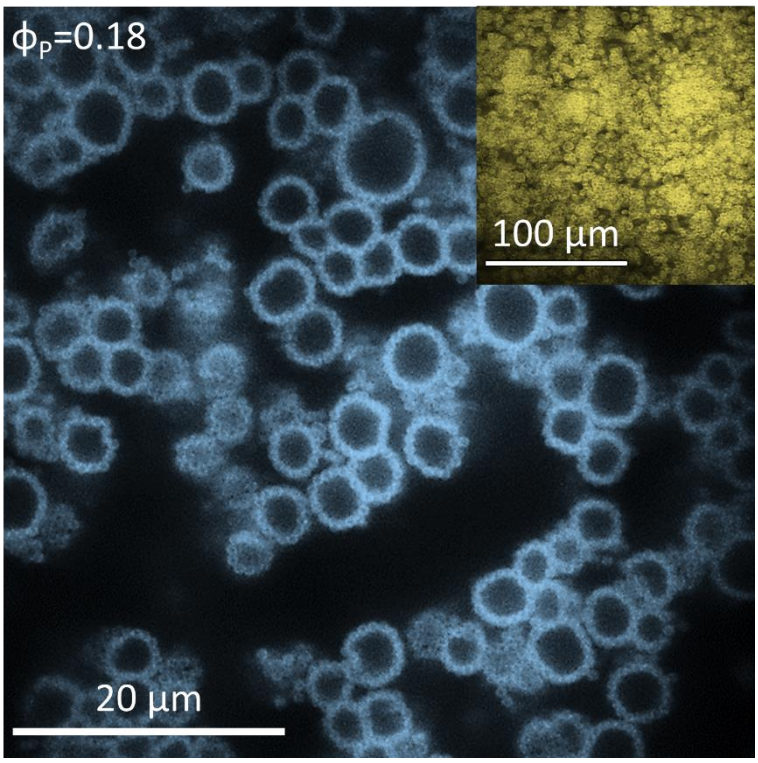

Figure S4.4. Confocal microscopy images of a Pickering emulsion gel created at a high ϕ_P, where free particles in the continuous phase are evident.

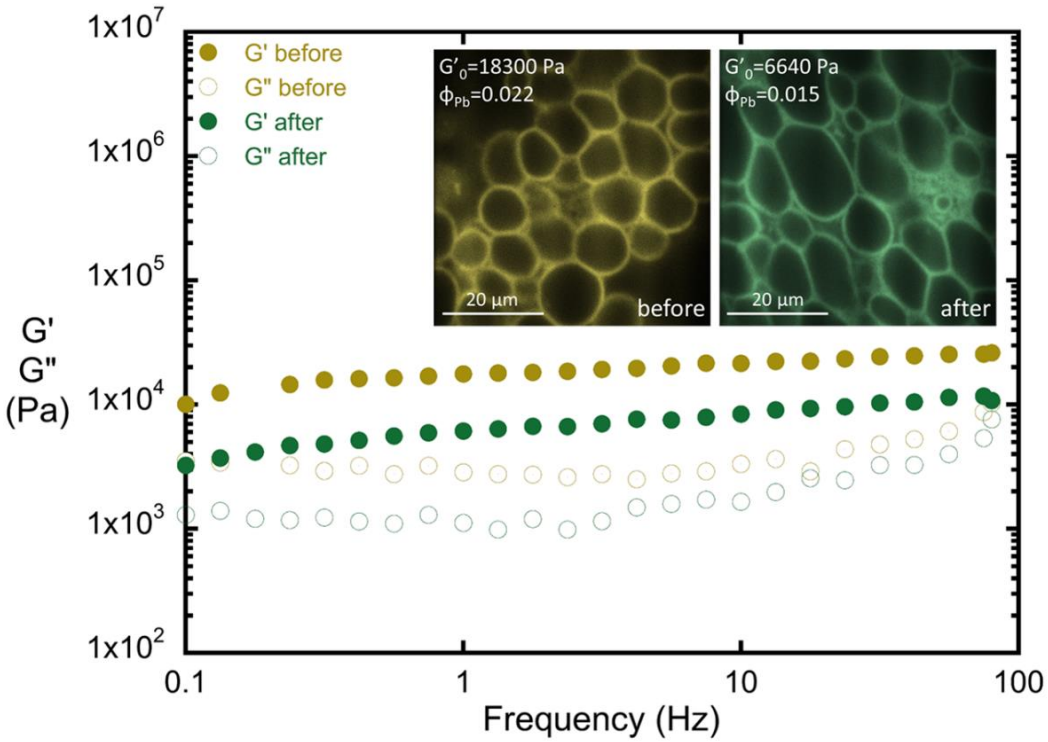

Figure S4.5. Frequency sweeps, done at $\gamma = 0.01\%$, on a Pickering emulsion gel sample, before and after, it underwent a simple shear at a low shear rate of $\dot{\gamma} = 50$ sec^{-1} for 2 minutes. The sample was prepared at $\phi_P = 0.05$ and $\eta = 30/70$.

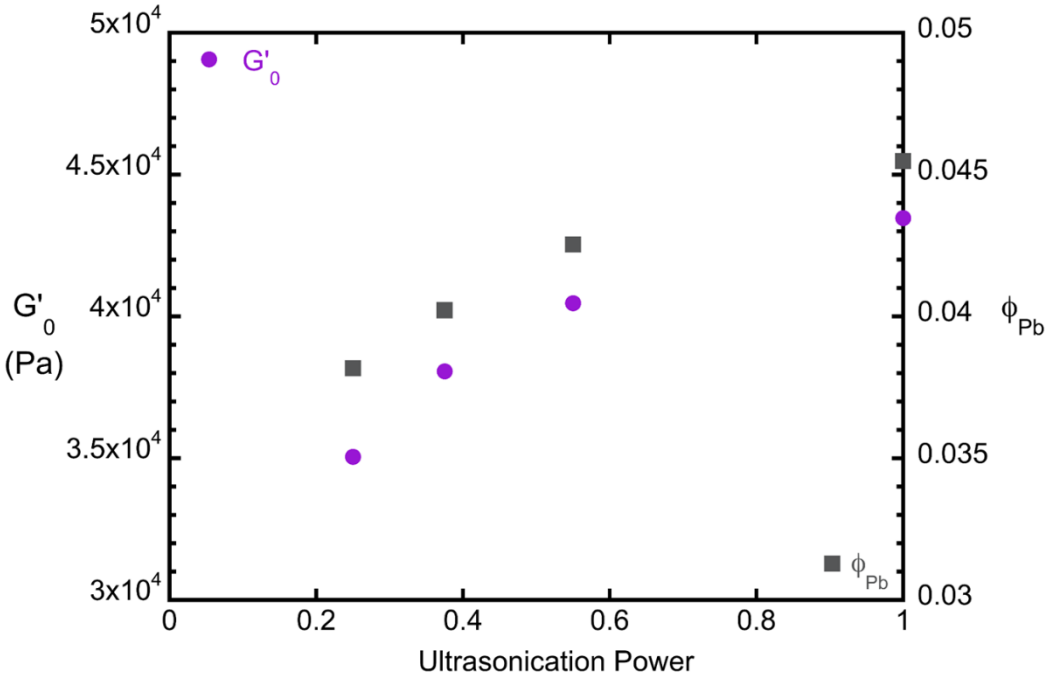

Figure S4.6. G'_0 of Pickering emulsion gel samples with the same $\phi_P = 0.085$ and $\eta = 30/70$, but formed at different ultrasonication powers. Note that the ultrasonication power was scaled by the greatest power used. On the secondary axis, ϕ_{Pb} for each sample is plotted.

4.5.2 Derivation of Equation 4.2

From geometric arguments, the volume of spherical particles, V_{Pt}, in an ordinary emulsion can be directly related to the number of particles, n_P, with diameter δ_P, as shown in Equation S4.1.

$$V_{Pt} = n_P \frac{4\pi}{3}\left(\frac{\delta_P}{2}\right)^3 \quad \text{(S4.1)}$$

The diameter of the particles, δ_P, can be determined experimentally by conducting scanning electron microscopy. The number of particles, n_P, within the emulsion however, is found by considering particle packing on the droplet surfaces, which is assumed to follow circle packing on a flat interface. If the particles are taken to pack in a hexagonal close pack arrangement, the available interfacial area, A_D, is related to the number of droplets, n_D, with diameter δ.

$$A_D = \frac{\pi}{2\sqrt{3}} n_D 4\pi \left(\frac{\delta}{2}\right)^2 \quad \text{(S4.2)}$$

Note that Equation S4.2 assumes particles exhibit a contact angle $\theta = 90°$, which is not the case in our experimental system. In our study, particles with $\theta > 90°$ are used to prepare Pickering emulsion gels with a known dispersed fluid volume, V_D. The resulting samples can analyzed by confocal microscopy to determine the droplet diameter, δ. This measured droplet diameter can be used to relate the number of droplets, n_D, to the total dispersed fluid volume using the same arguments of Equation S4.1. It cannot be used in Equation S4.2 as the diameter at which particles will sit on the droplet interface, however. An effective diameter, δ_θ, is required, that accounts for the fact that partially hydrophobic particles will protrude into the continuous phase at the droplet interface. This protrusion results in a greater effective diameter at which particles cover the fluid droplets in a hexagonal close packed arrangement. Equations S4.3 and S4.4 relate

the difference between the measured droplet diameter, δ, and the effective diameter, δ_θ,which is illustrated in Figures S4.7 and S4.8.

$$x = \frac{\delta_P}{2}\sin(\theta - 90) \quad \text{(S4.3)}$$

$$\delta_\theta = \delta + 2x \quad \text{(S4.4)}$$

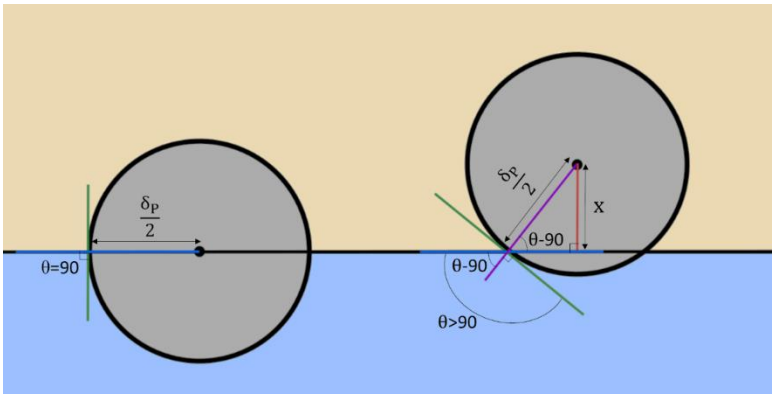

Figure S4.7. An illustration of how a neutral wetting particle, left, sits at the fluid interface versus how a partially hydrophobic particle sits at the fluid interface, right.

Accounting for the particles' partial hydrophobicity and expressing the number of droplets, n_D,

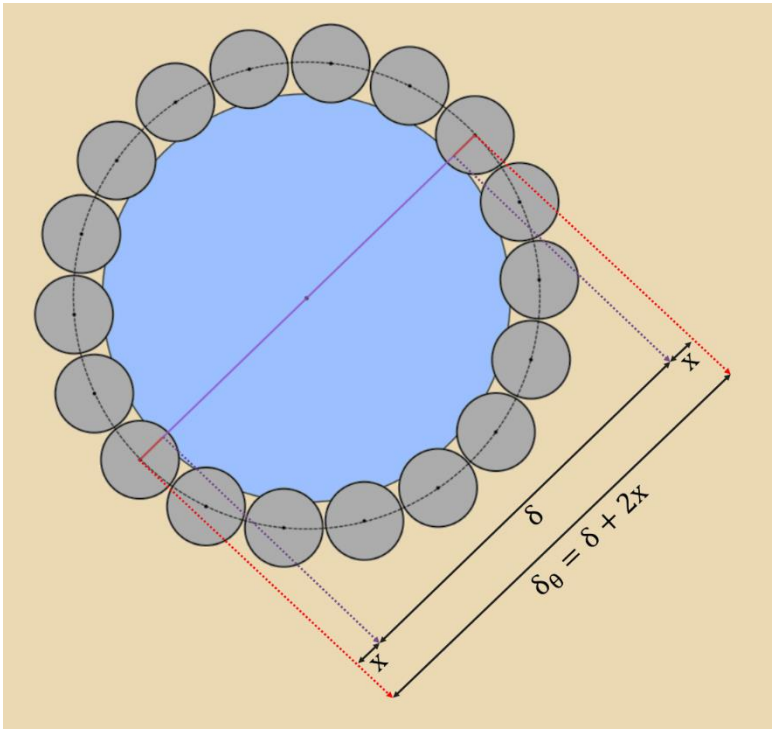

Figure S4.8. An illustration of how particles with θ > 90° pack at an effective droplet diameter, δ_θ, which is related to the measured droplet diameter, δ.

in terms of the total dispersed fluid volume, V_D, and the measured droplet diameter, δ, Equation S4.2 can be rewritten as follows.

$$A_\theta = \frac{3\pi}{\sqrt{3}} V_D \frac{\delta_\theta^2}{\delta^3} \tag{S4.5}$$

Here, A_θ, gives the actual interfacial area available in the system for particles to cover. In an ordinary Pickering emulsion with fully covered droplets, this area will be equal to the area particles can cover, A_P, which is related to number of particles, n_P, and their diameter, δ_P.

$$A_P = n_P \pi \left(\frac{\delta_P}{2}\right)^2 \tag{S4.6}$$

By setting the two areas, A_θ and A_P, equivalent to each other, the number of particles, n_P, can be expressed in terms of known or measurable variables, as seen in Equation S4.7.

$$n_P = \frac{12}{\sqrt{3}} \frac{V_D \delta_\theta^2}{\delta^3 \delta_P^2} \tag{S4.7}$$

Equation 4.2 is now derived by substituting the result of Equation S4.7 back into Equation S4.1. Here V_{Pt} gives the theoretical volume of particles with diameter δ_P and $\theta > 90°$ that is required to fully cover droplets with diameter δ in an ordinary Pickering emulsion prepared with a known dispersed fluid volume, V_D.

$$V_{Pt} = \frac{2\pi}{\sqrt{3}} \frac{V_D \delta_P \delta_\theta^2}{\delta^3} \tag{S4.8}$$

Note, if particles are neutral wetting, $\theta = 90$, then the effective diameter, δ_θ, is equal to the droplet diameter, δ, and Equation S4.8 collapses to what has been seen previously in literature.

$$V_{Pt} = \frac{2\pi}{\sqrt{3}} \frac{V_D \delta_P}{\delta} \tag{S4.9}$$

4.5.3 Non-Dimensionalization of Combined Variable

The combined variable introduced to capture changes made to the formulation of Pickering emulsion gels can be non-dimensionalized by multiplying it by a droplet diameter. Here we show that multiplying by the initial droplet diameter, δ_0, in the formation of a Pickering emulsion gel, yields a variable, K, which is effectively the surface coverage of the initial population of droplets.

$$\kappa = \frac{V_P \delta_0}{V_D \delta_P} \tag{S4.10}$$

We start with κ, which is equal to the combined variable multiplied by δ_0, but can be rewritten by using Equations S4.1 for expressions of V_P and V_D. The result of substituting these expressions in for V_P and V_D is shown below.

$$\kappa = \frac{n_P \delta_P^2}{n_D \delta_0^2} \tag{S4.11}$$

The number of particles, n_P, and particle diameter, δ_P, can be related to the interfacial area that they can cover, A_P, through Equation S4.6. Similarly, Equation S4.2 relates the total interfacial area available for particles to cover in a hexagonal close packed arrangement, A_θ, to the number of droplets, n_D, and droplet diameter, δ_0. Employing Equations S4.6 and S4.2, we arrive at the following expression for κ.

$$\kappa = \frac{2\pi}{\sqrt{3}} \frac{A_P}{A_\theta} \tag{S4.12}$$

If we let $K = \kappa \frac{\sqrt{3}}{2\pi}$, the result gives the interfacial area that a volume of particles, V_P, with diameter δ_P are able to cover, over the total interfacial area available in a population of droplets with diameter δ_0 and a total volume of V_D. Here K is the initial droplet surface coverage.

$$K = \frac{A_P}{A_\theta} \tag{S4.13}$$

CHAPTER 5: SUMMARY AND FUTURE DIRECTIONS

In this dissertation I have investigated the microstructure and rheology of various solid-stabilized emulsions. Examination of droplet coalescence in high internal phase emulsions (HIPEs), has generated a greater insight into the role particles play in stabilizing the thin films between the faceted droplets present in these concentrated systems. Particle size has been varied in my study, illustrating it influence on the interparticle interactions between interfacial particles. Future investigations into HIPE formation with droplets that exhibit either strong attractive or repulsive interactions, due to the stabilizing particles utilized, could gain further insight into the particle stabilization mechanism. In my study of the microstructure and rheology of concentrated simple Pickering emulsions, particle excluded volume interactions were shown to strongly mediate their microstructural and mechanical transitions. Future investigations on these systems, should examine the impact bridged particle monolayers, seen to form in HIPEs to stabilize thin films, on the mechanical behavior of concentrated emulsions. For my work on Pickering emulsion gels, the zero shear elastic modulus was seen to have a non-monotonic dependence on particle loading, which was rationalized based on a simple model of how the microstructure of Pickering emulsion gels formed. The yielding behavior of these solid-stabilized emulsions is still open for investigation. For all of the investigations I have conducted, better knowledge of the mechanics that governs the deformation of the particle-laden interfaces would be beneficial. I have begun studying individual particle-stabilized droplet under shear. Direct observation of these droplets is made possible by utilizing a counter-rotation stage as outlined in section 1.3.3. The preliminary results I have gathered illustrate the impact interfacial particles have on the deformation and rupture of droplets in shear flow. Below, the results are quickly reviewed.

In Figure 5.1, the deformation behavior of a bare droplet is compared with a particle-coated droplet placed under shear.

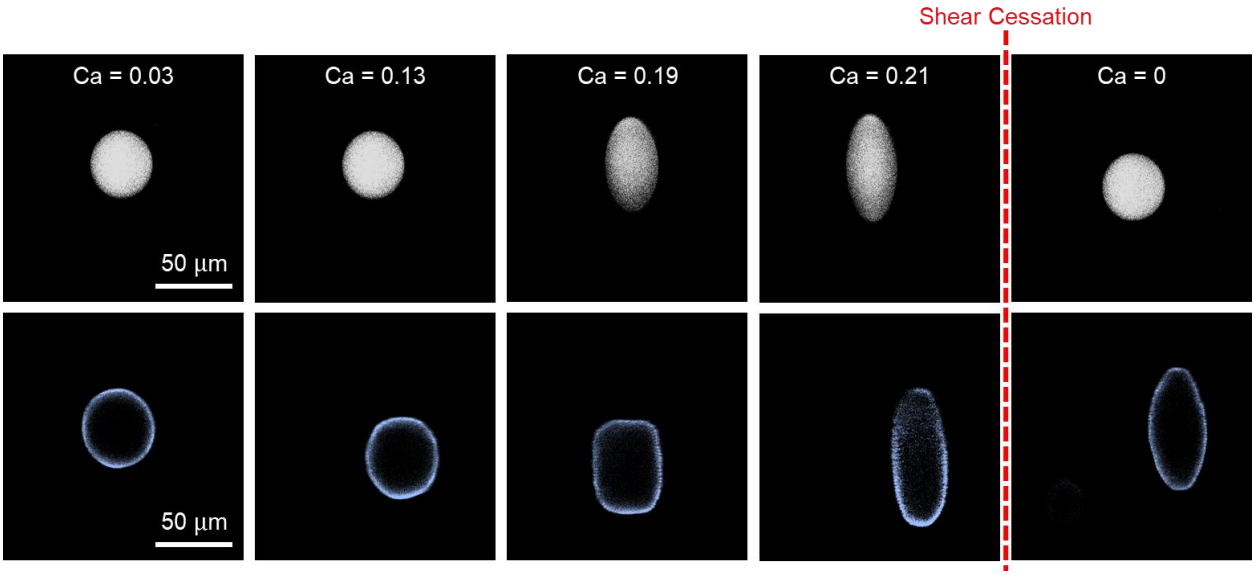

Figure 5.1. The deformation behavior of a bare droplet compared to a particle stabilized droplet undergoing similar shear conditions.

Each droplet is subjected to step-wise increases in shear rate before shear flow is abruptly halted. Increases in shear rate are denoted by the capillary number, $Ca = r\tau/\sigma$, where r, τ, and σ are droplet radius, τ shear stress and the fluid/fluid interfacial tension, respectively. From the images shown, we can qualitatively observe three differences in behavior, imparted by the presence of particles on the droplet interface. First, is the rectangular shape the particle armored droplet exhibits at Ca = 0.19. This deformation in droplet shape is not observed with a bare droplet, which shows a smooth transition from a sphere to an ellipsoid. Second, a greater degree of droplet deformation is observed for the particle-stabilized droplet at Ca = 0.21 than the bare droplet. Lastly, the cessation of shear flow generates a nonspherical particle-coated droplet that still exhibits some degree of its shear-induced deformation. The bare droplet is seen to immediately retract back to its original spherical shape. These behaviors imparted by the presence of particles at the droplet interface are being investigated. Another aspect that arises

due to the particles, that is not shown in Figure 5.1, is droplet instability to rupture. The particle-stabilized droplets readily rupture at a capillary number much lower than what is predicted for bare droplets. Examining a droplet after rupture, which lowers its particle surface coverage, shows the deformation behaviors noted from Figure 5.1 are sensitive to particle coverage. In Figure 5.2, the deformation behavior of a particle-stabilized droplet, after it has been ruptured once, is compared to a bare droplet under shear.

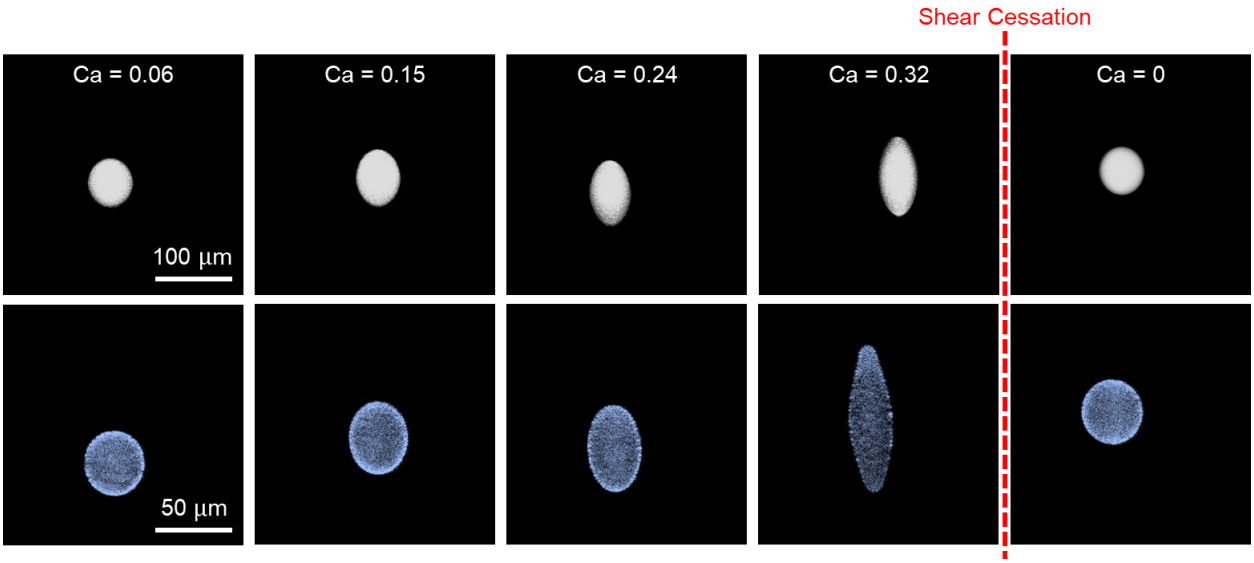

Figure 5.2. The deformation behavior of a bare droplet compared to a particle stabilized droplet, which was seen to rupture in a previous experiment, undergoing similar shear conditions.

Note, the rectangular shaped droplet and elongated droplet after shear cessation are no longer observed. Greater droplet deformation is still observed, but occurs at a higher capillary number, or greater shear rate. Future experiments look to further the investigation into these observations in order to rationalize their occurrence.

BIBLIOGRAPHY

[1] B. P. Binks and T. S. Horozov, *Colloidal particles at liquid interfaces*. Cambridge: Cambridge Univ. Press, 2006.

[2] J. C. Berg, *An Introduction to Interfaces and Colloids: The Bridge to Nanoscience*. WORLD SCIENTIFIC, 2009.

[3] R. J. Hunter, *Foundations of colloid science*, 2nd ed. Oxford ; New York: Oxford University Press, 2001.

[4] D. Rousseau, "Fat crystals and emulsion stability — a review," *Food Res. Int.*, vol. 33, no. 1, pp. 3–14, Jan. 2000.

[5] E. Dickinson, "Use of nanoparticles and microparticles in the formation and stabilization of food emulsions," *Trends Food Sci. Technol.*, vol. 24, no. 1, pp. 4–12, Mar. 2012.

[6] J. Falbe, *Surfactants in consumer products: theory, technology, and application*. Berlin; New York: Springer-Verlag, 2012.

[7] P. Mulqueen, "Recent advances in agrochemical formulation," *Adv. Colloid Interface Sci.*, vol. 106, no. 1, pp. 83–107, Dec. 2003.

[8] T. J. Thorson, R. E. Gurlin, E. L. Botvinick, and A. Mohraz, "Bijel-templated implantable biomaterials for enhancing tissue integration and vascularization," *Acta Biomater.*, vol. 94, pp. 173–182, Aug. 2019.

[9] J. A. Witt, D. R. Mumm, and A. Mohraz, "Microstructural tunability of co-continuous bijel-derived electrodes to provide high energy and power densities," *J. Mater. Chem. A*, vol. 4, no. 3, pp. 1000–1007, Jan. 2016.

[10] T. J. Thorson, E. L. Botvinick, and A. Mohraz, "Composite Bijel-Templated Hydrogels for Cell Delivery," *ACS Biomater. Sci. Eng.*, vol. 4, no. 2, pp. 587–594, Feb. 2018.

[11] N. R. Cameron and D. C. Sherrington, "High internal phase emulsions (HIPEs) — Structure, properties and use in polymer preparation," in *Biopolymers Liquid Crystalline Polymers Phase Emulsion*, Berlin, Heidelberg: Springer Berlin Heidelberg, 1996, pp. 163–214.

[12] N. R. Cameron, "High internal phase emulsion templating as a route to well-defined porous polymers," *Polymer*, vol. 46, no. 5, pp. 1439–1449, Feb. 2005.

[13] M. S. Silverstein, "PolyHIPEs: Recent advances in emulsion-templated porous polymers," *Prog. Polym. Sci.*, vol. 39, no. 1, pp. 199–234, Jan. 2014.

[14] S. Fujisawa, E. Togawa, and K. Kuroda, "Nanocellulose-stabilized Pickering emulsions and their applications," *Sci. Technol. Adv. Mater.*, vol. 18, no. 1, pp. 959–971, Dec. 2017.

[15] P. Finkle, H. D. Draper, and J. H. Hildebrand, "The Theory of Emulsification," *J. Am. Chem. Soc.*, vol. 45, no. 12, pp. 2780–2788, Dec. 1923.

[16] D. J. McClements, *Food emulsions: principles, practices, and techniques*, Third edition. Boca Raton: CRC Press, Taylor & Francis Group, 2016.

[17] B. P. Binks, "Particles as surfactants—similarities and differences," *Curr. Opin. Colloid Interface Sci.*, vol. 7, no. 1, pp. 21–41, Mar. 2002.

[18] W. Ramsden, "Separation of Solids in the Surface-Layers of Solutions and 'Suspensions' (Observations on Surface-Membranes, Bubbles, Emulsions, and Mechanical Coagulation). -- Preliminary Account," *Proc. R. Soc. Lond.*, vol. 72, no. 477–486, pp. 156–164, Jan. 1903.

[19] S. U. Pickering, "Emulsions," *J. Chem. Soc. Trans.*, vol. 91, no. 0, pp. 2001–2021, Jan. 1907.

[20] T. Young, “An Essay on the Cohesion of Fluids,” *Philos. Trans. R. Soc. Lond.*, vol. 95, no. 0, pp. 65–87, Jan. 1805.
[21] J. H. Schulman and J. Leja, “Control of contact angles at the oil-water-solid interfaces. Emulsions stabilized by solid particles (BaSO4),” *Trans. Faraday Soc.*, vol. 50, no. 0, pp. 598–605, Jan. 1954.
[22] D. E. Tambe and M. M. Sharma, “Factors Controlling the Stability of Colloid-Stabilized Emulsions: II. A Model for the Rheological Properties of Colloid-Laden Interfaces,” *J. Colloid Interface Sci.*, vol. 162, no. 1, pp. 1–10, Jan. 1994.
[23] G. Kaptay, “Interfacial criteria for stabilization of liquid foams by solid particles,” *Colloids Surf. Physicochem. Eng. Asp.*, vol. 230, no. 1, pp. 67–80, Dec. 2003.
[24] G. Kaptay, “On the equation of the maximum capillary pressure induced by solid particles to stabilize emulsions and foams and on the emulsion stability diagrams,” *Colloids Surf. Physicochem. Eng. Asp.*, vol. 282–283, pp. 387–401, Jul. 2006.
[25] A. V. Nushtaeva and P. M. Kruglyakov, “Capillary Pressure in Thinning Emulsion Film Stabilized with Solid Spherical Particles,” *Colloid J.*, vol. 65, no. 3, pp. 341–349, May 2003.
[26] T. S. Horozov, R. Aveyard, J. H. Clint, and B. Neumann, “Particle Zips: Vertical Emulsion Films with Particle Monolayers at Their Surfaces,” *Langmuir*, vol. 21, no. 6, pp. 2330–2341, Mar. 2005.
[27] T. S. Horozov and B. P. Binks, “Particle-Stabilized Emulsions: A Bilayer or a Bridging Monolayer?,” *Angew. Chem. Int. Ed.*, vol. 45, no. 5, pp. 773–776, Jan. 2006.
[28] T. G. Mason, “New fundamental concepts in emulsion rheology,” *Curr. Opin. Colloid Interface Sci.*, vol. 4, no. 3, pp. 231–238, Jun. 1999.
[29] S. R. Derkach, “Rheology of emulsions,” *Adv. Colloid Interface Sci.*, vol. 151, no. 1, pp. 1–23, Oct. 2009.
[30] S. Arditty, V. Schmitt, J. Giermanska-Kahn, and F. Leal-Calderon, “Materials based on solid-stabilized emulsions,” *J. Colloid Interface Sci.*, vol. 275, no. 2, pp. 659–664, Jul. 2004.
[31] S. S. Datta, D. D. Gerrard, T. S. Rhodes, T. G. Mason, and D. A. Weitz, “Rheology of attractive emulsions,” *Phys. Rev. E*, vol. 84, no. 4, Oct. 2011.
[32] R. Pal, “Rheology of simple and multiple emulsions,” *Curr. Opin. Colloid Interface Sci.*, vol. 16, no. 1, pp. 41–60, Feb. 2011.
[33] T. F. Tadros, “Fundamental principles of emulsion rheology and their applications,” *Colloids Surf. Physicochem. Eng. Asp.*, vol. 91, pp. 39–55, Nov. 1994.
[34] E. M. Herzig, K. A. White, A. B. Schofield, W. C. K. Poon, and P. S. Clegg, “Bicontinuous emulsions stabilized solely by colloidal particles,” *Nat. Mater.*, vol. 6, no. 12, pp. 966–971, Dec. 2007.
[35] M. N. Lee, H. K. Chan, and A. Mohraz, “Characteristics of Pickering Emulsion Gels Formed by Droplet Bridging,” *Langmuir*, vol. 28, no. 6, pp. 3085–3091, Feb. 2012.
[36] J. T. Muth and J. A. Lewis, “Microstructure and Elastic Properties of Colloidal Gel Foams,” *Langmuir*, vol. 33, no. 27, pp. 6869–6877, Jul. 2017.
[37] M. Kaganyuk and A. Mohraz, “Role of particles in the rheology of solid-stabilized high internal phase emulsions,” *J. Colloid Interface Sci.*, vol. 540, pp. 197–206, Mar. 2019.
[38] H. Katepalli, V. T. John, A. Tripathi, and A. Bose, “Microstructure and rheology of particle stabilized emulsions: Effects of particle shape and inter-particle interactions,” *J. Colloid Interface Sci.*, vol. 485, pp. 11–17, Jan. 2017.

[39] T. G. Mason, J. Bibette, and D. A. Weitz, “Elasticity of Compressed Emulsions,” *Phys. Rev. Lett.*, vol. 75, no. 10, pp. 2051–2054, Sep. 1995.
[40] H. M. Princen and A. D. Kiss, “Rheology of foams and highly concentrated emulsions,” *J. Colloid Interface Sci.*, vol. 112, no. 2, pp. 427–437, Aug. 1986.
[41] H. M. Princen, “Rheology of foams and highly concentrated emulsions,” *J. Colloid Interface Sci.*, vol. 91, no. 1, pp. 160–175, Jan. 1983.
[42] S. Cohen-Addad and R. Höhler, “Rheology of foams and highly concentrated emulsions,” *Curr. Opin. Colloid Interface Sci.*, vol. 19, no. 6, pp. 536–548, Dec. 2014.
[43] E. R. Weeks, J. C. Crocker, A. C. Levitt, A. Schofield, and D. A. Weitz, “Three-Dimensional Direct Imaging of Structural Relaxation Near the Colloidal Glass Transition,” *Science*, vol. 287, no. 5453, pp. 627–631, Jan. 2000.
[44] C. J. Dibble, M. Kogan, and M. J. Solomon, “Structure and dynamics of colloidal depletion gels: coincidence of transitions and heterogeneity,” *Phys. Rev. E*, vol. 74, no. 4, Oct. 2006.
[45] A. D. Dinsmore, V. Prasad, I. Y. Wong, and D. A. Weitz, “Microscopic structure and elasticity of weakly aggregated colloidal gels,” *Phys. Rev. Lett.*, vol. 96, no. 18, p. 185502, May 2006.
[46] M. Marvin, “Microscopy apparatus,” US3013467A, 19-Dec-1961.
[47] K. J. Lissant, B. W. Peace, S. H. Wu, and K. G. Mayhan, “Structure of high-internal-phase-ratio emulsions,” *J. Colloid Interface Sci.*, vol. 47, no. 2, pp. 416–423, May 1974.
[48] R. Foudazi, S. Qavi, I. Masalova, and A. Y. Malkin, “Physical chemistry of highly concentrated emulsions,” *Adv. Colloid Interface Sci.*, vol. 220, pp. 78–91, Jun. 2015.
[49] J. Naranda *et al.*, “Polyester type polyHIPE scaffolds with an interconnected porous structure for cartilage regeneration,” *Sci. Rep.*, vol. 6, p. 28695, Jun. 2016.
[50] R. Moglia, M. Whitely, M. Brooks, J. Robinson, M. Pishko, and E. Cosgriff-Hernandez, “Solvent-Free Fabrication of polyHIPE Microspheres for Controlled Release of Growth Factors,” *Macromol. Rapid Commun.*, vol. 35, no. 14, pp. 1301–1305, 2014.
[51] N. C. Grant, A. I. Cooper, and H. Zhang, “Uploading and Temperature-Controlled Release of Polymeric Colloids via Hydrophilic Emulsion-Templated Porous Polymers,” *ACS Appl. Mater. Interfaces*, vol. 2, no. 5, pp. 1400–1406, May 2010.
[52] P. J. Colver and S. A. F. Bon, “Cellular Polymer Monoliths Made via Pickering High Internal Phase Emulsions,” *Chem. Mater.*, vol. 19, no. 7, pp. 1537–1539, Apr. 2007.
[53] I. Capron and B. Cathala, “Surfactant-Free High Internal Phase Emulsions Stabilized by Cellulose Nanocrystals,” *Biomacromolecules*, vol. 14, no. 2, pp. 291–296, Feb. 2013.
[54] T. Zeng *et al.*, “Development of antioxidant Pickering high internal phase emulsions (HIPEs) stabilized by protein/polysaccharide hybrid particles as potential alternative for PHOs,” *Food Chem.*, vol. 231, pp. 122–130, Sep. 2017.
[55] S. Zhang and J. Chen, “PMMA based foams made via surfactant -free high internal phase emulsion templates,” *Chem. Commun.*, vol. 0, no. 16, pp. 2217–2219, 2009.
[56] T. G. Mason, M.-D. Lacasse, G. S. Grest, D. Levine, J. Bibette, and D. A. Weitz, “Osmotic pressure and viscoelastic shear moduli of concentrated emulsions,” *Phys. Rev. E*, vol. 56, no. 3, pp. 3150–3166, Sep. 1997.
[57] T. S. Horozov, “Foams and foam films stabilised by solid particles,” *Curr. Opin. Colloid Interface Sci.*, vol. 13, no. 3, pp. 134–140, Jun. 2008.

[58] V. O. Ikem, A. Menner, and A. Bismarck, “High Internal Phase Emulsions Stabilized Solely by Functionalized Silica Particles,” *Angew. Chem. Int. Ed.*, vol. 47, no. 43, pp. 8277–8279, 2008.
[59] C. P. Whitby, L. Lotte, and C. Lang, “Structure of concentrated oil-in-water Pickering emulsions,” *Soft Matter*, vol. 8, no. 30, pp. 7784–7789, Jul. 2012.
[60] H. M. Princen, “Osmotic pressure of foams and highly concentrated emulsions. I. Theoretical considerations,” *Langmuir*, vol. 2, no. 4, pp. 519–524, Jul. 1986.
[61] T. R. Briggs, “Emulsions with Finely Divided Solids,” *J. Ind. Eng. Chem.*, vol. 13, no. 11, pp. 1008–1010, Nov. 1921.
[62] Y. Yang *et al.*, “An Overview of Pickering Emulsions: Solid-Particle Materials, Classification, Morphology, and Applications,” *Front. Pharmacol.*, vol. 8, May 2017.
[63] N. Denkov, I. . Ivanov, P. . Kralchevsky, and D. . Wasan, “A possible mechanism of stabilization of emulsions by solid particles,” *J. Colloid Interface Sci.*, vol. 150, no. 2, pp. 589–593, May 1992.
[64] M. Kaganyuk and A. Mohraz, “Non-monotonic dependence of Pickering emulsion gel rheology on particle volume fraction,” *Soft Matter*, vol. 13, no. 13, pp. 2513–2522, 2017.
[65] H. Xu, M. Lask, J. Kirkwood, and G. Fuller, “Particle Bridging between Oil and Water Interfaces,” *Langmuir*, vol. 23, no. 9, pp. 4837–4841, Apr. 2007.
[66] D. J. French, P. Taylor, J. Fowler, and P. S. Clegg, “Making and breaking bridges in a Pickering emulsion,” *J. Colloid Interface Sci.*, vol. 441, pp. 30–38, Mar. 2015.
[67] V. N. Paunov, P. A. Kralchevsky, N. D. Denkov, and K. Nagayama, “Lateral Capillary Forces between Floating Submillimeter Particles,” *J. Colloid Interface Sci.*, vol. 157, no. 1, pp. 100–112, Apr. 1993.
[68] F. Qi, J. Wu, G. Sun, F. Nan, T. Ngai, and G. Ma, “Systematic studies of Pickering emulsions stabilized by uniform-sized PLGA particles: preparation and stabilization mechanism,” *J. Mater. Chem. B*, vol. 2, no. 43, pp. 7605–7611, Oct. 2014.
[69] M. M. van Schooneveld, V. W. A. de Villeneuve, R. P. A. Dullens, D. G. A. L. Aarts, M. E. Leunissen, and W. K. Kegel, “Structure, Stability, and Formation Pathways of Colloidal Gels in Systems with Short-Range Attraction and Long-Range Repulsion,” *J. Phys. Chem. B*, vol. 113, no. 14, pp. 4560–4564, Apr. 2009.
[70] M. T. Elsesser and A. D. Hollingsworth, “Revisiting the Synthesis of a Well-Known Comb-Graft Copolymer Stabilizer and Its Application to the Dispersion Polymerization of Poly(methyl methacrylate) in Organic Media,” *Langmuir*, vol. 26, no. 23, pp. 17989–17996, Dec. 2010.
[71] M. E. Leunissen, A. van Blaaderen, A. D. Hollingsworth, M. T. Sullivan, and P. M. Chaikin, “Electrostatics at the oil-water interface, stability, and order in emulsions and colloids,” *Proc. Natl. Acad. Sci.*, vol. 104, no. 8, pp. 2585–2590, Feb. 2007.
[72] S. Arditty, C. P. Whitby, B. P. Binks, V. Schmitt, and F. Leal-Calderon, “Some general features of limited coalescence in solid-stabilized emulsions,” *Eur. Phys. J. E*, vol. 11, no. 3, pp. 273–281.
[73] M. Visschers, J. Laven, and R. van der Linde, “Forces operative during film formation from latex dispersions,” *Prog. Org. Coat.*, vol. 31, no. 4, pp. 311–323, Aug. 1997.
[74] A. B. Pawar, M. Caggioni, R. Ergun, R. W. Hartel, and P. T. Spicer, “Arrested coalescence in Pickering emulsions,” *Soft Matter*, vol. 7, no. 17, pp. 7710–7716, Aug. 2011.

[75] S. Abedi, N. S. Suteria, C.-C. Chen, and S. A. Vanapalli, “Microfluidic production of size-tunable hexadecane-in-water emulsions: Effect of droplet size on destabilization of two-dimensional emulsions due to partial coalescence,” *J. Colloid Interface Sci.*, vol. 533, pp. 59–70, Jan. 2019.
[76] A. R. Studart, H. C. Shum, and D. A. Weitz, “Arrested Coalescence of Particle-coated Droplets into Nonspherical Supracolloidal Structures,” *J. Phys. Chem. B*, vol. 113, no. 12, pp. 3914–3919, Mar. 2009.
[77] A. B. Subramaniam, M. Abkarian, L. Mahadevan, and H. A. Stone, “Non-spherical bubbles,” *Nature*, vol. 438, no. 7070, pp. 930–930, Dec. 2005.
[78] P. Dahiya *et al.*, “Arrested coalescence of viscoelastic droplets: triplet shape and restructuring,” *Soft Matter*, vol. 13, no. 14, pp. 2686–2697, Apr. 2017.
[79] D. Vella, P. Aussillous, and L. Mahadevan, “Elasticity of an interfacial particle raft,” *EPL Europhys. Lett.*, vol. 68, no. 2, p. 212, Oct. 2004.
[80] L. Maurice, R. A. Maguire, A. B. Schofield, M. E. Cates, P. S. Clegg, and J. H. J. Thijssen, “Squeezing particle-stabilized emulsions into biliquid foams – equation of state,” *Soft Matter*, vol. 9, no. 32, p. 7757, 2013.
[81] T. F. Tadros, “Emulsion Formation, Stability, and Rheology,” in *Emulsion Formation and Stability*, T. F. Tadros, Ed. Wiley-VCH Verlag GmbH & Co. KGaA, 2013, pp. 1–75.
[82] E. Rio, W. Drenckhan, A. Salonen, and D. Langevin, “Unusually stable liquid foams,” *Adv. Colloid Interface Sci.*, vol. 205, pp. 74–86, Mar. 2014.
[83] T. N. Hunter, R. J. Pugh, G. V. Franks, and G. J. Jameson, “The role of particles in stabilising foams and emulsions,” *Adv. Colloid Interface Sci.*, vol. 137, no. 2, pp. 57–81, Mar. 2008.
[84] I. Kralova and J. Sjöblom, “Surfactants Used in Food Industry: A Review,” *J. Dispers. Sci. Technol.*, vol. 30, no. 9, pp. 1363–1383, Sep. 2009.
[85] J. Wadhwa, A. Nair, and R. Kumria, “Emulsion forming drug delivery system for lipophilic drugs,” *Acta Pol. Pharm.*, vol. 69, no. 2, pp. 179–191, Apr. 2012.
[86] T. Sharma, G. S. Kumar, and J. S. Sangwai, “Enhanced oil recovery using oil-in-water (o/w) emulsion stabilized by nanoparticle, surfactant and polymer in the presence of NaCl,” *Geosystem Eng.*, vol. 17, no. 3, pp. 195–205, May 2014.
[87] S. Caldwell *et al.*, “Degradable emulsion-templated scaffolds for tissue engineering from thiol–ene photopolymerisation,” *Soft Matter*, vol. 8, no. 40, pp. 10344–10351, 2012.
[88] J. G. Pribyl, K. M. L. Taylor-Pashow, T. C. Shehee, and B. C. Benicewicz, “High-Capacity Poly(4-vinylpyridine) Grafted PolyHIPE Foams for Efficient Plutonium Separation and Purification,” *ACS Omega*, vol. 3, no. 7, pp. 8181–8189, Jul. 2018.
[89] J. Yin, T. Zhang, E. Schulman, D. Liu, and J. Meng, “Hierarchical porous metallized poly-melamine-formaldehyde (PMF) as a low-cost and high-efficiency catalyst for cyclic carbonate synthesis from CO2 and epoxides,” *J. Mater. Chem. A*, vol. 6, no. 18, pp. 8441–8448, May 2018.
[90] C. Zhao, E. Danish, N. R. Cameron, and R. Kataky, “Emulsion-templated porous materials (PolyHIPEs) for selective ion and molecular recognition and transport: applications in electrochemical sensing,” *J. Mater. Chem.*, vol. 17, no. 23, pp. 2446–2453, 2007.
[91] H. S. Kim and T. G. Mason, “Advances and challenges in the rheology of concentrated emulsions and nanoemulsions,” *Adv. Colloid Interface Sci.*, vol. 247, pp. 397–412, Sep. 2017.

[92] R. Pal, “Influence of interfacial rheology on the viscosity of concentrated emulsions,” *J. Colloid Interface Sci.*, vol. 356, pp. 118–22, Apr. 2011.
[93] I. Masalova, R. Foudazi, and A. Y. Malkin, “The rheology of highly concentrated emulsions stabilized with different surfactants,” *Colloids Surf. Physicochem. Eng. Asp.*, vol. 375, no. 1, pp. 76–86, Feb. 2011.
[94] R. Foudazi, I. Masalova, and A. Y. Malkin, “The role of interdroplet interaction in the physics of highly concentrated emulsions,” *Colloid J.*, vol. 72, no. 1, pp. 74–92, Feb. 2010.
[95] A. Menner, R. Powell, and A. Bismarck, “Open Porous Polymer Foams via Inverse Emulsion Polymerization: Should the Definition of High Internal Phase (Ratio) Emulsions Be Extended?,” *Macromolecules*, vol. 39, no. 6, pp. 2034–2035, Mar. 2006.
[96] L. Bressy, P. Hébraud, V. Schmitt, and J. Bibette, “Rheology of Emulsions Stabilized by Solid Interfaces,” *Langmuir*, vol. 19, no. 3, pp. 598–604, Feb. 2003.
[97] J. Bergenholtz, M. Fuchs, and T. Voigtmann, “Colloidal gelation and non-ergodicity transitions,” *J. Phys. Condens. Matter*, vol. 12, no. 29, p. 6575, 2000.
[98] W. C. K. Poon, A. D. Pirie, and P. N. Pusey, “Gelation in colloid–polymer mixtures,” *Faraday Discuss.*, vol. 101, no. 0, pp. 65–76, Jan. 1995.
[99] M. N. Lee, J. H. J. Thijssen, J. A. Witt, P. S. Clegg, and A. Mohraz, “Making a Robust Interfacial Scaffold: Bijel Rheology and its Link to Processability,” *Adv. Funct. Mater.*, vol. 23, no. 4, pp. 417–423, Jan. 2013.
[100] W. Stöber, A. Fink, and E. Bohn, “Controlled growth of monodisperse silica spheres in the micron size range,” *J. Colloid Interface Sci.*, vol. 26, no. 1, pp. 62–69, Jan. 1968.
[101] A. Van Blaaderen and A. Vrij, “Synthesis and characterization of colloidal dispersions of fluorescent, monodisperse silica spheres,” *Langmuir*, vol. 8, no. 12, pp. 2921–2931, Dec. 1992.
[102] M.-D. Lacasse, G. S. Grest, D. Levine, T. G. Mason, and D. A. Weitz, “Model for the Elasticity of Compressed Emulsions,” *Phys. Rev. Lett.*, vol. 76, no. 18, pp. 3448–3451, Apr. 1996.
[103] L. G. Torres, R. Iturbe, M. J. Snowden, B. Z. Chowdhry, and S. A. Leharne, “Preparation of o/w emulsions stabilized by solid particles and their characterization by oscillatory rheology,” *Colloids Surf. Physicochem. Eng. Asp.*, vol. 302, no. 1, pp. 439–448, Jul. 2007.
[104] S. Simon, S. Theiler, A. Knudsen, G. Øye, and J. Sjöblom, “Rheological Properties of Particle-Stabilized Emulsions,” *J. Dispers. Sci. Technol.*, vol. 31, no. 5, pp. 632–640, Apr. 2010.
[105] M. Derakhshandeh, B. K. Pilapil, B. Workman, M. Trifkovic, and S. L. Bryant, “Analysis of network formation and long-term stability in silica nanoparticle stabilized emulsions,” *Soft Matter*, vol. 14, no. 21, pp. 4268–4277, May 2018.
[106] M. M. Kohonen, D. Geromichalos, M. Scheel, C. Schier, and S. Herminghaus, “On capillary bridges in wet granular materials,” *Phys. Stat. Mech. Its Appl.*, vol. 339, no. 1, pp. 7–15, Aug. 2004.
[107] M. Badetti *et al.*, “Rheology and microstructure of unsaturated wet granular materials: Experiments and simulations,” *J. Rheol.*, vol. 62, no. 5, pp. 1175–1186, Aug. 2018.
[108] F. Bossler and E. Koos, “Structure of Particle Networks in Capillary Suspensions with Wetting and Nonwetting Fluids,” *Langmuir*, vol. 32, no. 6, pp. 1489–1501, Feb. 2016.
[109] E. Koos, “Capillary suspensions: Particle networks formed through the capillary force,” *Curr. Opin. Colloid Interface Sci.*, vol. 19, no. 6, pp. 575–584, Dec. 2014.

[110] T. Domenech and S. S. Velankar, “On the rheology of pendular gels and morphological developments in paste-like ternary systems based on capillary attraction,” *Soft Matter*, vol. 11, no. 8, pp. 1500–1516, 2015.
[111] E. Koos and N. Willenbacher, “Capillary Forces in Suspension Rheology,” *Science*, vol. 331, no. 6019, pp. 897–900, Feb. 2011.
[112] S. S. Velankar, “A non-equilibrium state diagram for liquid/fluid/particle mixtures,” *Soft Matter*, vol. 11, no. 43, pp. 8393–8403, 2015.
[113] B. P. Binks, J. H. Clint, and C. P. Whitby, “Rheological Behavior of Water-in-Oil Emulsions Stabilized by Hydrophobic Bentonite Particles,” *Langmuir*, vol. 21, no. 12, pp. 5307–5316, Jun. 2005.
[114] M. Rayner, D. Marku, M. Eriksson, M. Sjöö, P. Dejmek, and M. Wahlgren, “Biomass-based particles for the formulation of Pickering type emulsions in food and topical applications,” *Colloids Surf. Physicochem. Eng. Asp.*, vol. 458, pp. 48–62, Sep. 2014.
[115] J. Marto *et al.*, “Starch-based Pickering emulsions for topical drug delivery: A QbD approach,” *Colloids Surf. B-Biointerfaces*, vol. 135, pp. 183–192, Nov. 2015.
[116] O. D. Velev, K. Furusawa, and K. Nagayama, “Assembly of Latex Particles by Using Emulsion Droplets as Templates. 1. Microstructured Hollow Spheres,” *Langmuir*, vol. 12, no. 10, pp. 2374–2384, Jan. 1996.
[117] M. N. Lee and A. Mohraz, “Bicontinuous Macroporous Materials from Bijel Templates,” *Adv. Mater.*, vol. 22, no. 43, pp. 4836–4841, Nov. 2010.
[118] A. P. Sullivan and P. K. Kilpatrick, “The Effects of Inorganic Solid Particles on Water and Crude Oil Emulsion Stability,” *Ind. Eng. Chem. Res.*, vol. 41, no. 14, pp. 3389–3404, Jul. 2002.
[119] N. Zhang, L. Zhang, and D. Sun, “Influence of emulsification process on the properties of Pickering emulsions stabilized by layered double hydroxide particles,” *Langmuir ACS J. Surf. Colloids*, vol. 31, no. 16, pp. 4619–4626, Apr. 2015.
[120] J. W. Tavacoli, J. H. J. Thijssen, A. B. Schofield, and P. S. Clegg, “Novel, Robust, and Versatile Bijels of Nitromethane, Ethanediol, and Colloidal Silica: Capsules, Sub-Ten-Micrometer Domains, and Mechanical Properties,” *Adv. Funct. Mater.*, vol. 21, no. 11, pp. 2020–2027, Jun. 2011.
[121] L. Bai, J. W. Fruehwirth, X. Cheng, and C. W. Macosko, “Dynamics and rheology of nonpolar bijels,” *Soft Matter*, vol. 11, no. 26, pp. 5282–5293, Jul. 2015.
[122] L. Imperiali, C. Clasen, J. Fransaer, C. W. Macosko, and J. Vermant, “A simple route towards graphene oxide frameworks,” *Mater Horiz*, vol. 1, no. 1, pp. 139–145, 2014.
[123] E. J. Stancik, M. Kouhkan, and G. G. Fuller, “Coalescence of particle-laden fluid interfaces,” *Langmuir ACS J. Surf. Colloids*, vol. 20, no. 1, pp. 90–94, Jan. 2004.
[124] E. J. Stancik and G. G. Fuller, “Connect the drops: using solids as adhesives for liquids,” *Langmuir ACS J. Surf. Colloids*, vol. 20, no. 12, pp. 4805–4808, Jun. 2004.
[125] N. P. Ashby, B. P. Binks, and V. N. Paunov, “Bridging interaction between a water drop stabilised by solid particles and a planar oil/water interface,” *Chem. Commun.*, no. 4, p. 436, 2004.
[126] P. Thareja and S. Velankar, “Particle-induced bridging in immiscible polymer blends,” *Rheol. Acta*, vol. 46, no. 3, pp. 405–412, Dec. 2006.
[127] P. Thareja and S. Velankar, “Rheology of immiscible blends with particle-induced drop clusters,” *Rheol. Acta*, vol. 47, no. 2, pp. 189–200, Mar. 2008.

[128] F. Thivilliers, N. Drelon, V. Schmitt, and F. Leal-Calderon, “Bicontinuous emulsion gels induced by partial coalescence: Kinetics and mechanism,” *Europhys. Lett. EPL*, vol. 76, no. 2, pp. 332–338, Oct. 2006.
[129] J. Vermant, S. Vandebril, C. Dewitte, and P. Moldenaers, “Particle-stabilized polymer blends,” *Rheol. Acta*, vol. 47, no. 7, pp. 835–839, Sep. 2008.
[130] J. A. Witt, D. R. Mumm, and A. Mohraz, “Bijel reinforcement by droplet bridging: a route to bicontinuous materials with large domains,” *Soft Matter*, vol. 9, no. 29, p. 6773, 2013.
[131] D. S. Frost, J. J. Schoepf, E. M. Nofen, and L. L. Dai, “Understanding droplet bridging in ionic liquid-based Pickering emulsions,” *J. Colloid Interface Sci.*, vol. 383, no. 1, pp. 103–109, Oct. 2012.
[132] P. Varadan and M. J. Solomon, “Direct Visualization of Long-Range Heterogeneous Structure in Dense Colloidal Gels,” *Langmuir*, vol. 19, no. 3, pp. 509–512, Feb. 2003.
[133] R. Buscall, P. D. A. Mills, J. W. Goodwin, and D. W. Lawson, “Scaling behaviour of the rheology of aggregate networks formed from colloidal particles,” *J. Chem. Soc. Faraday Trans. 1 Phys. Chem. Condens. Phases*, vol. 84, no. 12, pp. 4249–4260, Jan. 1988.
[134] W.-H. Shih, W. Y. Shih, S.-I. Kim, J. Liu, and I. A. Aksay, “Scaling behavior of the elastic properties of colloidal gels,” *Phys. Rev. A*, vol. 42, no. 8, pp. 4772–4779, Oct. 1990.
[135] M. Chen and W. Russel, “Characteristics of flocculated silica dispersions,” *J. Colloid Interface Sci.*, vol. 141, no. 2, pp. 564–577, Feb. 1991.
[136] C. J. Rueb and C. F. Zukoski, “Viscoelastic properties of colloidal gels,” *J. Rheol.*, vol. 41, no. 2, p. 197, Mar. 1997.